



Cite this: *J. Mater. Chem. C*,
2024, 12, 10330

Advancements in semiconductor quantum dots: expanding frontiers in optoelectronics, analytical sensing, biomedicine, and catalysis

Jiban Mondal,^a Rohan Lamba,^b Yukta Yukta,^c Rohit Yadav,^d Ram Kumar,^{ce} Balaram Pani^{ID *e} and Bholey Singh^{ID *f}

Semiconductor colloidal quantum dots (CQDs) have emerged as pivotal entities at the forefront of modern nanotechnology, promising revolutionary advancements across various fields including optoelectronics, quantum computing, photocatalysis, and biomedical imaging. In this comprehensive review, we present the latest developments in CQD research offering a profound exploration of their innovative concepts and analyzing recent methodologies and strategies across diverse domains. We first explore the superiority of CQDs over other nanomaterials in the biomedical, optoelectronics, analytical sensing, and photocatalysis domains along with the discovery of CQDs with modern developments. We begin with photophysical properties of CQDs that include size-tunable bandgaps, narrow linewidth emissions, tunable surface chemistry and charge transport, excitation-dependent photoluminescence quantum yields, fluorescence blinking, and "dark fractions". We even address the origin of blinking along with models that govern the fluorescence intermittency within the nanocrystal followed by how the photoluminescence quantum yield (PLQY) of CQDs is hampered by excitation energy and "dark fractions". Then, we delve into the development of exemplary devices featuring a spectrum of architectures, elucidating the recent progress that has led to significant improvements in optoelectronic device efficiency. Furthermore, we examine procedures for converting CQDs into adaptable biological probes for subcellular imaging, drug delivery vehicles, biosensors, and therapeutic agents in the biomedical domain. Additionally, we thoroughly investigate the critical role of ligand selection and synthesis protocols in photocatalysis and analytical sensing, elucidating the underlying photophysical principles in each application. We also discuss ongoing debates, future directions, and emerging trends in the field, aiming to spark increased interest in CQDs and CQD-based composites by showcasing their myriad advantages across various applications. This review serves to underscore the transformative potential of CQDs and stimulate further exploration and innovation in harnessing their unique capabilities.

Received 5th April 2024,

Accepted 12th June 2024

DOI: 10.1039/d4tc01396d

rsc.li/materials-c

1. Introduction

Colloidal quantum dots (CQDs) are semiconductor nanostructures with spherical shapes and are nanoscale in size. The wave

^a Centre for Nano Science and Engineering, Indian Institute of Science, Bangalore 560012, India

^b Department of Biomedical Engineering, Technion-Israel Institute of Technology, Haifa, Israel

^c Department of Chemistry, University of Delhi, Delhi 110007, India

^d Institute of Biophysics, Johannes Kepler University Linz, Gruberstraße 40, 4020, Linz, Austria

^e Department of Chemistry, Bhaskaracharya College of Applied Sciences, University of Delhi, New Delhi 110075, India

^f Department of Chemistry, Swami Shraddhanand College, University of Delhi, Delhi 110036, India. E-mail: bholeysingh@ss.du.ac.in

function of the electrons and holes in these particles is determined by the quantum confinement regime. Quantum confinement occurs when electrons are confined to an area similar to their de Broglie wavelength. In simple words, the fact that CQDs' particle sizes are smaller than the Bohr radius causes their energy levels to become quantized (Fig. 1). This leads to unique properties such as narrow linewidth and a tunable band gap energy, enabling size-tunable absorption and significantly boosting photoluminescence efficiency with a peak maximum that is related to the nanocrystal size and differs from that of the bulk material.^{1–5} The effective bandgap of CQDs expands with their size due to quantum confinement, which causes the absorption and emission spectra to shift to blue. Coulomb attraction and spin-exchange coupling cause tightly confined electron-hole pairs, or excitons when an electron is excited

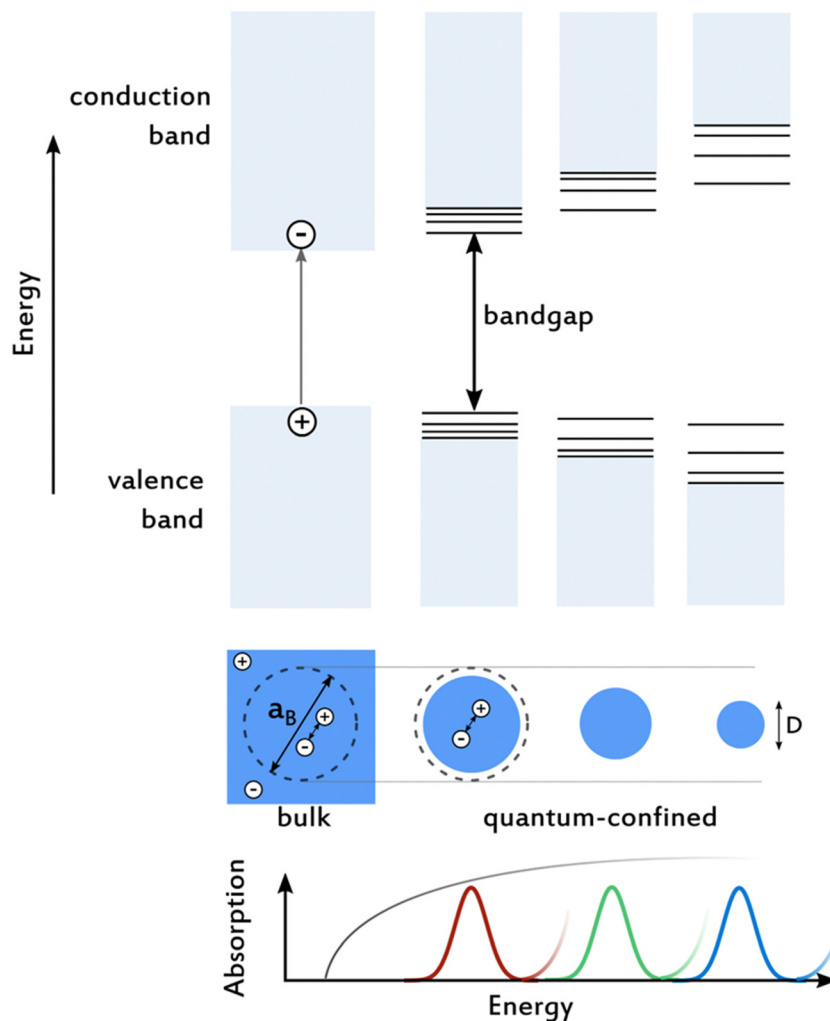


Fig. 1 Schematic depiction of quantum confinement of CQD materials. When the Bohr exciton diameter (a_B) is less than the spatial extent of electronic wave functions, quantum confinement takes place, resulting in size-dependent optical and electrical characteristics that differ from those of parental bulk materials. D is the diameter of the CQD. Reproduced with permission from ref. 7. Copyright 2021 Science.

across the bandgap. Multiple excitons are capable of populating a CQD at high excitation levels. Because of their close proximity, charge carriers in CQDs experience heightened many-body phenomena that influence their optoelectronic and electrical characteristics.^{6,7} Because of these special characteristics, colloidal CQDs are some of the most exciting and adaptable luminophores available today. At the forefront of functional materials and nanotechnology, they are having a significant impact on many aspects of contemporary biology, with colloidal CQDs being used extensively as labels and contrast agents in *in vitro* and *in vivo* biosensing applications.⁸ Nevertheless, the surface modification of CQDs makes them a potential tool in cancer imaging. Bioimaging and cancer detection can benefit from the attachment of specific biomolecules (such as peptides, antibodies, or small molecules) to CQDs.⁹ For instance, Brunetti *et al.* produced near-infrared (NIR) CQDs that were selectively accumulated at the location of colon cancer by their specific absorption and functionalization with NT4 cancer-selective tetra-branched peptides.¹⁰ In other

reports, CQDs have been used to help uncover drug release *in vivo*,¹¹ drug-targeted photothermal treatment,¹² and photodynamic therapy.¹³ The environment-dependent optical properties of CQDs enable their applications as biosensors to sense parameters like pH, temperature, and ROS inside the cells.¹⁴ Besides, biomedical applications, numerous display manufacturers have started adopting CQDs as light conversion, light absorbing, and solar energy conversion materials for CQD-photoluminescence techniques, photodetectors, and photovoltaic systems, respectively.^{15–17} They have also tried to use CQD films as an active material for field effect transistors¹⁸ and solar cells,¹⁹ and as a self-emitting layer for the CQD-electroluminescence (EL) device structure.²⁰ With their massive Stokes shift, strong photoluminescence quantum yield (PLQY), and high extinction coefficient across a broad-spectrum range, CQDs are becoming a more popular choice in science for use in a wide range of optoelectronic device designs.²¹ Recent advances in CQD nanotechnology have also slowly introduced these nanomaterials into analytical areas mostly as chemical

sensors in fluorescence-based measurements.^{22–24} Since CQDs are extremely small and have a high surface-to-volume ratio, their surface becomes crucial because any changes to the surrounding medium or interactions with specific chemical species are modifiable at different levels and significantly alter the photoluminescence properties, particularly the intensity of the emission. In the majority of cases, it may primarily impact the CQD's PLQY which is the ratio of photons released to photons absorbed by affecting electron–hole recombination efficiency, however, it may also encourage a spectrum shift or alter the PL decay time. From an analytical point of view, there are several ways to perceive the modulation of CQD luminescence as a selective response to a particular analyte recognition: direct or indirect chemiluminescence enhancing or quenching, chemiluminescence resonance energy transfer (CRET), annihilation or co-reactant electroluminescence, and fluorescence intensity quenching or enhancing.²⁵ Consequently, CQDs have been widely reported as an analytical instrument to detect many substances, including heavy metal ions, harmful pesticides, viruses, amino acids, medicines, gases, and so on.²⁶ Additionally, because of their low cost, chemical adjustability, and unique light-capturing capability, CQDs have attracted a lot of interest in photocatalytic applications. The use of CQDs and CQD-based composites in photocatalysis is the subject of research projects conducted by several organizations throughout the globe. There have been several published research studies on the use of CQDs as catalysts for a wide range of activities, including the production of stereospecific chemical compounds, water splitting, CO₂ reduction, dye degradation, and many more.^{27–29}

In acknowledgment of the superiority of CQDs in a variety of applications, Prof. Moungi G. Bawendi, Prof. Luis E. Brus, and Prof. Alexi I. Ekimov were awarded the 2023 Nobel Prize in Chemistry for their pioneering contributions to the discovery and synthesis of CQDs. The experimental realization of CQDs began with Ekimov *et al.*'s observation of size quantization effects in CuCl embedded in glass in 1981.³⁰ Shortly after chemically synthesized colloidal nanocrystals were developed, Brus *et al.* prepared colloidal CdS suspensions in 1982,³¹ which was followed by the demonstration of size quantization effects in 1983.³² The demonstration of particle size effects in small semiconductor nanoparticles was also supported by a number of other research groups, including Effros (1982),³³ Albery (1984),³⁴ Henglein (1985),³⁵ Gerischer (1986),³⁶ Sandroff (1986),³⁷ and Alivisatos (1988).³⁸ Despite these advancements, reproducibility was initially hampered by low concentrations and uncontrolled growth of nanoparticles in colloidal suspensions. The introduction of a revolutionary hot injection process for the production of CdE (E = S, Se, Te) nanocrystals by Bawendi *et al.* was a big step forward for colloidal semiconductors.³⁹ Coordination ligands and a high reaction temperature allowed for the synthesis of monodisperse nanocrystals of the right size. The formation of monodisperse nanocrystals with appropriate size was made possible through the use of coordinating ligands and a high reaction temperature. The ability to adjust the semiconductor bandgap *via* particle size modulation encouraged

others to investigate other categories of semiconductor nanocrystals, including chalcohalides,⁴⁰ metal halide perovskites,⁴¹ pnictides,⁴² and metal chalcogenides,⁴³ which include ternary semiconductors. The majority of research involving these CQDs, also known as nanocrystals, utilizes the same hot injection method concept as described by Bawendi *et al.* and coworkers.³⁹

This review article aims to provide a comprehensive and heuristic overview of CQDs, covering the recent advancements in the last few years that have led to notable improvements across a range of domains: optoelectronic devices (LEDs, solar cells, and photodetectors), analytical sensing (drugs, hazardous chemicals and pesticides, heavy metal ions, *etc.*), biomedical applications (bioimaging, biosensing, photothermal therapy, and drug delivery), and photocatalysis (photo redox organic transformations, H₂ and H₂O₂ production, CO₂ reduction, dye degradation, organic/inorganic pollutant degradation, and N₂ fixation) as shown in Fig. 2. Few review studies have adequately highlighted the critical importance of reaction precursors, synthesis procedures, ligand selection, the role of the addition of foreign material, *etc.* coupled with the underlying photophysical principles, even though several have independently covered the recent advances of CQDs in each domain without providing the significant role of the above-quoted criteria. These aspects are crucial for understanding why CQDs serve as versatile candidates across diverse applications. Additionally, we also report the most contentious fundamental questions concerning the photophysical properties of CQDs, including the excitation energy-dependent PLQY, fluorescence blinking origin, and the underlying mechanisms behind them. Furthermore, we also discuss "dark fractions", their formation factors, and their implications. The different techniques for enhancing CQD performance in optoelectronic devices like improving the hole transport layer (HTL) and electron transport layer (ETL), alloy shelling of CQDs, modification of interfaces between the ETL and CQDs or the HTL and CQDs along with the CQD matrix, development of hybrid ETL, *etc.* are addressed. In the analytical sensing section, we mention the role of ligands in sensing analyte molecules of interest along with an explanation for the need to sense them. The different synthesis strategies are outlined in the biomedicine section. Furthermore, in the catalysis portion, we discuss the role of the morphology of CQDs such as size, shape, *etc.* along with the mechanism involved in catalysis application. To provide a better understanding of the main objectives of this review, a road map is depicted as shown in Fig. 3. Furthermore, we also discuss current trends, future directions, and persisting controversies in each application. With this review study, we intend to further spark interest in CQDs and CQD-based composites by highlighting their many benefits across a wide range of applications.

2. Photophysical properties of CQDs

CQDs display distinctive and unique photophysical properties which include size and composition-tunable bandgaps, narrow

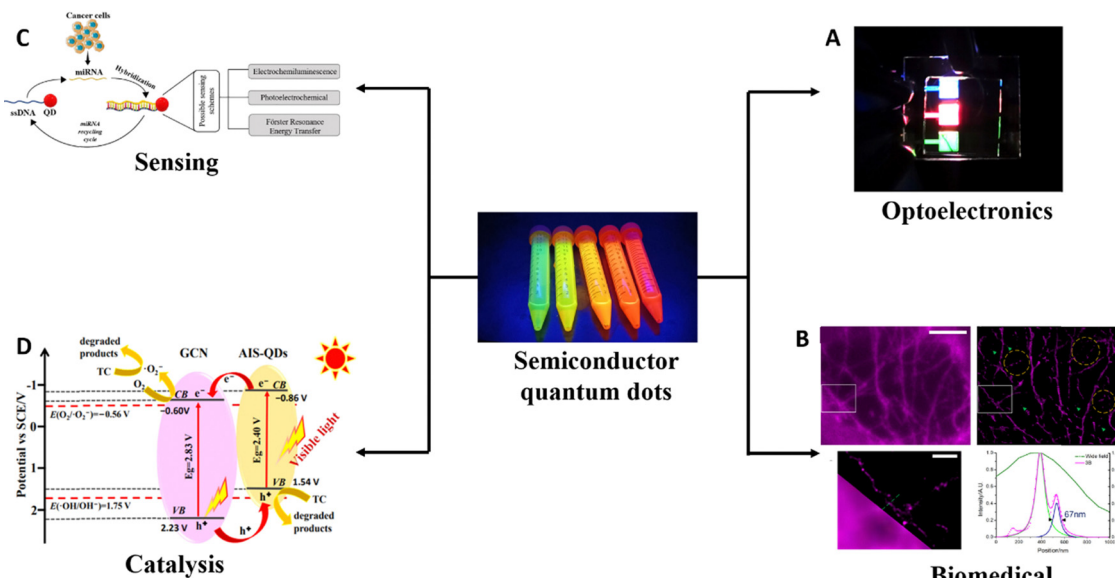


Fig. 2 Schematic overview of the CQD applications (A–D) in diverse fields.

linewidth emissions, tunable surface chemistry and charge transport, excitation-dependent photoluminescence quantum yields, fluorescence blinking, and “dark fractions”. These optoelectronic properties of CQDs are described below.

2.1. Size and composition-dependent bandgaps

CQDs have a bandgap (E_g) that is finely tunable throughout a wide range of energies, from the ultraviolet (UV) to the infrared (IR) by simply tuning their sizes. The bandgap of the parent bulk solid determines the lower bound of E_g . For CQD-based technologies, precise control over E_g is essential. This affects a

range of applications, including photovoltaic energy harvesting, lighting, displays, and lasers for communications, sensing, metrology, imaging, and medical diagnostic processes. Moreover, in addition to size modifications, compositional variations can also cause modifications in the emission spectra of CQDs. The ability to adjust the emission maxima to the near-infrared (NIR) region without significantly changing their size makes this composition-tunable emission method very useful for biological applications. As a result, this promotes improved CQD penetration into cells, increasing their usefulness in biological contexts.^{44–46} Fig. 4A illustrates the size-tunable

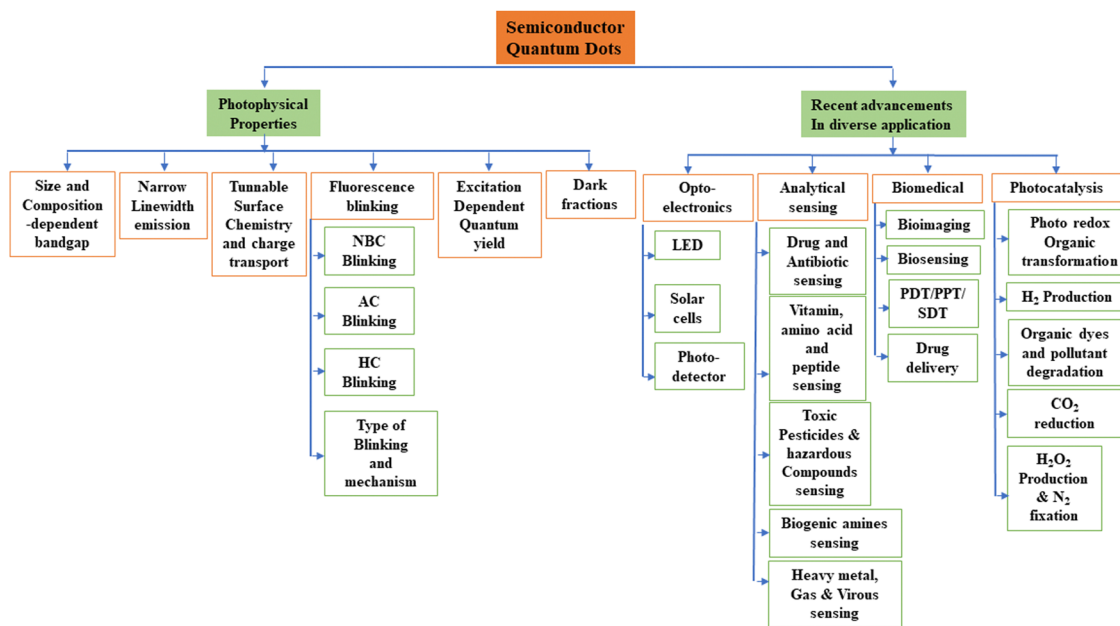


Fig. 3 The roadmap of key advancements of CQDs across the realms of optoelectronics, analytical sensing, biomedicine, and catalysis including their photophysical properties.

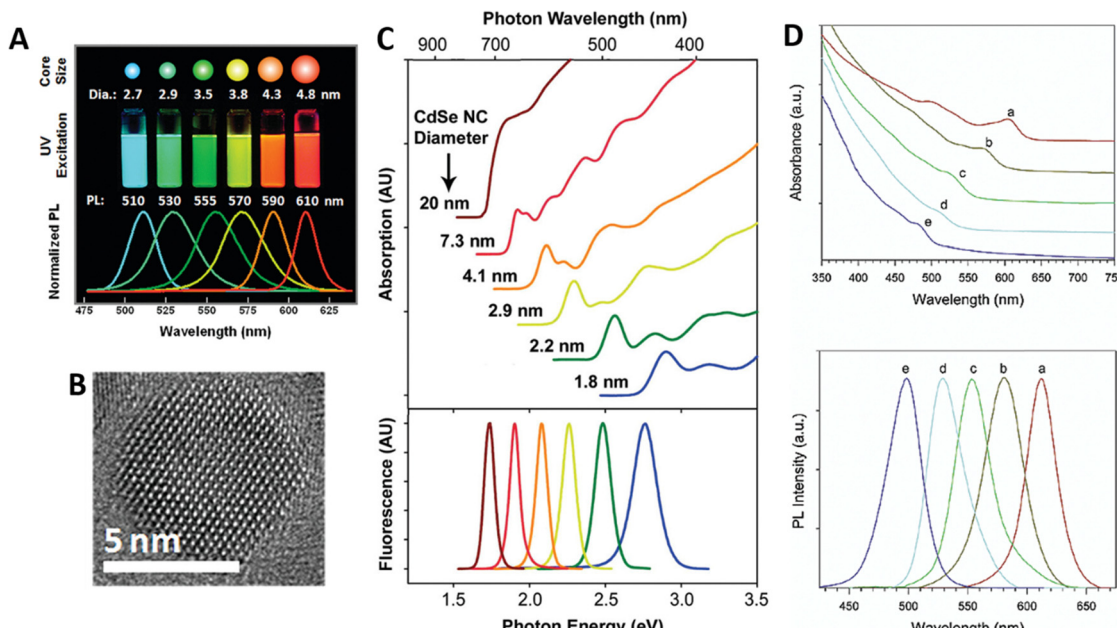


Fig. 4 Schematic representation of size and composition tunable emission spectra. (A) Size-tunable PL of CdSe CQDs. The photograph was taken under UV illumination (365 nm). (B) Transmission electron microscopy image of a CdSe/ZnS CQD. (C) Size-dependent absorption and fluorescence spectra of CdSe/ZnS core–shell CQDs. (D) Absorption and PL spectra of $Zn_xCd_{1-x}Se$ CQDs with different Zn mole fractions. Reproduced with permission from ref. 44. Copyright 2011 American Chemical Society. Reproduced with permission from ref. 45. Copyright 2010 American Chemical Society. Reproduced with permission from ref. 46. Copyright 2003 American Chemical Society.

emission and the corresponding TEM image of CdSe/ZnS CQDs is presented in Fig. 4B. Fig. 4C showcases the absorption and emission spectra of CdSe/ZnS core–shell CQDs with varying core sizes. Moreover, Fig. 4D demonstrates how tuning the bandgap of CdSe CQDs can also be achieved by varying Zn concentration. Thus, these visuals highlight the adaptability and potential of CQDs across a range of applications, by shedding light on their structural and spectral properties with changes in size and composition.

2.2. Narrow linewidth emission

The discrete, atomic-like structure of electronic states in highly monodisperse CQD samples results in a small ensemble emission line width at room temperature of 20 to 80 meV [full width at half maximum (FWHM)], which is close to a single-dot line width.⁴⁷ This makes it possible for next-generation displays to achieve the high color purity required to meet performance goals. Near-unity photoluminescence quantum yield (PLQY; the amount of emitted photons per absorbed photon) is also attained by the best CQD samples.⁴⁸ Commercial TVs and displays have made use of the CQDs' bright and narrowband emission. Luminescent solar concentrators (LSCs), which serve as large-area sunlight collectors for photovoltaic modules, also benefit from these qualities.⁴⁹ The discrete nature of CQD electronic states is a significant advantage in lasing applications. The desired ground-state transition is concentrated by the steep density of states, and the thermal depopulation of the emitting band-edge states is hindered by the vast spacing between quantized energy levels.⁵⁰ Commercial CQD lasers are now being developed using In(Ga)As/GaAs CQDs based on the S-K growth mode.⁵¹

2.3. Tunable surface chemistry

Because of their enormous surface-to-volume ratio, CQDs are very environment-sensitive. Usually, molecules or ions with various morphologies and functional groups terminate the surfaces of CQDs.⁵² This provides a way to control how CQDs interact with their surroundings. CQDs can be utilized as optically addressable bio labels and analytical sensors by attaching them to proteins, antibodies, or other species.⁵³

2.4. Tunable charge transport

The capacity of charge carriers to traverse interparticle barriers dictates the ability of CQD assemblies to pass current. The charge carrier mobilities of CQD solids are often lower than those of III-Vs semiconductors (10^2 – $10^3\text{ cm}^2\text{ V}^{-1}\text{ s}^{-1}$) in the solution phase, with values commonly falling in the range of $10^{-1}\text{ cm}^2\text{ V}^{-1}\text{ s}^{-1}$. The relationship between carrier confinement, CQD interfacial characteristics, and electronic coupling is complicated in most CQD solids. Higher mobility through enhanced CQD coupling is frequently followed by a rise in intra-gap tail states, which reduce the CQD solid's electronic gap. Charge-transport barriers are frequently formed between consecutive dots by the passivating layers, which are used to reduce intra-gap states and prevent CQD fusion. For a single carrier type, mobilities as high as $10\text{ cm}^2\text{ V}^{-1}\text{ s}^{-1}$ have been achieved by managing these conflicting tendencies.^{54,55} CQD solids that exhibit balanced charge transport for both polarities (n and p) and preserve discrete quantum-confined electronic states have recently made significant strides.⁵⁶

2.5. Fluorescence blinking

Emission from a single molecule or nanocrystal (NCs) is frequently irregular when subjected to constant photoexcitation. This intermittency, often known as blinking, occurs reversibly between the emissive state (“ON” or “Bright”) and the non-emissive state (“OFF” or “Dark”) when an electron or a hole gets trapped in a “dark state” or “trap state” (a state which blocks radiative recombination of excitons) which is often known as a “grey state”. Blinking, thus, is a variation in photoluminescence intensity related to the nanocrystal’s time at the single particle level as shown in Fig. 5a. The corresponding “ON” and “OFF” time distributions are shown in Fig. 5b. The probability distribution of the “OFF”-state, $P(\tau_{\text{off}})$ with respect to the “OFF”-state duration (τ_{off}) typically follows inverse power law distributions

$$P(\tau_{\text{off}}) \propto \tau_{\text{off}}^{-\alpha} \quad (1)$$

where α is the power-law coefficient with a value between 1 and 2. This power-law distribution indicates widely distributed off-switching rates.

However, the probability distribution of the “ON” state, $P(\tau_{\text{on}})$ with respect to the “ON” state duration (τ_{on}), follows truncated power-law distributions

$$P(\tau_{\text{on}}) \propto \tau_{\text{on}}^{-\alpha} \cdot e^{-\tau/\tau_c} \quad (2)$$

where τ_c is the cross-over time or truncation time which indicates the start of exponential truncation.

Blinking persists until a one-step photobleaching event takes place, which causes the NCs to permanently change into a non-emissive species.^{57,58} Blinking was first observed by Nirmal *et al.* while studying isolated CdSe nanocrystals (NCs) using steady-state laser stimulation.⁵⁹ It has been observed that CQDs with multi-shell or thick shells show less blinking and greater “ON” time than the bare CQDs, and the thick potential

barrier surrounding the nanocrystal core ought to prevent carrier escape toward the surface. Numerous research teams have seen blinking in various NC and nanowire kinds at different temperatures since this first finding. A lot of studies have seen blinking in various NC and nanowire kinds at different temperatures since this first finding.^{60,61} Even at extremely low temperatures (4 K), NC blinking dynamics are remarkably recorded, ruling out thermally triggered processes and offering crucial information on the underlying physical mechanism. Let us first discuss the many sorts of blinking seen in CQDs before reviewing the models that have been offered to explain blinking characteristics.

NBC blinking. In a transient “shallow trap state”, a charge carrier quickly relaxes *via* a nonradiative pathway prior to the generation of another exciton. In this instance, PL blinking is caused by a time-dependent fluctuation in the carrier trapping rate. NBC blinking is the term for the photoluminescence variation caused by nonradiative band-edge carrier (NBC) recombination mediated by these “shallow trap states”.⁶²

AC blinking. A prolonged duration of trapping the charge carrier results in the charging of the nanocrystal. This charged nanocrystal absorbs another photon, producing an exciton that turns the system into a trion. Two scenarios can occur in this case: (i) the exciton can recombine radiatively at a rate that is nearly twice as rapid as neutral exciton recombination; (ii) the exciton recombination energy can be non-radiatively transferred to a third carrier (a process known as Auger recombination). AC blinking is the name given to PL blinking resulting from both nonradiative and radiation-mediated trion-mediated recombination.^{62,63}

HC blinking. In addition to these two procedures, PL blinking may also result from trapping the heated carrier before it relaxes to the band boundary. This results in a considerable reduction in PL intensity without any meaningful change in a

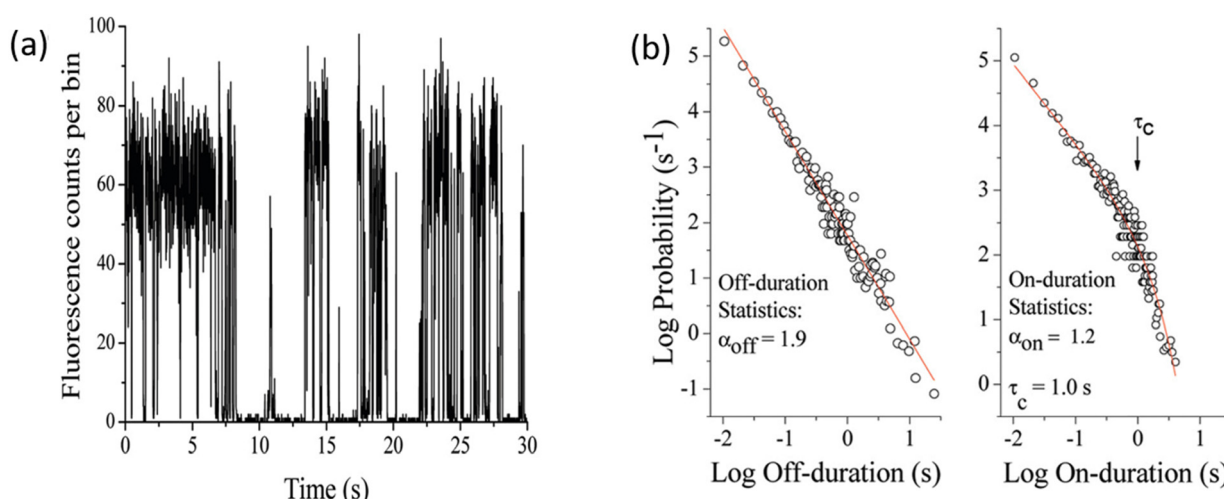


Fig. 5 Random blinking of colloidal nanocrystals. (a) A fluorescence blinking trajectory from a single CdSe/ZnS core/shell CQD. The fluorescence counts are binned into 10.5 ms time bins. (b) Probability density distribution histogram of “ON” and “OFF” time. [α is a power-law coefficient with a value between 1 and 2 and τ_c is the cross-over time or truncation time which indicates the start of exponential truncation]. Reproduced with permission from ref. 57. Copyright 2011 American Chemical Society.

lifespan, since the trapped hot carrier relaxes swiftly (through a non-radiative recombination mechanism) prior to the formation of another exciton. The term “hot carrier (HC) blinking” refers to this unusual occurrence.⁶³

Two methods have emerged in the literature for synchronizing the non-fluorescent intervals observed during blinking with this charge carrier entrapment. The first method, known as Type I models here, is based on the charging model, which holds that charge trapping leaves the nanocrystal core effectively charged. Over the charged nanocrystal, auger recombination is an effective non-radiative recombination mechanism that produces a low fluorescence quantum yield over a period of time determined by the lifetime of the trapped charge. The second method, which we will call Type II models from here on, is predicated on the trapped charge’s ability to quickly and non-radiatively recombine with its countercharge following each excitation event. Here, a rapid charge-trapping rate induces poor fluorescence quantum yield, and time-dependent variations in that trapping rate lead to intermittency. Research is presently underway to determine the specifics of these generalized theories as well as the causes of the greatly dispersed kinetics of these processes.

Type I blinking model. The formation of a hole in the valence band (VB) and an electron in the conduction band (CB) originates from charge separation in the nanocrystal under continuous photoexcitation. An exciton is made up of these electron–hole pairs that are firmly bonded together in the nanocrystal through electrostatic attraction. The nanocrystal emits fluorescence (Fig. 6a) when this exciton recombines radiatively, *i.e.* when the electron recombines with its neighboring hole in the radiative channel. Continuous photon absorption that produces excitons and then radiative recombination maintains the emissive “ON” state (Fig. 6b). Charge carriers are trapped in “trap states” by thermal ionization or photoionization, which causes the change from the “ON” to the “OFF” state (Fig. 6c). These “trap states” are considered to be close to either the VB or the CB. The nanocrystal’s center acquires a positive or negative charge if the electron or hole is trapped respectively in the “dark state” or “trap state”. Subsequently, within the nanocrystal core, a fresh exciton forms as a result of continuous photoexcitation. Then, at the nanocrystal core, the freshly formed exciton and a single charge carrier combine to form a three-particle system called a trion. The trion can have a positive or negative charge, depending on

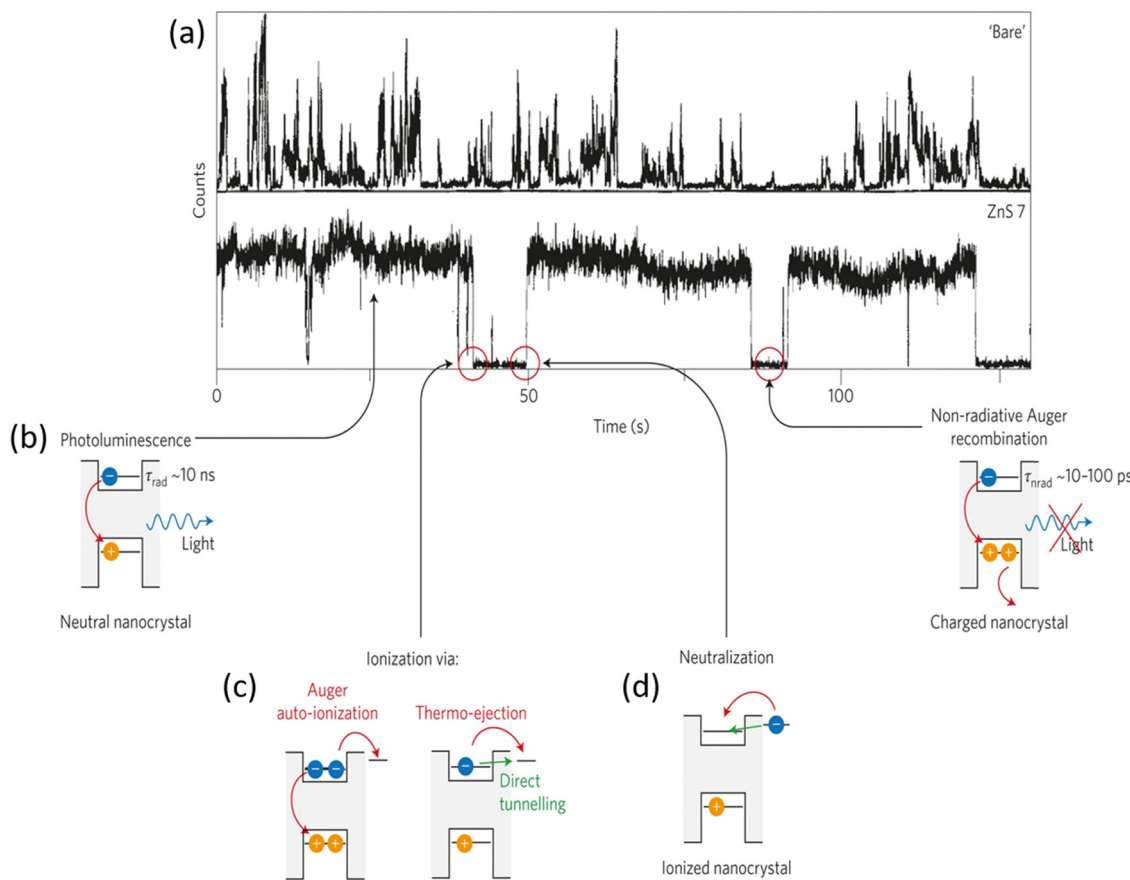


Fig. 6 Schematic depiction of the type-I blinking mechanism. (a) Typical fluorescence trajectory measured in a single CdSe nanocrystal of 2.1 nm radius. (b) Schematics of neutral and charged NCs. Optical excitation of the neutral NC leads to PL with a radiative decay time τ_{rad} on the order of 10 ns; excitation of the charged NC leads to fast non-radiative Auger recombination with a decay time τ_{nrad} on the order of 10–100 ps. Arrows display the phenomena that control fluorescence trajectory measured in a single CdSe CQD. (c) The process leads to nanocrystal ionization. (d) Neutralization of charged NCs. Reproduced with permission from ref. 58. Copyright 2016 Springer Nature.

the charge of the lone carrier. Tens of MV cm^{-1} is the approximate magnitude of the electric field produced by the surplus charge inside the nanocrystal core. Through quick energy transfer to the single charge carrier in the nanocrystal core, this electric field causes non-radiative recombination of the exciton – a process called the Auger mechanism. The Auger recombination mechanism keeps the nanocrystal in a non-emissive “OFF” state. The transition from the “OFF” state back to the “ON” state occurs when the trapped charge returns to the core of the nanocrystal, allowing for exciton recombination to take place radiatively (Fig. 6d).^{58,64}

Type II blinking model. According to the Type II model, fluorescence blinking is caused by variations in the carrier (hole or electron) rate over time. Continuous photon absorption cycles, which continually produce excitons and fluorescence recombination, occur when the carrier trapping rate is slower than the fluorescence rate (Fig. 7a). The “ON” state gives way to the “OFF” state when the trapping rate far surpasses the fluorescence rate. The nanocrystal absorbs photons to produce excitons while it is in the “OFF” state. Following this, non-radiative recombination with the trapped electron (or hole) and quick removal of the electron (or hole) to a “trap state” take place (Fig. 7b and c). When charge carrier trapping becomes noticeably slower than the rate of fluorescence, the system will

switch back from the “OFF” to “ON” state (Fig. 7d). Multiple recombination centers (MRC) are a theory put out by Frantsuzov *et al.* to account for the variable carrier trapping rate in Type II blinking models. They proposed that the surface of the nanocrystal had many carrier trapping sites that may alternate between active (high trapping rate) and inactive (minimum trapping rate) conformations. These sites are assumed to be interface or surface atoms bouncing between two quasi-stable locations under the influence of light. When many “trap states” are concurrently in the active conformation, fast trapping rates and off periods are anticipated.⁶⁵

2.6. Excitation energy-dependent quantum yield

As a quantitative indicator of fluorescence quality, photoluminescence quantum yield (PLQY) has become a crucial spectroscopic parameter for the application of CQDs. CQDs with excellent photoluminescence and photostability, alongside a wide absorption spectrum and an emission maximum that is independent of excitation energy, show promise as materials for a range of technological applications, from bioimaging to light-emitting devices. These CQDs can produce photoluminescence at any wavelength thanks to their wide absorption spectrum. Although the maximal emission of CQDs is independent of excitation energy, the PLQY is shown to be dependent

Type II Blinking Models:

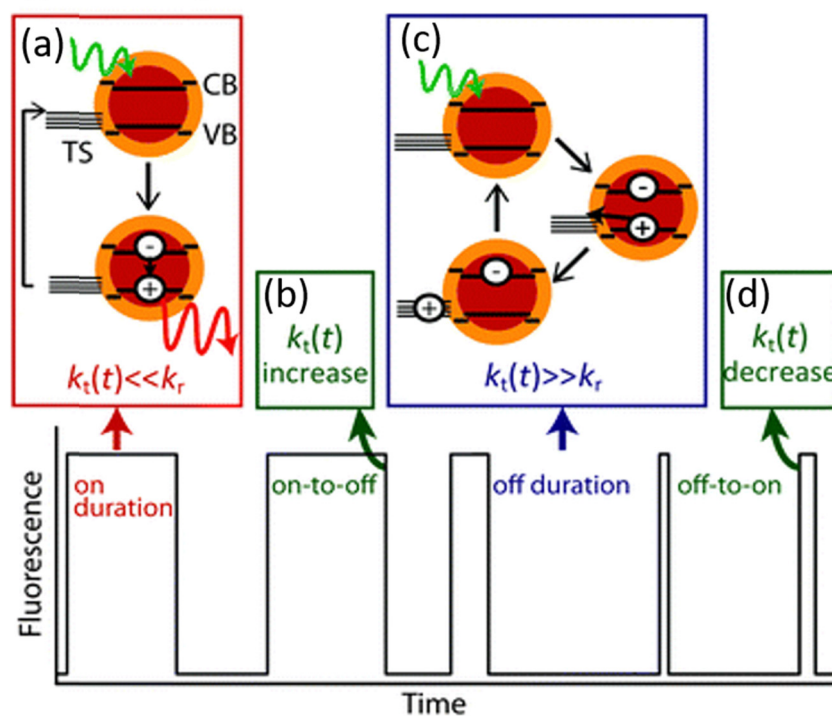


Fig. 7 Type II flashing model schematic description. $K_t(t)$ and K_r stand for carrier trapping rate and fluorescence recombination rate, respectively (here hole trapping has been taken into consideration). In the context of nanocrystals, VB, CB, and TS stand for the valence band maxima, conduction band minima, and “trap states” respectively. (a) In an ‘ON’ state, $K_t(t) \ll K_r$ and the nanocrystals recombine fluorescence and exciton generation through absorption cycles. (b) Switching from on to off happens when $K_t(t)$ increases and surpasses K_r . (c) In an ‘OFF’ state, $K_t(t) \gg K_r$, and the nanocrystal alternates between absorbing to produce an exciton, trapping holes, and then quickly recombining the electron with the hole that was trapped. The nanocrystal returns to its initial neutral state prior to the subsequent absorption event. (d) Switching from “OFF” to “ON” happens when $K_t(t)$ falls and becomes less than K_r . Reproduced with permission from ref. 65. Copyright 2013 Royal Society of Chemistry.

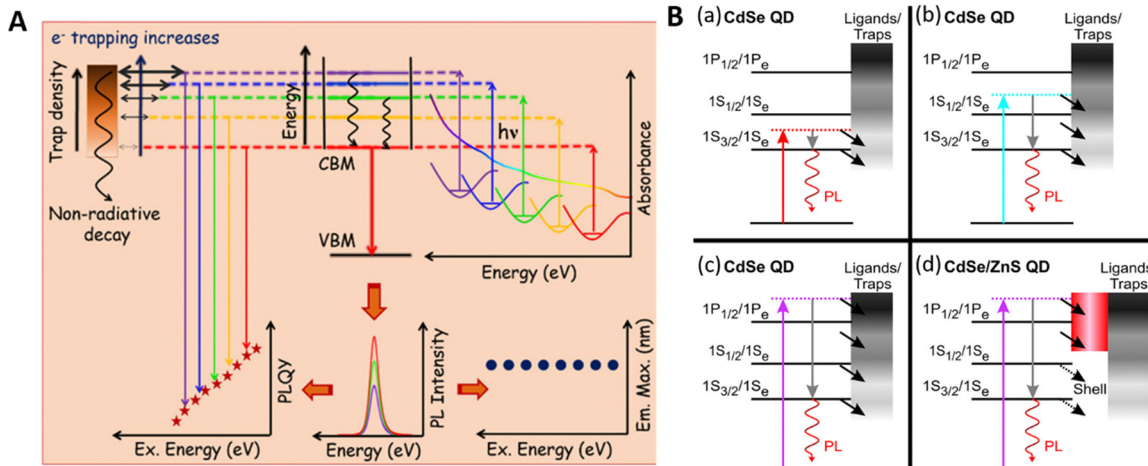


Fig. 8 (A) Excitation energy dependent PLQY of CQDs with respect to excitation energy. PLQY decreases as excitation energy increases because the “trap state” density falls towards the band edge. (B) Schematics representing the opposing nonradiative relaxation paths in CQDs that lower the PL QYs. (a) Coupling to surface traps and ligands can compete with relaxation to the $1S_{3/2}/1S_e$ states and give rise to variable PLQYs after photoexcitation of CdSe CQDs to energies slightly above the lowest states of the hole and electron. (b) and (c) As the excitation energy increases, the number of nonradiative states increases and the proportion of charge carriers relaxing to the $1S_{3/2}/1S_e$ states drops. (d) Type-I heterostructure of CdSe/ZnS CQDs reduces the routes to the ligands and traps, particularly at lower excitation energy. But still, electrons can interact with the “trap state” at excitation energy close to the $1P_{1/2}-1P_e$ transition because of the conduction band offset between the CdSe core and ZnS shell. [QD in the figure represents CQD]. Reproduced with permission from ref. 67. Copyright 2013 American Chemical Society. Reproduced with permission from ref. 71. Copyright 2022 American Chemical Society.

on excitation energy (Fig. 8A).^{66–73} Photoluminescence excitation (PLE) measurements were used to reveal excitation energy-dependent (EED) PLQYs, which were first shown by Hoheisel *et al.*⁶⁶ These measurements showed a monotonic drop in CdSe NC PLQY when ensembles were stimulated to the blue of their band edge. The reason for this decrease is explained as particles being excited into a range of states that differed from constrained NC states. Hoy *et al.*'s further research revealed that CdSe NC PL QYs decreased as excitation energy increased, with a notable ~90% drop of ~1 eV above the band gap. They suggested that increasing “trap-state” densities, which are the cause of EED PLQY, leads to increased nonradiative carrier trapping above NC band boundaries. Utilization of shelling on CQDs can prevent electron trapping to an extent that results in a higher PLQY than those of bare CQDs, but no change in EED PLQY will be observed (Fig. 8B).⁶⁷ By using coordinated PLE and absorptance measurements, Li *et al.* further corroborated EED PLQY. They also proposed that higher hot carrier trapping above NC band margins is caused by higher carrier trapping rates, which are a result of increasing free energy differences for trapping.⁶⁸ Roy *et al.* extended this investigation to CdSe-based CQDs where they suggested a decrease in the extent of hot electron trapping and an increase in the extent of hot hole trapping as the excitation energy is lowered. As a consequence, the PLQY is found to be higher at longer wavelengths or lower excitation energy.⁶⁹ Additionally, Chayan K. De *et al.* observed that the decrease in the PLQY value at longer wavelengths is less pronounced for InP-based core alloy system CQDs as compared to that of CdSe-based core alloy CQDs, attributed to the excitation taking a longer time to cool down in InP-based CQDs and thus being more prone to getting trapped resulting

in less PLQY at shorter wavelengths.⁷⁰ Recently, another study led by Roy *et al.* demonstrated that the EED PLQY trend is followed by both InP-based core and core alloy shell CQDs. They suggested that when the excitation energy increases, there is a greater chance of charge carrier interaction with “trap states”, which lowers the proportion of “ON” events and, therefore the PLQY.⁷¹ Nonetheless, it has been discovered that sometimes hole trapping can be beneficial for increasing the PLQY for CuInS₂-based core/alloy-shell CQDs while maintaining the same EED PLQY trend.⁷²

Regarding EED PLQYs, there is conflicting evidence suggesting that they might be artifacts resulting from measurement mistakes. According to Toni *et al.*, EED PLQYs are caused by excess surface ligands and NC aggregates in the solution. This can cause deceptive discrepancies between the PLE and related absorptance spectra and scattering losses in PLE measurements at short excitation wavelengths. Toni *et al.* discovered no indication of EED QYs after washing NC ensembles to eliminate scattering sources, which lends support to this.⁷⁴ Geißler *et al.* provided evidence in favor of this argument by presenting absolute, integrating sphere-based PLQY measurements that revealed excitation wavelength-independent PLQYs in CdSe NCs.⁷⁵

2.7. Dark fractions

Similar to fluorescence blinking and excitation energy, PLQY is likewise affected by “dark fractions”. CQDs that exhibit non-radiant or non-emitting behavior and remain nonemissive even after being exposed to light are referred to as “dark fractions”.^{76–81} “Dark fractions” in CQDs are formed due to a number of circumstances. For instance, excited charge carriers

may be trapped in nanocrystals due to the existence of “trap states” or defects, which would cause non-radiative decay. Quenching of emissions can also be brought on by non-luminescent aggregates or clusters that are created during synthesis at high temperatures or concentrations of starting ingredients.⁷⁷ Environmental elements that are important for the generation of “dark fractions” include pH, solvent, capping ligands, *etc.*^{80,81} Several investigations have been carried out to understand the production of dark particles and the parameters that affect them. To illustrate how dark fractions affect ensemble PLQY, Y. Ebenstein *et al.* addressed the topic and pointed out that a rise in “dark fractions” causes an increase in ensemble PLQY.⁷⁷ Thomas Pons *et al.* confirmed the coexistence of bright particles and “dark fractions” in colloidal solutions and their relative ratio regulating the PLQY of CQDs. They did this by doing the single-particle analysis to connect ensemble PLQY with the emission of single CQDs.⁷⁸ Jie Yao *et al.* revealed that the brightness of CQDs is strongly related to “bright and dark fractions”, which has a substantial influence on bioimaging applications. They also characterized the presence of “dark fractions” in water-soluble CdSe/ZnS CQDs along with their blinking behaviors.⁷⁹ To better understand “dark fraction” generation and associated pH change, Nela Durisic *et al.* undertook a pH-dependent investigation and observed that dark particles are formed more at lower pH values (Fig. 9A).^{80,81} They found that the production of “trap states” is facilitated by H⁺ ions and that shorter “ON” periods and more electron trapping occur at lower pH levels when “bright and dark state” overlap increases (Fig. 9B).⁸⁰

(1) **Optoelectronics.** Effective charge transfer and the formation of a variety of electronic junctions with metals and

dielectrics are made possible by the semiconducting characteristics of CQDs. Because of their adaptability, CQDs are a great material to use in the development of optoelectronic devices. Furthermore, the colloidal nature of CQDs opens up a variety of inexpensive, solution-processable pathways for the production of devices. The most striking feature of CQDs, though, is how versatile they are in terms of both their optical and semiconductor characteristics. This allows for the manufacturing of customized CQDs for a wide range of optoelectronic devices.⁸² The first use of CQDs as an electronic material was exploited in 1994 by Colvin *et al.* and co-workers. They designed the first CQD-based light-emitting diode (CQD-LED) that sparked the development of a whole new class of photonic devices. Exactly three orders of magnitude less external quantum efficiency was demonstrated by these initial CdSe CQD-based LEDs than by contemporary CQD-based LED examples.⁸³ The development of effective CQD synthesis techniques, optimization of device design, and enhancement of charge transport layer characteristics resulted in the fast growth in CQD-LED efficiency. Other significant CQD-based optoelectronic devices, such as photovoltaic cells and photodetectors, were subsequently inspired by this. These days, CQD-based photodetectors have filled a critical gap in sensitive NIR detection, while CQD-based solar cells are one of the most promising options for third-generation photovoltaics. The basic ideas behind how CQDs function in each of these applications differ slightly depending on the kind of device. When used to display technology, narrow CQD emission and thus pure color are essential; yet, when using CQDs as a light source, a wide emission spectrum is preferred. A high photoluminescence quantum yield (PLQY) is essential

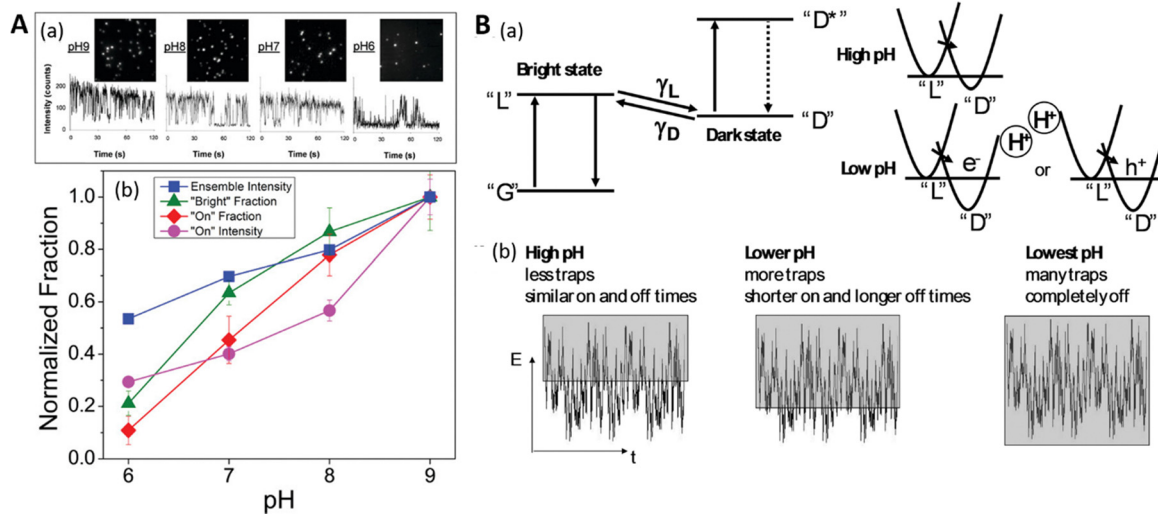


Fig. 9 (A) pH-Dependent single particle investigation. (a) Bright particle number fluctuations at different pH values. The corresponding fluorescence trajectory at the specified pH is displayed in the traces beneath each image. (b) Comparison of the ensemble and single particle fluorescence outcomes at multiple pH. The “bright fraction” of CQDs in the sample is shown by green triangle symbols, which are calculated as the proportion of individual CQDs that emit light at any given time during the whole film. Red diamond symbols are used to measure the average number of CQDs that are “ON” for a 50 ms frame (also known as the average “ON fraction”). The relative average is shown by the magenta circle symbol “ON Intensity.” For ease of comparison, all of the results are normalized to the CQDs measured in pH 9 solution. (B) “Dark fraction” formation mechanism. At lower pH, the overlapping area of the “dark state” and “bright state” is more and high trapping of charge carriers (a). Variation of “ON” and “OFF” duration with respect to pH (b). Reproduced with permission from ref. 80. Copyright 2009 American Chemical Society. Reproduced with permission from ref. 81. Copyright 2011 American Chemical Society.

for both activities. As a result, LEDs use a wide variety of core/shell CQDs. Blinking suppression and Auger recombination are also brought about by the softening of the alloyed CQDs' confinement potential.⁸⁴ Thereby, CQDs that are suited for LED applications combine the synthesis of an alloyed core with the application of precise shelling. Conversely, the design of effective photovoltaic systems depends critically on a high extinction coefficient across a large spectral range. In the meantime, applications involving photodetection often need a particular sensitivity toward significant portions of the electromagnetic spectrum. Since "midgap states" lower carrier mobilities and excited state duration, which are crucial for device performance, clearing the bandgap from "trap states" is a crucial prerequisite for effective CQD-based photovoltaics.⁸⁵ On the other hand, the "midgap states" found in CQDs may serve as efficient sensitizing centers for photodetectors, and these same "midgap states" can be used in photoconductors to provide significant photoconductive gain and sensitivity.⁸⁶ Now, we are going to explore the latest advancements in colloidal CQD-based optoelectronic devices, emphasizing three key components: LEDs, photovoltaic (PV) cells, and photodetectors.

(*I*) *CQD-based LEDs.* The injection of electrons and holes into a thin layer of light-emitting CQDs is the fundamental mechanism of a CQD-based light-emitting diode (CQD-LED). Radiative recombination takes place when electrons and holes travel through the respective charge transport layers to reach the CQD layer under applied bias. This produces photons with an energy equal to the CQD bandgap. Colvin and associates created the first CQD-LED in 1994.⁸³ To date, research has focused on a few of the special qualities of semiconductor CQDs, such as tunable and sharp fluorescence, photo-stability, and soluble processing. The LED was made up of p-*para* phenylene vinylene (PPV) and CdSe CQDs that were positioned between an ITO and an Mg electrode. The discovery established a new area of growing research even though the external quantum efficiency (EQE), which is the number of radiated photons per number of electrons put into an LED, did not reach 0.01%. A low PLQY of quantum dots was the main cause of the first CQD-LEDs being reported as having low EQEs. Since then, a great deal of strategic work has been done to increase the PLQY as in these early stages of synthetic technique development, CQDs suffered from a range of surface defects, which acted as traps for excitons and reduced the PLQY. These methods include core-shelling,^{87–92} alloying,⁹³ alloy-shelling,^{94,95} addition of foreign solvent or substrate,⁹⁶ ligand exchange or passivation^{97–100} and ligand cleavage¹⁰¹ etc. as described in Table 1 along with external quantum efficiency (EQE). Progress in synthetic techniques made it possible to produce CQDs with much greater PLQYs and, therefore, to reduce the thickness of the emitting layer in CQD-LEDs to provide better charge injection and transport and led to the creation of CQD-LEDs with CQD emitting monolayers.

Recently, Haobing Zhao *et al.* employed InP multishell CQDs for narrow-bandwidth LEDs. They synthesized InP/ZnSeS/ZnS multishell CQDs by growing the inner-shell layer with a temperature-gradient solution growth (TGSG) strategy. The as-

synthesized CQDs exhibited a high PLQY of 91% and a narrow full width at half-maximum (fwhm) of 36 nm. Additionally, quantum dot light-emitting devices (QLEDs) based on these CQDs demonstrate a narrow fwhm of 42 nm, marking the narrowest emission of green InP QLEDs from a safe phosphorus source. Further enhancements in the electron injection into the QLEDs, were achieved by inserting a thin layer of lithium fluoride (Fig. 10A), resulting in a peak external quantum efficiency (EQE) of 5.56%.⁸⁷ In another work, a quasi-shell-growth strategy (QS strategy) was applied to InP CQDs to form InP/ZnSe/ZnS CQDs for QLEDs. The PLQY of these CQDs was found to exceed 90% with a narrow emission linewidth of 36 nm. The quasi-ZnSe shell, formed by adsorption of Zn and Se monomers during InP nucleation, played a crucial role in suppressing Ostwald ripening, ensuring isotropic growth, and passivating defects in the InP core. The resulting QLED exhibited significantly enhanced luminous efficiency, high brightness ($15\,606\text{ cd m}^{-2}$), a peak external quantum efficiency of 10.6%, and a long operational lifetime exceeding 5000 hours. Nevertheless, they also exhibit significant color purity, charge balance, and film surface quality in the green QLEDs through the introduction of a thin polyvinyl pyrrolidone (PVP) interfacial layer.⁸⁸ Similar coating of InP CQDs with thick layers of ZnSe and ZnS shells was carried out to address charge delocalization issues and achieve a narrow size distribution. The purified NCs exhibited an intense and narrow emission spectrum in the red wavelength range (626–670 nm) with an emission quantum efficiency of 74% at 632 nm and 60% for far-red wavelengths of 670 nm. The NCs demonstrated a relatively long average emission lifetime of 50–70 ns. InP/ZnSe/ZnS CQDs were successfully used as the emissive layer in red-emissive LEDs, achieving an external quantum efficiency (EQE) of 1.16%, a luminance of 1039 cd m^{-2} , and a current efficiency of 0.88 cd A^{-1} .⁸⁹ In another study, monochromatic LEDs were developed using on-chip color conversion with InP-based InP/ZnSe/ZnS CQDs, achieving a consistent output spectrum approximately 45 nm wide. The CQDs, characterized by a near-unity PLQY, demonstrated a color conversion efficiency exceeding 50%, exhibiting minimal intensity roll-off and a wavelength shift at higher driving currents. The efficiency was largely limited by package losses, with wall plug efficiencies reaching up to 30% (Fig. 10B).⁹⁰ Similar ZnSe and ZnS shelling was also incorporated by Jingwen Feng *et al.* but on ZnSeTe CQDs. The fabricated LEDs with ZnSeTe/ZnSe/ZnS CQDs resulted in a peak current efficiency of 11.8 cd A^{-1} and a chroma efficiency of 72, demonstrating a 2.2 times improvement compared to the control device.⁹¹ Manuela De Franco *et al.* presented a NIR LED based on InAs/ZnSe CQDs. The LEDs achieved a record external quantum efficiency (EQE) of 5.5% at 947 nm and demonstrated an operational lifetime of approximately 32 hours before reaching 50% of their initial luminance.⁹² An ultrathin indium sulfide (InS) shell was constructed to passivate electron vacancies and convert donor/acceptor level concentrations of Zn-Ag-In-Ga-S CQDs (Fig. 10C). The optimized In-rich 2-layer InS structure prevented further surface vacancy formation, enhanced radiative recombination, and achieved a significant

Table 1 Performance summary of CQD-based LEDs and techniques to enhance the PLQY of CQDs

Materials	Method to enhance PLQY	PLQY value (%)	EQE (%)	Ref.
InP/ZnSeS/ZnS CQDs	Temperature-gradient solution growth (TGSG) strategy	91	5.56	87
InP/ZnSe/ZnS CQDs	Quasi-shell-growth (QS) strategy	90	10.6	88
InP/ZnSe/ZnS CQDs	Quasi-shell-growth (QS) strategy	—	1.16	89
InP/ZnSe/ZnS CQDs		Near unity		90
ZnSeTe/ZnSe/ZnS CQDs	Core shelling	50% in solution	6	91
InAs/ZnSe CQDs	Core Shelling	—	5.5	92
Zn–Ag–In–Ga–S/InS	Core shelling	86.2	5.32	93
CuInS ₂ /ZnS CQDs	Core shelling	—	8.2	94
ZnCdSe/ZnSeS CQDs	Alloy shelling	~92 in solution and 84 in films	22.9	95
PbS CQDs	Surface engineering through surfactant addition	—	>0.4	96
CdZnSe/CdZnS/ZnS CQDs	Surface engineering through a carbocation-enabled ligand stripping approach	Pristine and CELS: red 82 and 97; green, 47 and 80; blue, 41 and 71	19.1 (red), 17.5 (green), 12.0 (blue)	97
Graded-alloy core/shell “giant” CQDs	Surface passivation strategy	>99 (near unity)	—	98
InP/ZnSe/ZnS CQDs	Foreign agent addition	Near-unity	22.2	99
ZnSeTe/ZnSe/ZnS CQDs	Ligand engineering	86.2	5.46	100
In ₂ O ₃ CQDs	Ligand engineering through direct optical patterning of colloidal hydrophobic nanocrystals (DOVE)	~19.0 (patterned CQD film); 43.7 (DOVE CQD film + ligand passivation)	2.9 (patterned CQD film); 5.6 (DOVE CQD film + ligand passivation)	101
InP/ZnSe/ZnS CQDs	Improvement of HTL	48	8.46	102
CdSe/ZnS CQDs	Improvement of HTL	—	25.19	103
InP CQDs	Improvement of ETL	—	15	104
ZnCdSe/ZnS CQDs	Improvement of HTL	—	Higher EQE at a low luminance compared with other HTLs	105
ZnSeTe CQDs	Phase tuning layer (PTL) incorporation	—	15.14	106
ZnTeSe-based CQDs	Improvement of HTL	—	10.1	107
PbS CQDs	Band offset improvement of HTL and the emitting layer	—	0.35	108
InP/ZnSe/ZnS CQDs	Modulation of the patterning process for LED fabrication	~60.0	~2.0	109
CdSe/CdS CQDs	Modulation of the patterning process	—	—	110
AgAuSe CQDs	Modulation of ETL/QD/HTL interfaces	—	15.8	111
PbS CQDs	Introduction of a binary CQD matrix	68 for 1.75 eV binary matrix	18.6	112

PLQY increase of 86.2%. They commented that their result was the highest EQE for red QLEDs to date, reaching 5.32%.⁹³ Li Jun Lim *et al.* followed both alloying and shelling strategies to produce LEDs, utilizing CuInS₂/ZnS CQDs with a high photoluminescence quantum efficiency (PLQE) of 65% at a long emission wavelength of 920 nm. Subsequently, they fabricated near-infrared (NIR) light-emitting diodes (LEDs) using these CQDs, achieving an external quantum efficiency (EQE) of 8.2% which is comparable to the best-reported PbS and InAs quantum dot LEDs.⁹⁴ Sometimes, alloy shelling, such as the use of ZnCdSe/ZnSeS CQDs with a continuous gradient alloyed core-shell structure, has been explored as an alternative to binary shells like ZnSe, ZnS, InS, etc. Liu *et al.* demonstrated QLEDs based on these CQDs, achieving an external quantum efficiency of over 20% across a luminance range of 200–90 000 cd m⁻². These QLEDs exhibited a remarkable T_{95} operation lifetime exceeding 20 000 hours at 1000 cd m⁻², along with impressive shelf stability (>100 days) and cycle stability (>10 cycles).⁹⁵ Now focusing on strategies like surface engineering and foreign substrates to improve the stability and PLQYs of CQDs for LED application, Fei Li *et al.* recently introduced a surfactant into the

system to enhance the stability and yield of PbS CQDs (Fig. 11A). They achieved highly stable PbS CQDs with significantly enhanced photoluminescence intensities by incorporating an octane thiol (OT) surfactant. This addition effectively suppressed surface traps and continuous oxidation of unstable (100) facets in PbS CQDs. The OT surfactant doubled the photoluminescence efficiency and improved stability. PbS-based QLEDs with a standard device structure demonstrated a breakthrough high radiance of 18.3 W sr⁻¹ m⁻² under a driving current density exceeding 2000 mA cm⁻². The effective passivation of surface traps with octane thiol surfactant and the suppression of coupling between excitons and surface states under large working currents were key factors contributing to this breakthrough in radiance.⁹⁶ Zhong Fu *et al.* presented a light-triggered, carbocation-enabled ligand stripping (CELS) approach for patterning quantum dot layer QLEDs. During CELS, photogenerated carbocations from triphenyl methyl chlorides removed native ligands of quantum dots (Fig. 11B), enabling microscale precision patterning. Chloride anions passivated surface defects and maintained photoluminescent quantum yields. CELS-patterned QLEDs exhibited high external quantum efficiencies (19.1%,

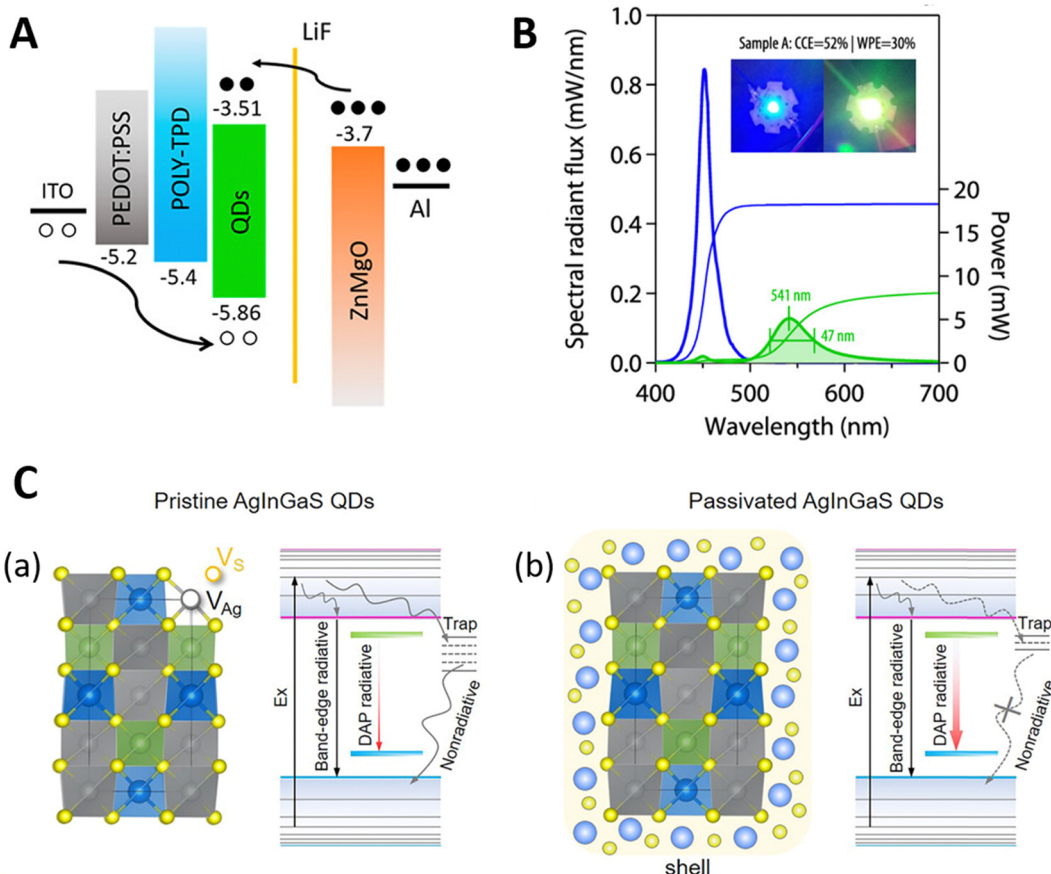


Fig. 10 (A) Device architecture with the corresponding energy band alignment of the QLED with a LiF barrier layer. The addition of a LiF thin layer as an electron injection layer improves the EQE. (B) Spectral radiant flux and emitted power measured on CQD on-chip LEDs formed using green emitting InP-based CQDs. (C) Schematic diagram of the crystal structure influencing the luminescence mechanism in pristine Ag–In–Ga–S CQDs with Ag and S vacancies (a) and passivated Ag–In–Ga–S CQDs (b). The passivation of the InS thin layer blocks the non-radiative recombination pathway through “trap state” blockage. Reproduced with permission from ref. 87. Copyright 2023 American Chemical Society. Reproduced with permission from ref. 90. Copyright 2023 American Chemical Society. Reproduced with permission from ref. 93. Copyright 2023 American Chemical Society.

17.5%, 12.0% for red, green, and blue, respectively) and a long operation lifetime (T_{95} at 1000 nits up to 8700 h), approaching records for non-patterned devices.⁹⁷ Next, Rahul Singh *et al.* focused on improving the optoelectronic properties of green-emitting graded-alloy core/shell “giant” quantum dots (g-CQDs) by passivating surface defects. The g-CQDs were treated with Z-type ligands (ZnCl_2 , CdCl_2 , and MgCl_2) to enhance the photoluminescence quantum yield (PLQY), lifetime, and stability. The Z-type ligands effectively passivated “trap states” on the CQD surface, leading to a significant improvement in PLQY. Notably, ZnCl_2 treatment resulted in the maximum enhancement, reaching near-unity PLQY. The treated g-CQDs exhibited superior photostability under continuous UV-light irradiation for 24 hours. Temperature-dependent stability was also studied. Finally, a green-emitting down-converted LED was successfully fabricated using ZnCl_2 -treated g-CQDs, showcasing their potential for display applications.⁹⁸ InP/ZnSe/ZnS core/shell-shell CQDs with a near-unity photoluminescence quantum yield were formed through the addition of ZnF_2 during synthesis. The ZnF_2 reacted with a carboxylic acid at high temperature to *in situ* generate HF, eliminating surface oxide impurities and

facilitating epitaxial shell growth. The resulting InP/ZnSe/ZnS CQDs exhibited improved characteristics compared to those synthesized with hydrofluoric acid, including a narrower emission line width and better thermal stability. Light-emitting diodes (LEDs) using these CQDs achieved a peak external quantum efficiency of 22.2%, high brightness, and extended operational stability.⁹⁹ Another alternative method is the decoration of bromide for modulating the surface states of CQDs. Zhishuai Zheng *et al.* aimed to reduce CQD surface defects by passivating unsaturated Zn for enhanced carrier radiative recombination and removing excess oleic acid through ligand exchange for efficient carrier transport (Fig. 11C). The bromide decoration resulted in a significant increase in PLQY from 39.7% to 86.2%, along with substantial improvements in QLED performance, including over sevenfold enhancement in external quantum efficiency (EQE) from 0.74% to 5.46% and a noticeable decrease in turn-on voltage from 6.7 to 5.9 V.¹⁰⁰ Yan Wang *et al.* mentioned and introduced a direct photoresist-free method called DOVE (direct optical patterning of colloidal hydrophobic nanocrystals) (Fig. 11D) for efficient patterning of colloidal nanocrystals (NCs) through light-induced cleavage of native

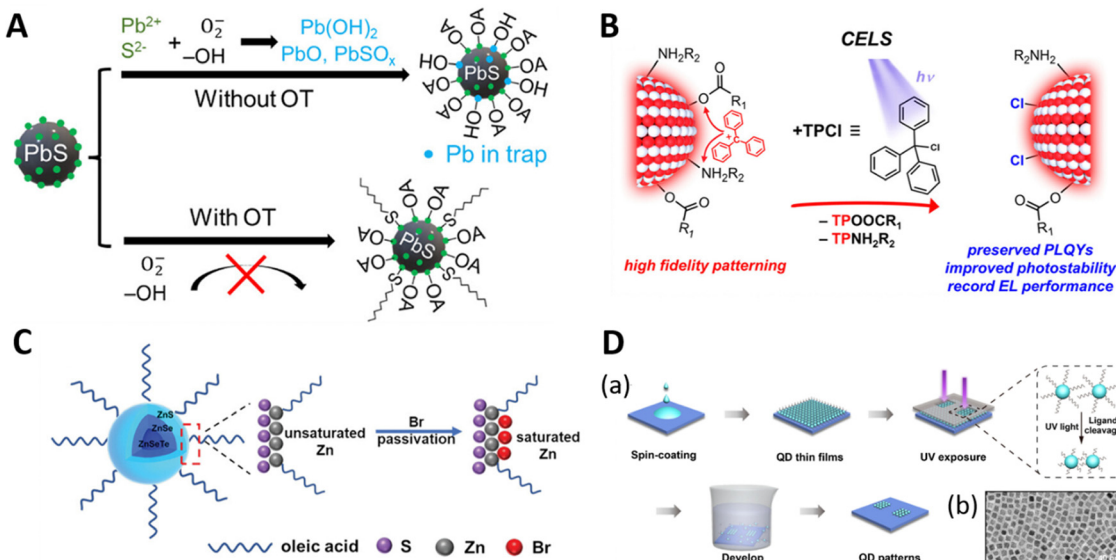


Fig. 11 (A) Schematic explaining the role of OT surfactant on enhancing the photoluminescence intensity of PbS CQDs by passivation of surface “trap states”. (B) Photochemistry involved in CELS. TPCl photodissociates under 254 nm and produces TP⁺ and Cl⁻. The Lewis acidic TP⁺ cations readily remove the native ligands (alkyl carboxylates or amines, abbreviated as R₂COO⁻ and R₂NH₂⁻, and also other conventional CQD ligands, such as alkyl thiols) from the CQD surface by forming corresponding adducts (TPOOCR₁ and TPNH₂R₂). This leads to a loss of colloidal stability and permits high-fidelity patterning. Cl⁻ anions then bind to the undercoordinated metal sites to passivate surface defects, thereby leading to CQDs with mixed ligands, unaltered PLQYs enhanced photostability, and record EL performance. (C) Schematic diagram of the Br passivation of unsaturated Zn on CQD surfaces. (D) Schematic illustration of the DOVE patterning process. Direct patterning process of In₂O₃ NC thin films using a quartz mask under UV exposure [185 nm (10%) and 254 nm (90%), power density = 30 mW cm⁻²] (a). TEM image of In₂O₃ CQDs (b). Reproduced with permission from ref. 96. Copyright 2023 American Chemical Society. Reproduced with permission from ref. 97. Copyright 2023 American Chemical Society. Reproduced with permission from ref. 100. Copyright 2022 John Wiley and Sons. Reproduced with permission from ref. 101. Copyright 2022 American Chemical Society.

organic ligands under UV exposure. The method allowed fine patterning of NCs with micrometer-scale features, and the resulting patterns enabled post-patterning ligand exchange. The feasibility of the DOVE method was demonstrated by fabricating patterned NC-based thin-film transistors (TFTs) and quantum dot light-emitting diodes (QLEDs). The In₂O₃ NC-based TFTs showed enhanced electronic performance upon ligand exchange, and ZnCl₂-treated green CQD patterns in QLEDs exhibited comparable electroluminescence performance to unpatterned devices.¹⁰¹

Further improvement of the electron and hole transporting layers (ETL and HTL, respectively) led to the next generation of CQD-based LEDs with a completely inorganic structure or a completely organic structure or hybrid structure. Lufa Li *et al.* utilized a self-assembled monolayer of 4-bromo-2-fluorothiophenol (SAM-BFTP) at the interface of the hole transport layer (HTL) and CQDs. This molecular dipole layer reduced the hole injection energy barrier and inhibited fluorescence quenching. Additionally, copper ions doped into phosphomolybdic acid (Cu:PMA) served as the hole injection layer (HIL). The resulting QLED achieved a maximum EQE of 8.46% and a luminance of 18 356 cd m⁻². The SAM-BFTP layer effectively balanced charge injection, passivated surface defects, and improved interfacial contact, leading to enhanced device performance and stability. The introduction of the Cu:PMA HIL further contributed to the improvements observed in the QLED.¹⁰² Next, a self-assembled hole HTL was prepared based

on a monolayer of poly[3-(6-carboxymethyl)thiophene-2,5-diy] (P3HT-COOH). This self-assembled monolayer replaced the commonly used hole injection structures, resulting in significantly improved QLED characteristics. The P3HT-COOH monolayer demonstrated benefits such as reduced hole injection barriers, effective blocking of electron leakage, and enhanced device stability. The QLEDs with this self-assembled monolayer exhibited lower turn-on voltages, high external quantum efficiency (EQE) of 25.19%, stable luminous intensity over 90% for 200 days, and durability exceeding 2 hours of operation under a luminance of 1000 cd m⁻².¹⁰³ Ya-Kun Wang *et al.* developed a novel bifunctional ETL (CNT2T, 3',3'',3''''-(1,3,5-triazine-2,4,6-trial)tris([1,1'-biphenyl]-3-carbonitrile)) to address issues in red InP quantum dot LEDs, particularly related to trap migration and luminescence quenching. CNT2T demonstrated superior performance, achieving a record external quantum efficiency (EQE) of 15% and a maximum luminance exceeding 12 000 cd m⁻² in red InP LEDs. The bifunctional ETL successfully passivated Zn²⁺ traps and prevented migration between layers, leading to a 1.4-fold EQE improvement compared to traditional ZnMgO controls.¹⁰⁴ Minh-Son Hoang *et al.* addressed phase separation in a hybrid poly(9,9-diocetylfluorene-*alt*-N-(4-sec-butylphenyl)-diphenylamine) (TFB) and polyvinylcarbazole (PVK) system used as a HTL for QLEDs. Without phase separation, the hybrid HTL significantly improved QLED performance, reducing turn-on voltage by approximately 47% and increasing brightness by around 37%. Eliminating

phase separation enhanced electroluminescent performance in both glass and flexible polyimide substrates, showing decreased turn-on voltage by 29–32% and increased brightness by 133–200%.¹⁰⁵ Furthermore, Cuixia Yuan *et al.* introduced a top-emitting structure for alloyed ZnSeTe CQD-based QLEDs to address issues of unsaturated emissions and broad spectra. The structure incorporated a transparent indium-zinc-oxide (IZO) top electrode and an IZO phase tuning layer (PTL) to modulate emission spectra and device efficiency. The resulting top-emitting QLED achieved saturated blue emissions beyond Recommendation ITU-R BT.709 standards, approaching Rec.2020 standards. The device demonstrated a high external quantum efficiency of 15.14%, which was further improved to 18.16% with SiO₂ nanosphere capping. The application of a 100 nm PTL effectively reduced surface plasmon polariton losses, resulting in an outcoupling efficiency of 41.2% at 478 nm. The developed top-emitting architecture enhanced color saturation and efficiency, yielding a high chroma efficiency of 123.¹⁰⁶ To address poor hole injection in blue ZnTeSe-based quantum dot light-emitting diodes (QLEDs), dual dipole layers were introduced using (2, 3, 6, 7, 10, 11 hexaazatriphenyl hexacarbonitrile) (HAT-CN) between the hole injection layer (poly(3,4-ethylene dioxythiophene):poly(styrene sulfonate) (PEDOT:PSS)) and the hole transport layer (polyvinyl carbazole) (PVK). The HAT-CN layer created dual dipole layers, reducing the hole injection barrier, decreasing hole defect density, increasing hole current, and improving effective radiation recombination of charge carriers. QLEDs with the HAT-CN layer exhibited a higher external quantum efficiency, increasing from 4.2% to 10.1%. Additionally, the *T*₅₀ lifetime nearly doubled at a high luminance of 2000 cd m⁻².¹⁰⁷ PEDOT:PSS was also used by Manman Gong *et al.* to optimize the band offset between the HTL and the emitting layer, achieving a maximum radiance of 16.14 W sr⁻¹ m⁻² at 6.15 V.¹⁰⁸

Modulation of the patterning process for LED fabrication has also been utilized to improve CQD efficiency in LEDs. Recently, Joon Yup Lee *et al.* introduced a high-resolution (>2000 PPI) multicolor patterning method for fabricating LEDs using InP CQD films through conventional photolithography

(Fig. 12A) with a positive photoresist (PR). To achieve solvent resistance, they deposited an ultrathin ZnO layer through atomic layer deposition. Their approach employed a positive PR with a photoacid generator, enabling side-by-side patterning of red- and green-colored InP-based CQDs. They successfully stacked each color CQD film. The process proved suitable for both thin (<100 nm) CQD films used in CQD-LED devices and thick (>1 μm) CQD films for color-conversion layers in backlights. Despite the patterning process, the CQD film performance remained unaffected, and the resulting CQD-LED devices exhibited unchanged performance post-patterning.¹⁰⁹ The maskless lithography was employed for direct CQD patterning in the QLED fabrication process to create 3D CQD pockets that acted as isotropic encapsulation of CQDs, preventing edge ingress from the lateral sides of CQD films. The patterning process involved three iterations of the identical printing steps: (1) casting the resin, (2) projecting the UV pattern, and (3) removing the uncured resin (Fig. 12B).¹¹⁰

Simultaneously, with the improvement of the CTL/HTL structure, the search for a more effective process to enhance the performance of QLEDs took place with the modification of the interface between the ETL and CQDs or the HTL and CQDS along with the CQD matrix. Recently, cysteamine – (CTA) was used as an interface mediation method to passivate contact defects and modulate the cross-sectional potential distribution (Fig. 13A). QLEDs developed with CTA modulating interfaces led to a record external quantum efficiency (EQE) of 15.8% and a power conversion efficiency (PCE) of 12.7% at 1046 nm.¹¹¹ Santanu Pradhan *et al.* achieved a recorded external quantum efficiency (EQE) of 18.6% by employing a binary CQD matrix with optimized bandgaps and enhancing optical out-coupling with a hemispherical lens. Their approach involved a modified technique using two matrix CQDs with slightly different bandgaps to form a heterojunction, improving overall device performance and enabling applications in SWIR free-space optical transmission.¹¹²

Another emerging trend of CQDs in LED applications is to produce white light-emitting diodes (WLED). Two common approaches to producing white light from CQDs stem from

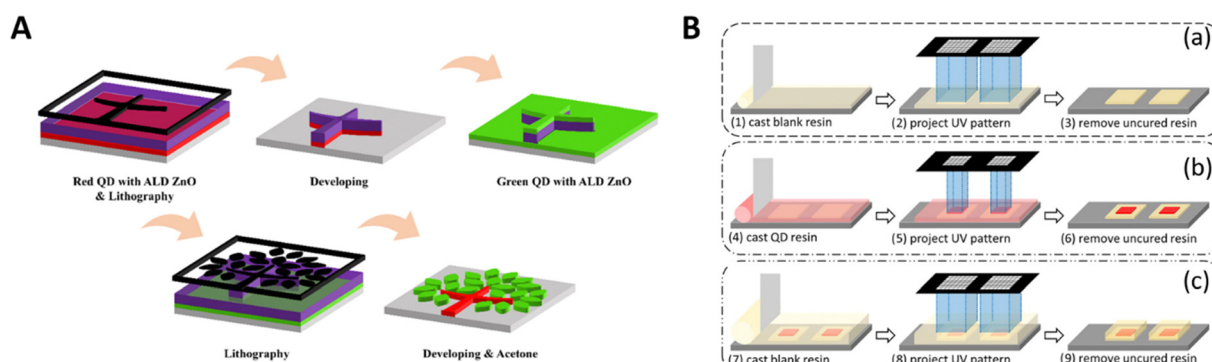


Fig. 12 (A) The multicolor (red and green, respectively) CQD film patterning process on CQDs with atomic layer deposition (ALD) ZnO surface passivation with repeated steps of photolithography processes. ALD treatment of ZnO toward CQD films improves the solvent resistance during the photolithography process. (B) Illustration of the CQD pocket fabrication process with the successive formations of the base layer (a), the core layer (b), and the top layer (c) [in figure QD means CQD]. Reproduced with permission from ref. 109. Copyright 2023 American Chemical Society. Reproduced with permission from ref. 110. Copyright 2023 American Chemical Society.

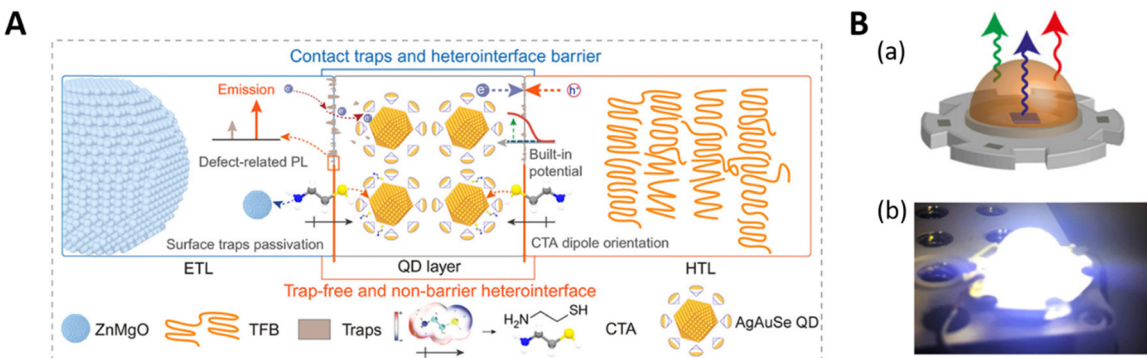


Fig. 13 (A) Schematic cross-sectional diagram of NIR-QLEDs based on CQD film contact interface mediation. In the ETL/CQD/HTL heterostructure, the amine groups of the CTA molecules passivated the ETL surface defects, and thiol groups coordinated with the CQD film surface. Inset: The electrostatic potential surface and molecular structure and dipole orientation of CTA. (B) White light generation as a combination of the blue electroluminescence from the LED and green and red emission from the CQDs (a), and a photograph of WLED using CQD liquids when it was turned on (b). Reproduced with permission from ref. 111. Copyright 2023 American Chemical Society. Reproduced with permission from ref. 113. Copyright 2022 American Chemical Society.

either mixing a set of quantum dot films of different emission colours,¹¹⁴ or by the specific synthesis of nanocrystals with a wide luminescence band.¹¹⁵ To achieve a broad luminescence peak, purpose trap-related emission can be stimulated *via* surface passivation¹¹⁶ or modification¹¹⁷ or nanocrystals can be doped with specific ions such as Cu⁺ and Mn²⁺.¹¹⁸ Another emerging technique utilizes the integration of CQDs on different color LED chips. Green- and red-emitting ZnCdSe/ZnSe CQDs were integrated into blue LEDs *via* liquid injection, resulting in red-green-blue (RGB)- and green-blue (GB)-based white LEDs (Fig. 13B) with luminous efficiencies of 129.6 and 170.4 lm W⁻¹, respectively.¹¹³

(II) *Solar cells*. One of the most advanced applications of CQDs is the conversion of solar energy to electrical power. Colloidal CQDs combine low cost and relatively high efficiency, making them perfectly suited to the needs of third-generation photovoltaics. Solution-processed photovoltaics, which rely on colloidal CQDs, can significantly reduce production costs by using roll-to-roll or spray-coating fabrication technologies as well as low-temperature synthesis processes.^{119,120} The exponential increase in power conversion efficiency (PCE) of colloidal quantum dot (CQD) solar cells over the past ten years, along with advancements in manufacturing techniques, suggests further colloidal CQD

applications in the renewable energy area. Since the first hybrid CQD¹²¹ and entirely inorganic CQD¹²² solar cells were fabricated, the efficiencies of these devices have enhanced drastically and consistently attracted significant attention, with constantly evolving designs. To enhance the efficiencies, optimization of the cathode material, with Al,¹²³ Ag,^{124,125} and Mg¹²⁶ etc. tested as low-work function metals, while organic¹²⁷ and inorganic¹²⁸ intermediate layers were examined. Many efforts have been made as summarized in Table 2 to improve the morphology of the TiO₂/CQD interface,¹²⁹ ZnO/CQD interface,^{130,131} CQDs/organic HTL interface¹³² and the photoanodes^{133–135} in general. Bin Jin *et al.* introduced a novel voltage-assisted successive ionic layer adsorption and reaction (VASILAR) technique (Fig. 14A) to modify the TiO₂/CQD interface. With their method which employed an electric field for uniform CQD distribution on TiO₂ mesoporous films, they achieved an outstanding performance with an efficiency of 5.7% for quantum dot-sensitized solar cells (CQDSSCs).¹²⁹ In another amazing work, Jihyung Lee *et al.* aimed to enhance charge extraction at the ZnO/CQD interfaces. They introduced a cinnamic acid ligand-based interfacial layer for the ZnO electron transport layer (ETL) with a cascading band offset, which effectively reduced potential barriers and minimized charge accumulation and bimolecular recombination at the interfaces (Fig. 14B).¹³⁰ On the other hand, Sandeep

Table 2 Performance summary of CQD-based solar cells

Materials	Methods to improve the performance of solar cells	Power-conversion efficiency (%)	Ref.
CdS/CdSe CQDs	Improvement of TiO ₂ /CQD interface using a VASILAR technique	5.7	129
PbS CQDs	Enhancement of charge extraction at the ZnO/CQD interfaces	14.01	130
PbS CQDs	Interface engineering	2.94	131
PbS CQDs	Fabrication of CQD/mixed-organic junction	13.6	132
CdS/CdSe CQDs	Introduction of TiO ₂ nanofiber decorated with ZnO nanosheets	3.05	133
CdSe CQDs	<i>In situ</i> cation exchange process	11.6	136
PbS CQDs	<i>In situ</i> synergistic passivation (ISP) strategy	13.3	137
PbS CQDs	Regulation of thiol capping ligands	12.2	138
PbS CQDs	Solution annealing (SA) strategy	11	139
PbS CQDs	Introduction of a hybrid passivation strategy	12.70	140
PbS CQDs	Enhancing the quality of the ZnO ETL	13.54	141

Kumar *et al.* controlled the roughness of ZnO nanocrystals by varying the binary solvent volume ratio of chloroform and methanol (CF:MeOH) to optimize the performance of the solar cells.¹³¹ Yujin Jung *et al.* recently proved that thiol termination of the CQD surface led to a reduction in the interfacial barrier, resulting in a 4-fold increase in charge transfer efficiency. The CQD/mixed-organic heterojunction solar cells exhibited a remarkable photocurrent density of 33.3 mA cm^{-2} and near-unity broadband quantum efficiency up to 1100 nm. The integration of a mixed-organic layer and interface engineering using thiol ligands significantly enhanced optical properties and charge transport. Consequently, the hybrid solar cell achieved a notable power conversion efficiency of 13.6%.¹³² The development of novel nanoarray photoanodes is very promising. Yang Cao *et al.* developing vertically aligned TiO₂ nanofiber decorated by ZnO nanosheets. They demonstrated that such a hybrid array photoanode improved both short-circuit current density (J_{sc}) and open-circuit voltage (V_{oc}) as compared to pristine TiO₂ nanofiber films, resulting in improved solar cell conversion efficiency from 2.37% to 3.05%.¹³³

With time, the focus has been on the development of CQD synthesis strategies,¹⁴² ligand passivation,^{136–140} and the

creation of a hybrid ETL.¹⁴¹ Mohan Yuan *et al.* used PbI₂ as both a passivating ligand and a cation source, which induced the transformation of CdSe to PbSe (Fig. 14C) and improved the defect density and carrier lifetime of PbSe CQD films, leading to enhanced photovoltaic performance in PbSe solar cells.¹³⁶ Yang Liu *et al.* used an *in situ* synergistic passivation (ISP) strategy, introducing short functional molecules during CQD synthesis, to achieve dramatically enhanced passivation. This in turn significantly reduced surface trap density and avoided problematic ligand exchange passivating processes.¹³⁷ Then, Jingxuan Chen *et al.* focused on enhancing the performance of infrared colloidal quantum dot solar cells (CQDSCs) by addressing the detrimental effects of conventional 1,2-ethanedithiol (EDT) ligands on the underlayer n-type CQD solid films during the preparation of a p-type CQD solid film on top. Through a systematic exploration of various thiol ligands, they found that the molecular structure of the thiol ligand plays a crucial role in the interaction with CQDs. Specifically, 4-amino benzene thiol (ABT) emerged as an optimal ligand for p-type CQDs, effectively replacing EDT without compromising the integrity of the underlayer n-type CQD solid films.¹³⁸ Xinlu Liu *et al.*

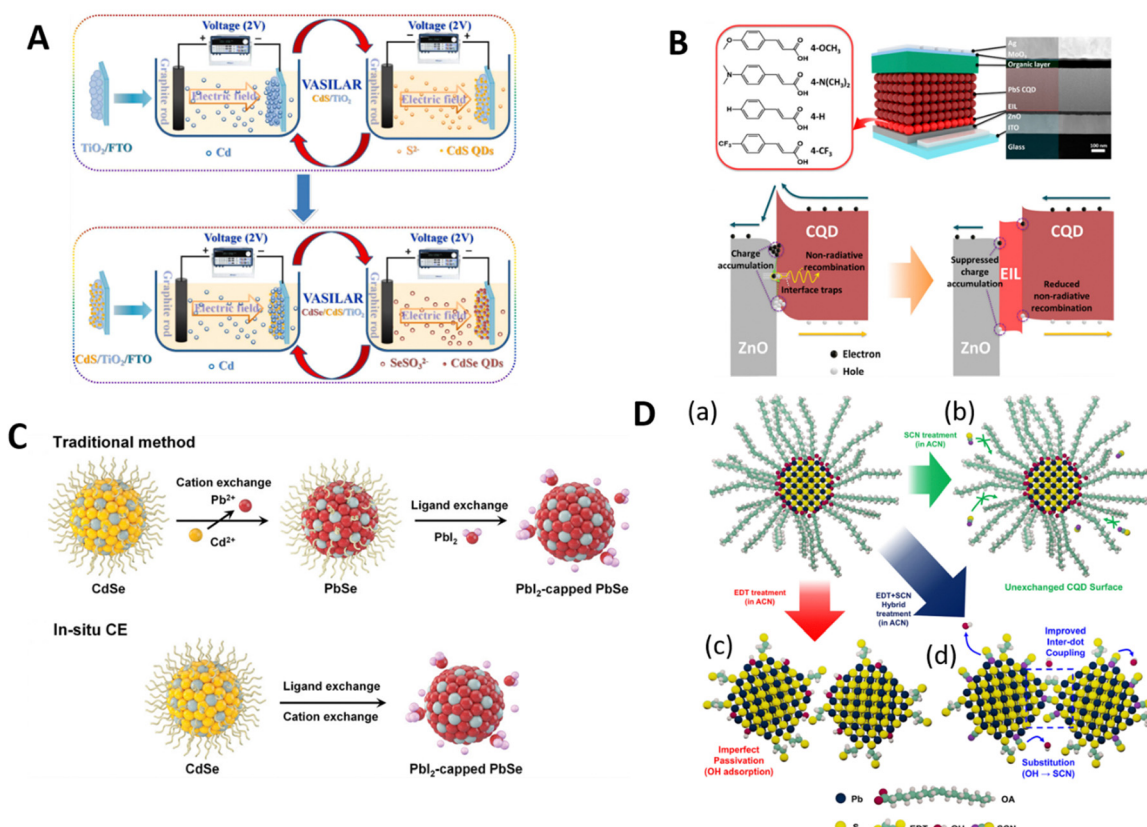


Fig. 14 (A) Schematic diagram of the VASILAR process for the construction of TiO₂/CdS/CdSe film. (B) Proposed interface engineering scheme: insertion of an EIL between ZnO and CQD layers in a CQD/organic hybrid solar cell to suppress charge accumulation. (C) Sketch of PbI₂-capped PbSe CQD synthesis using the traditional method (a), and their method (b). The utilization of PbI₂ as a precursor improved the defect density of PbSe films through the conversion of CdSe to PbSe. (D) Schematics describing the surface environment of CQDs: before ligand exchange (a), after SCN-only treatment (b), EDT-only treatment (c), and CQDs after EDT + SCN hybrid treatment (d). Reproduced with permission from ref. 129. Copyright 2023 Elsevier. Reproduced with permission from ref. 130. Copyright 2023 American Chemical Society. Reproduced with permission from ref. 140. Copyright 2020 American Chemical Society.

engineered the surface chemistry of PbS CQDs for enhanced photovoltaic performance through the ligand passivation process. They introduced a novel solution annealing (SA) strategy, involving thermal-assisted organic ligand desorption and simultaneous passivation of desorbed vacancies. The process was applied after the conventional ligand exchange, using concentrated lead halide ligands. The annealing effectively desorbed electrically insulating oleate ligands and trap-related surface groups, replacing them with more conductive lead halide ligands, resulting in a more complete ligand exchange.¹³⁹ Jonghee Yang *et al.* addressed imperfect surface passivation in colloidal quantum dot-based photovoltaics (CQDPVs) by introducing a hybrid passivation strategy, utilizing both 1,2-ethane dithiol (EDT) and thiocyanate (SCN). This hybrid passivation significantly ameliorated the surface passivation of CQD hole transport layers (HTL), effectively mitigating charge recombination. The mechanism involved successful dual passivation of the CQD surface by EDT and SCN. The hybrid treatment reduced inter-dot distance and minimized unbound thiolates which solely adding EDT or SCN could not achieve (Fig. 14D). This modification enhanced the charge transport environment in the CQD HTL. Consequently, the improved surface passivation and reduced inter-dot spacing facilitated efficient charge separation.¹⁴⁰ Shiwen Fang *et al.* explored a hybrid strategy to enhance the quality of ZnO ETL by incorporating stable organic open-shell donor–acceptor type diradicaloids. These diradical molecules, with high electron-donating properties, effectively passivated deep-level “trap states” and improved ZnO nanoparticle film conductivity. The passivated ZnO ETL was applied in PbS CQDs solar cells, resulting in a notable power conversion efficiency of 13.54%.¹⁴¹

(III) CQD-based photodetectors. The absence of widely utilized detectors for the near-infrared spectral area (NIR), such as Si-based avalanche photodiodes (APD) or CCD cameras used in the visible range, is the main driving force behind the substantial development of CQD-based photodetectors.¹⁴³ NIR photodetectors with great sensitivity, such PMTs, Ge or InGaAs APDs, and InGaAs-based arrays, are prohibitively expensive, which limits their widespread use. According to this theory, soluble-processed CQDs might take the place of inorganic semiconductors that are now in use. A vast array of opportunities exist for the development of these CQD-based photodetectors thanks to bandgap tuning and surface chemistry.

NIR photo-detector. NIR spectrum detection is becoming more and more necessary, especially in the disciplines of food inspection, agriculture, biology, and spectroscopy, as well as in optical fibre communications, imaging, security, and remote sensing.¹⁴⁴ However, new industries like the military, autonomous vehicles, and healthcare have raised standards for NIR detector performance. On the one hand, this rising demand calls for a decrease in the cost of producing NIR photodetectors. The high cost of materials and accompanying technologies, such as photodetectors based on InGaAs and InGaAsP, prevents the widespread use of traditional commercial photodetectors based on III–V compound semiconductors. The monolithic integration

of III–V devices on silicon electronics is impeded by the fundamental characteristics of III–V semiconductor compounds, as well as issues related to lattice mismatch, high thermal budget, and cross-contamination.^{145,146} Though it is hoped III–V detectors will not become less complex or expensive to produce if they are integrated with amplification and readout circuitry.¹⁴⁷ The technology for CMOS-compatible Ge on Si photodetectors has advanced significantly, however the operational spectral range (Ge direct band gap) is still restricted to less than 1600 nm, and the manufacturing cost is still very high.^{148–150} Furthermore, the need for flexible NIR photodetectors has grown quickly due to the growing application of NIR photodetectors in contemporary medical and health domains, such as electronic skin. However, it is challenging to use conventional III–V semiconductors made using the epitaxial growth technique in flexible devices. The aforementioned rationales have led to extensive exploration of numerous novel materials in the realm of near-infrared photodetectors, with CQDs being of particular interest. Excitons are bound by semiconductor nanostructures called CQDs in three different spatial orientations. CQDs exhibit strong light-matter interactions and unusual optical features, the most significant of which are large adjustable band gaps and high absorption coefficients, due to their typical strong confinement.^{19,151–153} Meanwhile, two other significant advantages of CQDs are their numerous exciton production effects and their ease of manufacture as materials that can be processed in a solution.^{154,155} As a result, CQDs offer a great deal of potential for use as absorbers in inexpensive, tunable-spectrum NIR detectors. These CQDs are primarily PbS^{156–159} and PbSe.¹⁶⁰

In the 1940s, bulk PbS was used in IR detectors as a conventional 0.6 eV band gap semiconductor for IR responses.¹⁶¹ On the other hand, nanoscaled PbS CQDs show some unique characteristics, including a high molar broadband absorption coefficient ($106 \text{ M}^{-1} \text{ cm}^{-1}$) and large Bohr exciton radii (approximately 18 nm),¹⁶² and a wide range of tunable band gaps (0.6–1.6 eV).¹⁶³ They also have the benefits of being inexpensive, easily soluble, and having high air stability. PbS CQDs are therefore being utilized more and more in the field of infrared detection. PbS CQD-based photodetectors have rapidly progressed since G. Konstantatos *et al.* announced the first PbS CQD-based photodetector in 2005.¹⁶⁴ Their primary performance metrics, like response speed, dark current, on/off ratio, detectivity D^* , and responsivity R , can not only match but significantly exceed those of conventional III–V semiconductor photodetectors in some areas. More significantly, they demonstrate potential in areas not achievable with conventional semiconductor photodetectors, such as selective optoelectronic detection, NIR long-wave detection, and flexible electronic systems. The procedures for preparing and depositing PbS CQDs have advanced quickly during the last few decades. The advancement of ligand exchange technology allowed for the optimization of PbS CQD stability by adjusting the work function, carrier mobility, and carrier concentration.^{165,166}

Nevertheless, occasionally CdSe,^{167,168} CdTe,¹⁶⁹ and HgTe¹⁷⁰ CQDs are also employed as an absorbing material for NIR photodetectors. Metal chalcogenide CQD-based photodetectors with exceptionally high operating characteristics can be

fabricated *via* recent developments in CQD synthesis,¹⁷⁰ air stability improvement,¹⁷¹ new surface treatment concepts,¹⁷² coupling with plasmonic nanostructure¹⁷³ and elimination of interface defects between ETL and CQDs.¹⁷⁴ They work well in many kinds of photodetector configurations, including photo-transistors, photodiodes, and photoconductors, and they often have extremely high gain and sensitivity or quick photo-response times. For instance, PbSe CQD-based photodetectors may be sensitive in an extremely wide spectral range from 400 nm to 1800 nm,¹⁶⁰ having detectivity of up to 1.53×10^{13} Jones¹⁵⁶ with a high sensitivity of 45.3 A W^{-1} ¹⁵⁷ and an external efficiency of 1260%.¹⁵⁸

MIR photo-detector. In recent years, mid-infrared (MIR) photodetectors are often built using narrow-bandgap semiconductors produced on a suitable substrate by molecular beam epitaxy or chemical vapor deposition. The extensive use of MIR photodetectors is limited by these expensive and complex technical procedures. Solution-based colloidal technologies offer competitive operating qualities and a notable decrease in production expenditures. When applied to the spectral range above 2000 nm, PbS and PbSe CQDs, which are frequently used for NIR photodetectors, become inefficient. Few devices based on high-quality mono-dispersed lead chalcogenide CQDs functioning over 2000 nm have been reported, mostly because of the difficulty in synthesizing CQDs with a large diameter.^{175–177}

A range of Hg-based compounds have been suggested as superior PbS and PbSe CQD replacements in MIR detection. Menglu Chen *et al.* reported HgTe colloidal CQD-based photoconductors (Fig. 15) with detectivity as high as 5.4×10^{10} Jones at 80 K and 500 Hz.¹⁷⁸ The drop-casting method used by John C. Peterson *et al.* to make the MIR photodetector was found to be stable under ambient air and to exhibit good detectivities even at room temperature. They demonstrated that room-temperature quantum efficiencies of 10% and 15% could be attained for HgTe CQD devices by shrinking the device size to 50 by 50 μm .¹⁷⁹

A higher detectivity and faster time response was achieved when bismuth sulfide (Bi_2S_3) films were introduced as the electron transport layer (ETL) in HgTe CQD photodiodes, which facilitated uniform absorber deposition, enhanced charge extraction, and minimized interfacial losses.¹⁸⁰ Another opportunity to detect MIR radiation by CQDs is to utilize intraband

transitions. In the past, this idea was explored for 2D nanostructures, and many MIR photodetectors have been developed.^{181,182} However, there has not been much research done on intraband transitions in 0D nanostructures up to this point. Recently, photoconductivity in HgSe dots, resonantly generated at the $1\text{S}_e-1\text{P}_e$ wavelength (Fig. 16), was reported by Menglu Chen *et al.*¹⁸³ Additionally, an n-doped PbS CQD-based photodetector for the 5–9 μm range was presented by Íñigo Ramiro *et al.*, and it was demonstrated to have extremely high charge mobility.¹⁷⁶ Haozhi Zhang *et al.* have also developed an n-doped HgTe CQD photodetector which exhibits a $1\text{S}_e-1\text{P}_e$ intraband transition in the long-wave infrared (LWIR) range (8–12 μm). They observed a blueshift of 90 cm^{-1} in the intraband transition from 300 to 80 K, while the interband transition redshifted by 350 cm^{-1} .¹⁸⁴ Further advancements in MIR detectors based on intraband transitions in colloidal CQDs could be possible with precise control over CQD doping and surface chemistry.

UV photo-detector. From the edge of the visible zone to the high-energy portion of the X-ray spectrum, corresponds to UV light (10–400 nm). When UV light (320–400 nm) from the sun strikes the Earth's surface, it can cause skin damage and even cancer.¹⁸⁵ Moreover, UV photodetectors are widely used in fire alarms, cancer cell identification, and missile early warning tracking because, in contrast to visible and infrared light, UV signals do not interact with their surroundings.^{185,186} One of the most promising materials for UV photodetectors has been zinc oxide (ZnO), which is easily synthesized, less harmful to the environment, and has a direct bandgap of around 3.3 eV. Early in the 20th century, ZnO -photodetectors were first studied. This was followed by a number of studies to resolve the problem that the Schottky structure ZnO photodetectors lacked significant device performance and inexpensive manufacturing techniques.^{186,187} Other compounds that can be employed include SnO_2 , NbO_5 , MgO , and ZnS . Although ZnO colloidal CQDs constitute a new generation of UV photodetectors, bulk 2D and 1D ZnO -based devices have been employed for UV detection in the past.¹⁸⁸ In combination with ZnO CQDs, several materials have been tested to determine the best-performing UV photodetectors. For example, the authors' device, which can detect signals as faint as 1.72 mW cm^{-2} , has a very high sensitivity due to increased carrier separation at the ZnO CQD/MXene nanoflake interface.¹⁸⁹ Norah Alwadai *et al.* fabricated an all-inorganic p–n heterojunction UV-C

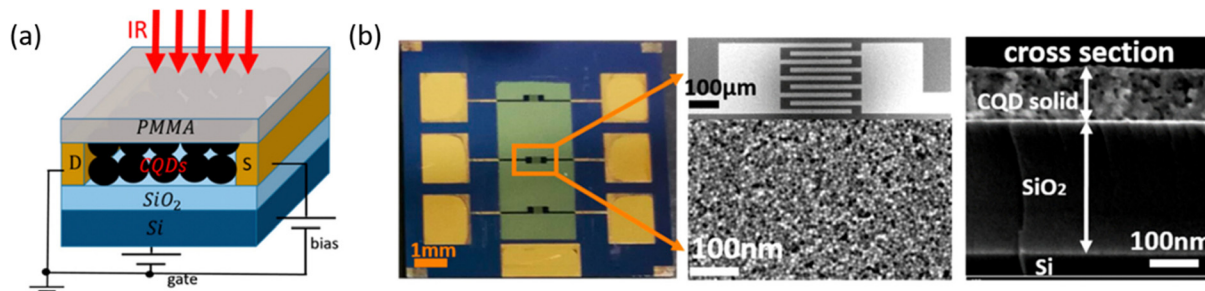


Fig. 15 Schematic of a bottom-gate field effect transistor (FET) made of CQDs (a), and a photograph and SEM image of three FET devices of $0.3 \text{ mm} \times 0.16 \text{ mm}$ (b). Reproduced with permission from ref. 178. Copyright 2019 American Chemical Society.

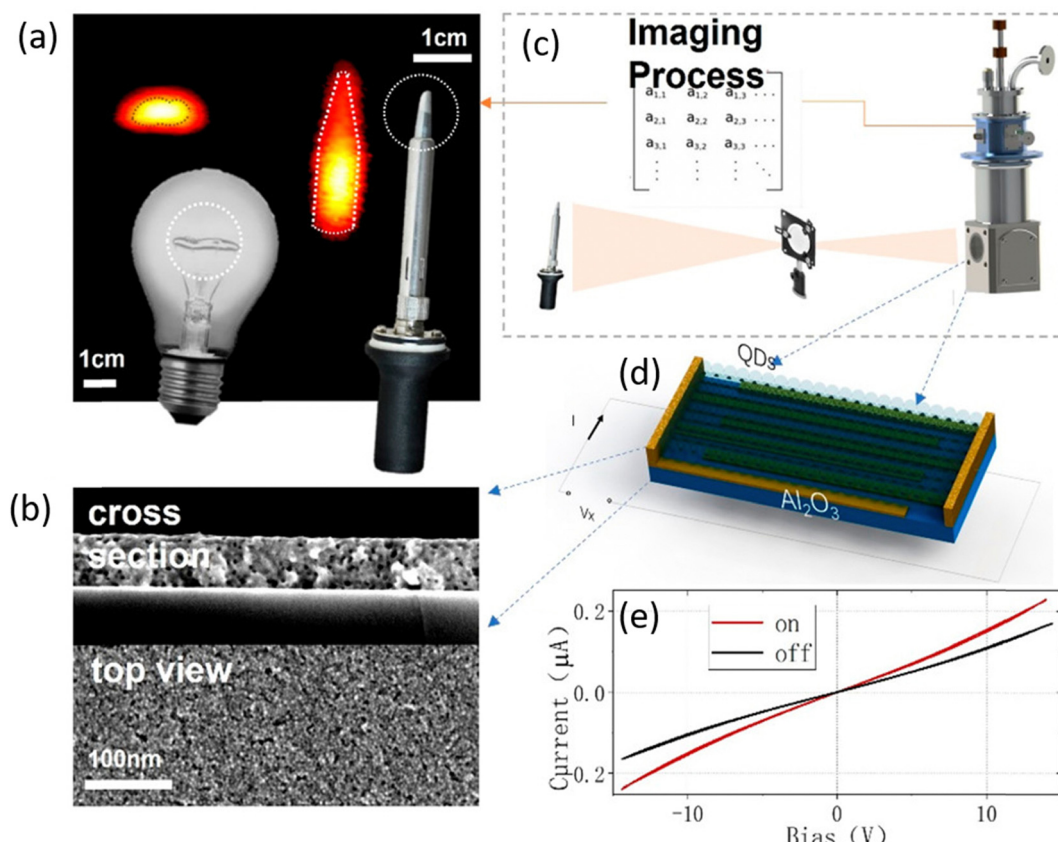


Fig. 16 Infrared hot images obtained using a HgSe intraband CQD photodetector (a), SEM top view and cross-section of a HgSe CQD photoconductor (b), schematic diagram of the scanning imaging method (c), schematic figure of the CQD photoconductor (d) and HgSe CQD photo-conductor current without (black line) and with (red line) blackbody radiation. The effective solid area is $\sim 0.3\text{ mm} \times 0.16\text{ mm}$ (e). Reproduced with permission from ref. 183. Copyright 2022 American Chemical Society.

detector using an n-type ZnO CQD layer and p-type CuO micro pyramids. This device demonstrated increased photo-responsivity under zero bias and a high gain due to interfacial trap-induced charge injection.¹⁹⁰ In another work, Shusen Lin *et al.* recently showed the outstanding performance of a ZnO CQD-based photodetector.¹⁹¹ They obtained an external quantum efficiency (EQE) of 813% at 0.34 mW mm^{-2} and a detectivity (D) of 7.251×10^{11} Jones on the Au core-shelled AuPd hybrid NPs by including a blended active layer of ZnO CQDs and molybdenum disulfide (MoS_2) nanoflakes. Shusen Lin *et al.* also fabricated a device with hybrid AuPt alloy nanoparticles and ZnO CQDs but also introduced a thin layer of graphene quantum dots (GQDs) showing that AuPt alloy nanoparticles provided an increase in the photocurrent, while the added carrier injection is achieved by the thin layer of GQDs.¹⁹² An overall performance summary of CQD-based photodetectors including UV, NIR, and MIR with the actual values of detectivity and responsivity is provided in Table 3.

(2) **Analytical sensing.** Over the past ten years, CQDs have made it easier to develop sensitive fluorescence sensors because of their special photophysical qualities, adaptable surface chemistry, capacity to bind ligands, and ability to be encapsulated in various materials or attached to various functional materials while maintaining their inherent luminescence.^{193,194} Due to their small size, CQDs have a higher concentration of surface

atoms.¹⁹⁵ Additionally, their surface contains broken chemical bonds, also known as dangling bonds,¹⁹⁶ which makes them perfect molecule receptors for sensing applications. As the exciton recombination of CQDs produces fluorescence, changes in surface charge or ligand components of the CQDs are expected to impact the efficiency of the core electron-hole recombination and, in turn, the luminescence efficiency. This is because changes in exciton recombination occur either before the charge carrier is trapped (band gap recombination) or while the charge carrier is trapped in very shallow traps (near band gap recombination).¹⁹⁷ Thus, fluorescence changes caused by the direct physical adsorption or chelating of ions and small molecules on the surface of the CQDs triggered by the exchanged ligand may be used to construct a chemical sensing system based on CQDs. As an analytical sensor, CQDs have been capitalized on for sensing drugs, antibiotics, different amino acids, peptides, and vitamins found in human serum, biogenic amines in food samples, heavy metal ions, poisonous pesticides, gas molecules, viruses, *etc.* However, these applications present many challenges in different sectors. Antibiotic and drug sensing requires the provision of sensors capable of detecting specific antibiotics or a particular drug with high sensitivity, while eliminating interfering substances in body fluids is of great importance for accurate detection.^{198,199} Vitamins, amino

Table 3 Performance summary of CQD-based photodetectors working within the UV region to MIR region

Materials	Methods to enhance the performance of PV cells	Working region	Detectivity (D^*) (Jones)	Responsivity R (A W $^{-1}$)	Ref.
PbS CQDs	Heterojunction improvement	NIR	1.53×10^{13}	19.070	156
PbS CQDs	Solution phase ligand exchange	NIR	9.3×10^{12}	45.3	157
PbS CQDs	Tailoring the trap density of CQDs by designing surface ligands with dual functionality	NIR	2.6×10^{12}	—	158
PbS CQD	Incorporation of 2D materials	NIR	1.6×10^{11}	Up-to 46	159
PbSe CQDs	Hybrid nanostructure fabrication strategy	NIR	—	1.8	160
CdSe/ZnS CQDs	Plasmon coupling	NIR	—	—	167
CdSe/ZnS CQDs	Controllable layer-by-layer (LbL) deposition	NIR	—	0.146	168
CdTe CQDs	Introduction of a hole-blocking layer	NIR	1.1×10^{11}	0.5	169
HgTe CQDs	Ligand-engineered approach	NIR	3.9×10^{11}	0.38	170
PbS CQDs	Suppression of ion migration	NIR	—	—	171
InAs CQDs	New surface treatment concepts	NIR	1.9×10^{11}	—	172
PbS CQDs	Plasmon coupling	NIR	Order of 10^{13}	Always > 9	173
PbS CQDs	Elimination of interface defects between the ETL and CQDs	NIR	2.15×10^{12}	0.526	174
PbSe/PbS CQDs	Combination of a metamaterial perfect absorber	MIR	$\sim 1 \times 10^8$	~375	175
PbS CQDs	Doping of heavy metals	MIR	4×10^4 (at 6.8 μm) 8×10^4 (at 7.3 μm) 4×10^4 (at 8 μm)	1.5×10^{-4} (at 6.8 μm) 1.1×10^{-4} (at 7.3 μm) 1.3×10^{-4} (at 8 μm)	176
PbSe CQDs	Trap engineering of nanostructures by varying starting material counter ions	MIR	—	49 when Pb(OAc) $_2$ starting material	177
HgTe CQDs	Solid-state ligand exchange	MIR	5.4×10^{10}	—	178
HgTe CQDs	Minimization of the electrodes' series resistance	MIR	$> 10^9$	—	179
HgTe CQDs	Electron transport layer incorporation	MIR	$\sim 10^{11}$	0.35	180
PbS CQDs	2D nanostructure addition	MIR	4.11×10^{11}	—	181
Cu-In-Se CQDs	2D nanostructure addition	MIR	2.10×10^{12}	—	182
HgSe CQDs	Mixed-phase ligand exchange approach	MIR	$> 1.7 \times 10^9$	—	183
HgTe CQDs	—	MIR	$\sim 10^7$	—	184
ZnO CQDs	Self-assembled	UV	—	504	188
ZnO CQDs	Hybridization through 2D nanostructures	UV	26.66×10^{11}	0.373	189
ZnO CQDs	Spray-coating solution-processed method	UV	$\sim 1.72 \times 10^{11}$	0.956	190
ZnO CQDs	Coupling with 2D nanostructures and hybrid metal nanoparticles	UV	7.251×10^{11}	2.525	191
ZnO CQDs	Bimetallic nanoparticle incorporation	UV	7.04×10^{10}	2.299	192

acids, and peptides pose challenges due to their structural diversity and low molecular weight, which require the development of visual sensors. Food spoilage indicators require sensors capable of detecting biogenic amines, at trace levels with high selectivity, which are essential for ensuring food safety.²⁰⁰ Detection of toxic pesticides and hazardous substances in the environment around samples requires sensors with high sensitivity, the removal of interference from matrix components, and an assurance of long-term stability.²⁰¹ Environmental monitoring of heavy metals requires high sensitivity and selectivity, especially in samples with low metal concentrations, and robust sensors with long-term monitoring capabilities are needed.²⁰² CQDs, with their tunable bandgap power and adaptable surface chemistry, provide a promising solution. Surface modification of CQDs with unique ligands, substrate or receptors can enhance their selectivity toward target antibiotics or drugs or toxic pesticides and hazardous substances or heavy metal atoms enabling specific binding to these molecules with a change in fluorescence intensity or color, enhancing selectivity and sensitivity in detecting them visually. Gas sensing environmental and industrial applications require small-scale sensors with real-time capability to track a wide range of gases. CQD-based sensors, integrated into microfluidic or lab-on-a-chip devices, offer compact and portable solutions for gas sensing, leveraging their high surface area and customizable surface chemistry for selective gas detection. Finally, the development of sensitive viruses for the

rapid detection and control of emerging pathogens presents a challenge in detecting microorganisms at low concentrations in complex biological samples with high sensitivity and selectivity. From Table 4 it can be understood that functionalized CQDs, using advanced detection techniques such as fluorescence-resonance energy transfer (FRET) or surface-enhanced Raman spectroscopy (SERS) together, can enable rapid and simplified bacterial detection, facilitating rapid bacterial identification and containment efforts.²⁰³

(I) *Drug and antibiotic sensing.* A straightforward and uncomplicated ratiometric fluorescent probe made of blue emission carbon nanodots (CNDs) and yellow emission Zn-doped CdTe quantum dots (ZnCdTe CQDs) capped with GSH was fabricated by Tian Zhang *et al.* for 6-mercaptopurine (6-MP) sensing. The detection of 6-MP using this probe can be achieved by checking the fluorescence profile of the probe. The fluorescence intensity of ZnCdTe CQDs is selectively quenched by 6-MP through fluorescence resonance energy transfer (FRET) (Fig. 17A). The fluorescence intensity ratio (F445/F565) demonstrated a linear response to the concentration of 6-MP, while the fluorescence intensity of CNDs essentially remained constant over this period (Fig. 17B). The ZnCdTe CQD/CND developed probe showed a broad and similar detection range of 1.0 to 100.0 $\mu\text{mol L}^{-1}$ with a detection limit of 0.46 $\mu\text{mol L}^{-1}$.²⁰⁴ A highly sensitive fluorescence nanoprobe was designed for the

Table 4 Summary of CQD-based nano-platforms for analytical sensing applications

Materials	Analyte	Detection methods	Detection limit	Detection range	Ref.
ZnCdTe CQDs	6-MP	Decline in the emission intensity of CQDs	0.46 $\mu\text{mol L}^{-1}$	1.0 to 100.0 $\mu\text{mol L}^{-1}$	204
ZnSe/In ₂ S ₃ CQDs	Cocaine	Increase in CQD emission intensity	0.8 nM	—	205
CdTe CQDs	MA	Quenching of CQD emission	40.34 ± 1.05 pM	0.134–124 nM	206
CdTe/ZnS CQDs	MA	Quenching of CQD emission	4.15 ± 1.08 pM	13.8 pM–999.8 nM	207
CuInS ₂ /ZnS CQDs	CTC	Recovery of CND's emission	0.36 μM to 0.46 μM	0–50 μM	208
Ag ₂ S CQDs	AA	Restoration of CQD emission	0.014 μM	0.2 μM –20 mM	209
CdTe/CdSe/ZnS CQDs	AA	Decline in the emission intensity of CQDs	0.014 μM	0–27 μM	210
CuInS ₂ /ZnS CQDs	Asp	Quenching of CQD emission	78 nM	830 nM–0.33 mM	211
Ag ₂ S CQDs	GSH	Restoration of CQD emission	60 μM	—	212
CdTe CQDs	BAs	Increase in CQD emission intensity	—	1.259–5.428 μM	213
Cds CQDs	Paraquat, DDVP, -ammonium	Emission intensity change and spectral shift of fluorescence	1.44 μM (paraquat), 0.23 mM (DDVP), 49.8 μM (glufosinate-ammonium)	—	214
CdTe CQDs	Chlorpyrifos	Enhanced rate of electron transport	0.16 pM	0.5 pM–500 nM	215
CdSe/ZnS CQDs	4-AP, 4-NP	Increase in current amplitude	34.8 nM (4-AP), 17.7 nM (4-NP)	—	216
— (CQDs)	Cu ²⁺	Decline in the emission intensity of CQDs	500 pM	—	217
ZnS–Mn ²⁺ CQDs	Cu ²⁺	Quenching of CQD emission	23 nM	0–4 μM	218
CuInS ₂ /ZnS CQDs	Cu ²⁺	Quenching of CQD emission	63 nM	75–750 nM	219
Cds CQDs	Cu ²⁺	Solution color change	—	—	220
CdSe CQDs	Hg ²⁺	Obscuring of fluorescence	5 ppm	5–50 ppm	221
CdSe/ZnS CQDs	Hg ²⁺	Quenching of CQD emission	74.8 nM and 54.8 nM	—	222
CuInS/ZnS CQDs	Pb ²⁺	Quenching of CQD emission	4.48 ppb	5–50 ppb	223
ZnSeS/Cu:ZnS/ZnS CQDs	Pb ²⁺	Quenching of CQD emission	21 nM	0.04–6 μM	224
CdZnTe CQDs	Pb ²⁺ and Hg ²⁺	Increase in CQD emission intensity	—	—	225
CdTe CQDs	Fe ²⁺ , H ₂ O ₂ and •OH	Quenching of CQD emission	58 nM (H ₂ O ₂), 8 nM (•OH)	—	226
PbS CQDs	NO ₂	—	0.78 ppb	—	227
PbS CQDs	Methanol	Series of interactions and changes on the surface of thin films	—	10–100 ppm	228
CdTe/ZnS CQDs	Covid-19 viral genome RNA	Drop in fluorescence intensity	0.000823 μM	—	229
CdTe/ZnS CQDs	SARS-CoV-2	Shift in fluorescence intensity	2.19 × 10 ⁻⁹ μM	—	230
Cds CQDs	ctDNA	Variations in ECL	3.4 aM	—	231

detection of cocaine. This fluorescence probe is composed of amphiphilic polymer (A-polym)-functionalized cadmium-free ZnSe/In₂S₃ core/shell CQDs, cationic cetyltrimethylammonium bromide (CTAB)-capped gold nanoparticle (AuNP) and a DNA Aptm receptor. Initially, the nanoprobe does not show any fluorescence as the fluorescence emission of the A-polymer-coated CQDs is quenched by CTAB-AuNP. But, upon the interaction of cocaine with the nanoprobe, the localized surface plasmon resonance (LSPR) signal from AuNP amplified the fluorescence intensity signal of the CQDs thereby turning on the fluorescence of the bound CQDs. This nanoprobe can selectively and quantitatively detect cocaine with a detection limit of 0.8 nM.²⁰⁵ In a different work, Hamideh Elmizadeh *et al.* developed a brand-new apta-nano biosensor based on CdTe CQDs for quick and accurate detection of MA in biological fluids and biological forensic evidence. Using the ligand-exchange technique, the water-soluble APTA-nano biosensor was created by substituting thiolated MA aptamer for thioglycolic acid (TGA) molecules on the surface of CQDs. Following aptamer modification, the fluorescence intensity of CQDs increased; however, the addition of the target molecule (MA) resulted in a reduction in fluorescence intensity because of the formation of the aptamer-MA complex. They found that the detection limit of their nanosensor for MA is 40.34 ± 1.05 pM.²⁰⁶

A similar group developed another sensor based on CdTe/ZnS CQDs. They used two processes to manufacture the sensor. The first stage was using the ligand exchange approach to replace the glutathione (GSH) and thioglycolic acid (TGA) molecules on the surface of CQDs with thiolated MA aptamer, increasing the fluorescence intensity of the CQDs. The ideal concentration of DNA-conjugated Cy3 fluorophore was progressively added to the mixture in the second stage. The energy transfer from CQDs to Cy3 fluorophore causes the quenching of CQDs and activation of the fluorophore, according to the fluorescence resonance energy transfer (FRET) process. Ultimately, the thiolated labeled aptamer tends to bind to the target (MA) while varying the concentration of MA in this system. In consequence, Cy3 fluorophore detached from the CQD surface, contributing to the quenching of the CQDs and fluorophore. The detection limit of MA is 4.15 ± 1.08 pM.²⁰⁷ A ratiometric fluorescence sensor was created by Xiaoping Chen *et al.* to detect the antibiotic chlorotetracycline (CTC) with selectivity. The sensor is made up of carboxyl-modified CuInS₂/ZnS CQDs with dark-red emission and blue emissive carbon nanodots (CNDs) where CuInS₂/ZnS CQDs act as quenching agents to reduce the fluorescence of CNDs *via* the FRET mechanism. Following the addition of CTC, the interaction between CNDs and CuInS₂/ZnS QDs is inhibited, which causes CNDs' fluorescence to recover while that of the CQDs is

unaffected. The detection limit of CTC lies in the range of 0.36 μM to 0.46 μM .²⁰⁸

(II) *Vitamin, amino acid, and peptide sensing.* To sense ascorbic acid (AA) in serum and juice, Haoyu Chen *et al.* engineered a ratiometric fluorescent nano platform using Ag_2S CQDs and multifunctional hydroxyl cobalt oxide nanoflakes (CoOOH NFs). They assembled Ag_2S CQDs on the surface of CoOOH NFs to create this hybrid sensor. This resulted in an inner filter effect (IFE) that caused the NIR fluorescence emission of the Ag_2S CQDs to quench at 680 nm. Next, they included *o*-phenylenediamine (OPD), a frequently used substrate of oxidase-like (OXD) mimic, into the system. CoOOH NFs possessing OXD-like activity can catalyze the conversion of the non-fluorescent substrate of OPD into the fluorescent substrate 2,3-diaminophenazine (DAP), resulting in the emergence of maximum fluorescence at 575 nm. The introduction of AA resulted in a decrease in the fluorescence emission of DAP, as the transformation of Co^{2+} led to a reduction in the OXD-like activity of CoOOH NFs. Ag_2S CQDs were released concurrently, which led to the restoration of red fluorescence. The detection procedure may be made simpler if the same wavelength was used to activate both of these fluorescent signals. The linear range and detection limit of 0.2 μM –20 mM and 0.014 μM , respectively, may be used to quantify AA using the readout

F575/F680.²⁰⁹ Another experiment was carried out by Jin Wang *et al.* to sense ascorbic acid (AA) in solution. They used water-soluble CQDs with various core–shell configurations as fluorescence probes (FPs) and the photoluminescence (PL) intensity of CQDs as a detection indication for AA due to their unique sensitivity. They regulated the concentration of FPs and core–shell type to achieve multiscale regulation of the measurement range and sensitivity of AA. They noticed that when AA was added, the photoluminescence intensity of the CQDs decreased because AA promotes the non-radiative recombination of charge carriers. Nevertheless, they set up a capillary sensor with an inner wall honeycomb CQD film connected, which significantly expanded the CQDs and AA's surface area, shortened the measurement time, and improved sensitivity. The achieved minimum detection limit for AA was 0.014 μM .²¹⁰ Sara Safari, recently used $\text{CuInS}_2/\text{ZnS}$ core/shell CQDs for aspartic acid (Asp) detection which is a non-essential amino acid for the human body and is responsible for the Krebs or citric acid cycle. Compared to the other amino acids, the probe's fluorescence response toward Asp was very strong. The addition of Asp to an aqueous medium caused a considerable quench in the fluorescence intensity. This probe's lower limit of detection was determined to be 78 nM.²¹¹ The application of CQDs as a sensor is not limited to amino acids but also extends to peptides like GSH present in human serum.

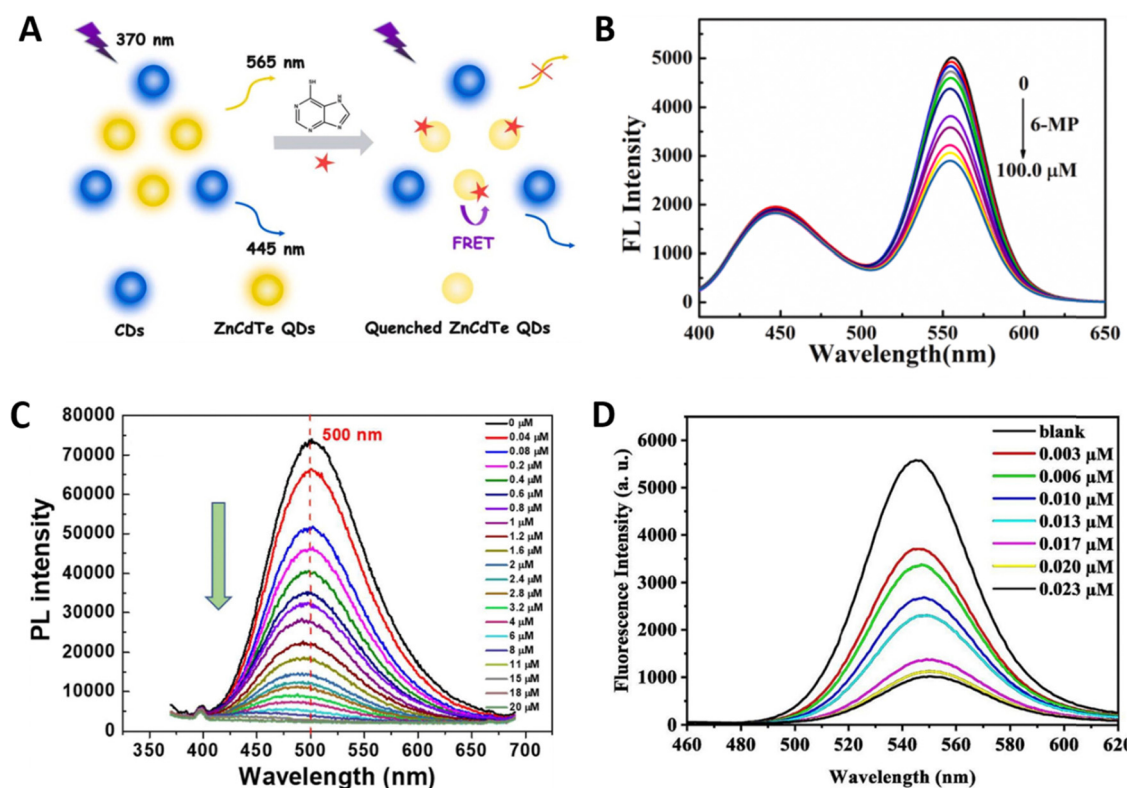


Fig. 17 (A) Schematic illustration of ratiometric fluorescence sensing of 6-MP. (B) Ratiometric fluorescence spectra of different concentrations of 6-MP from 1.0 to 100.0 $\mu\text{mol L}^{-1}$. The fluorescence peak of CQDs gets quenched upon the addition of 6-MP while the CND emission remains fixed. (C) PL emission spectra of $\text{ZnSeS}/\text{Cu:ZnS}/\text{ZnS}$ CQDs dispersed in water upon the addition of various concentrations of Pb^{2+} . (D) Fluorescence emission spectra of a nano biosensor with different micromolar concentrations of ctDNA (0–0.023 μM) in RNase-free water; the emission spectra shift to longer wavelength with an increase in SARS-CoV-2 concentration. Reproduced with permission from ref. 204. Copyright 2022 Elsevier. Reproduced with permission from ref. 224. Copyright 2022 Elsevier. Reproduced with permission from ref. 230. Copyright 2023 Elsevier.

Yun Shu *et al.* constructed a new fluorescent sensing platform that is intended for the quick and accurate measurement of glutathione (GSH). The device uses NIR fluorescent Ag₂S CQDs and MnO₂ 2D nanosheets as NIR emitters and quenchers. By adhering these Ag₂S CQDs to the surface of MnO₂ nanosheets, they were able to build this nano platform. GSH may convert MnO₂ to Mn²⁺, which would break the nano platform and subsequently cause the NIR fluorescence of Ag₂S CQDs to return. This would allow this nanoplatform to function as a GSH sensor with a 60 μM limit of detection.²¹²

(III) *Biogenic amine sensing.* Moreover, to build up a straightforward, quick, and efficient food safety monitoring system, Jianfeng Yan *et al.* established a dual emissive fluorescent sensor based on blue emissive CNDs and yellow emissive CdTe CQDs for visual detection of biogenic amines (BAs) in food samples. Blue-emitting CNDs served as internal references in this sensor, whereas CdTe CQDs functioned as indication signals. The medium's basicity steadily went up with the addition of BAs, which enhanced the yellow fluorescence of the CdTe CQDs. The designed ratiometric fluorescence sensor achieved low detection limits (1.259–5.428 μM) and quick responses (30 s) for the quantitative investigation of eight different types of BAs.²¹³

(IV) *Toxic pesticide and hazardous compound sensing.* For the detection of organic and inorganic pesticides and hazardous compounds, Siyu Chen *et al.* synthesized water-soluble 3-mercaptopropionic acid (MPA) capped CdS fluorescent CQDs to simultaneously detect three different pesticides, dichlorvos (DDVP), paraquat, and glufosinate-ammonium, through different fluorescence responses. The fluorescence of CQDs can be efficiently quenched using paraquat, while DDVP can significantly increase fluorescence. Both a 30-fold fluorescence amplification and a 150 nm fluorescent blueshifting may be induced by glutamate-ammonium. For all three pesticides, the probe showed low detection limits: 1.44 μM for paraquat, 0.23 mM for DDVP, and 49.8 μM for glufosinate-ammonium.²¹⁴ For chlorpyrifos pesticide detection, a biosensor was developed by Hosna Ehzari *et al.* This biosensor used a single frequency impedance (SFI) approach and included human serum albumin (HSA), TGA-capped Pd-doped CdTe quantum dots (Pd:CdTe CQDs), and sub-layer multiwall carbon nanotubes (MWCNT). The resistance at the electrode surface increased when the CPS-HSA complex formed in the nano-matrix. The outcomes showed that Pd:CdTe capped with TGA enhanced the rate of electron transport and provided a perfect environment for blocking HSA. The LOD was determined to be 0.16 pM, and the suggested sensor demonstrated the ability to detect a broad range of CPS values from 0.5 pM to 500 nM.²¹⁵ The presence of derivatives of phenol in the environment can lead to significant imbalances in the ecological balance. Thus, it is essential to detect such dangerous toxic compounds.²³² Kuo-Yuan Hwa *et al.* fabricated an electrochemical sensor with CdSe/ZnS CQDs anchored on functionalized multi-walled carbon nanotubes (f-MWCNTs) for the simultaneous detection of 4-aminophenol (4-AP) and 4-nitrophenol (4-NP). The goal of

functionalizing f-MWCNTs with CdSe/ZnS CQDs was to increase the electrode's surface area for excellent analyte molecule selectivity. Selective detection of these chemicals was made possible by the increase in current amplitude that occurred following the addition of 4-AP and 4-NP. Low detection limit values of 34.8 and 17.7 nM were demonstrated by the sensor for the detection of 4-AP and 4-NP, respectively.²¹⁶

(V) *Heavy metal sensing.* There are multiple strategies reported to sense heavy metal ions such as mercury ion (Hg²⁺), lead (Pb²⁺), copper (Cu²⁺), etc. For instance, Yao Li *et al.* developed a photothermal microreactor (PMR) system containing CQD nanoparticles to improve the detection of copper ions (Cu²⁺ ions) in a microliter sample. The device produced vortex fields and microbubbles with an improved photothermal effect by using photothermal waveguides (PTW). The development and aggregation of many water-in-oil microdroplets can be facilitated by microbubbles. Due to the vortex field's ability to trap CQDs as fluorescent probes, the huge surface area of microdroplets, and the acceleration of molecular motion due to elevated temperature, CQDs interact with copper ions (Cu²⁺) rapidly once they are gathered in the detecting region. The interaction of Cu²⁺ ions and CQDs results in a progressive decrease in relative fluorescence intensity at a constant lower power, highlighting Cu²⁺ ion selection. Under ideal circumstances, they succeeded in achieving 500 pM Cu²⁺ ion detection in 5 min with a 2 μL sample.²¹⁷ Another work by Subodhana Praballian Aswathy used fast fluorescence analysis and environmentally friendly ZnS–Mn²⁺ CQDs functionalized with (3-mercaptopropyl)trimethoxysilane (MPTS) to detect the heavy metal ion Cu²⁺. The effective transfer of electrons from the CQDs to the Cu²⁺ ions is the reason why the fluorescence of the CQDs was quenched when the system was exposed to the Cu²⁺ ions. Therefore, with an LOD of 23.0 nM, the reduction in the fluorescence signal functions as an accurate indication of the existence and concentration of Cu²⁺ ions.²¹⁸ Jose Varghese Rajendran *et al.* described the use of water-soluble glutathione (GSH) capped ternary CuInS₂/ZnS (CIS/ZnS) CQDs in a simple fluorometric approach for the detection of Cu²⁺ ions. The CQDs showed a considerable suppression of photoluminescence when subjected to Cu²⁺ ions compared to other metal ions in comparison to other metal ions such as Hg²⁺, Co²⁺, Cd²⁺, Pb²⁺, Zn²⁺, Ni²⁺, Mg²⁺, Sn²⁺, Mn²⁺, Fe²⁺, and Fe³⁺ ions. The quenching mechanism was attributed to the aggregation of CIS/ZnS CQDs resulting from the complexation of Cu²⁺ ions with the GSH capping group of the CQDs. At a concentration range of 75–750 nM, the fluorescence quenching of the CIS/ZnS CQDs showed a linear response to Cu²⁺ ions, with a LOD of 63 nM.²¹⁹ Furthermore, a smartly designed chitosan (CTS) modified CdS CQD (CdS@CTS CQD) system by Faisal K. Algethami *et al.* allowed for highly selective Cu²⁺ ion detection of heavy metals with the naked eye. As soon as the CdS@CTS CQD system interacted with Cu²⁺ ions, its color changed from yellow to grey-black. The process underlying the color shift, which is observable to the naked eye, has been linked to the complex formation between Cu²⁺ ions and CTS. When given other heavy metal ions, the

Published on 14 June 2024. Downloaded by University of Illinois Urbana-Champaign on 10/16/2024 10:50:58 PM.

system similarly changed color, but with less selectivity.²²⁰ For the sensing of mercury ions (Hg^{2+}) in solution Sohel Das *et al.* used 3-mercaptopropionic acid-capped CdSe (MPA-CdSe) CQDs. They found that MPA-CdSe CQDs had a sensitivity as low as 5 ppm for detecting Hg^{2+} in contaminated water. A significant obscuring of fluorescence was thought to be a sign of the selection of Hg^{2+} ion.²²¹ Two structures of CdSe/ZnS CQDs, with varying solubility characteristics, were synthesized by Gilma Granados-Oliveros *et al.* to detect Hg^{2+} ions. In the first structure, CdSe/ZnS CQDs were capped with oleic acid (CdSe/ZnS/OA). In the subsequent structure, glutathione was substituted for oleic acid by a ligand exchange process, yielding CdSe/ZnS CQDs capped with glutathione (CdSe/ZnS/GSH). As a result of glutathione replacing oleic acid in the CdSe/ZnS/OA CQDs, the latter's optical characteristics showed a red-shift in absorption and emission band. The exposition of both CQD structures to Hg^{2+} ions resulted in 100% quenching of fluorescence. For both CdSe/ZnS/OA and CdSe/ZnS/GSH, the limit of detection (LOD) was 74.8 nM and 54.8 nM, respectively.²²² Yasmeen Elkony *et al.* created new nanocomposite (PIn)/CuInS (CIS)/ZnS CQDs by polymerizing polyindole (Pin) *in situ* in the presence of CIS/ZnS CQDs. This nanocomposite was then utilized as a fluorescent probe to detect Pb^{2+} ions. When Pb^{2+} ions were present, the nanocomposite showed a quenching of the emission peak, with an accuracy of 0.0041 ppb⁻¹ and a detection limit of 4.48 ppb. Ion exchange processes or photo-induced electron transfer were thought to be responsible for the quenching.²²³ Salima Mabrouk *et al.* revealed another technique for detecting Pb^{2+} ions in water. They synthesized MPA-capped ZnSeS/Cu:ZnS/ZnS core/shell/shell CQDs with a PL quantum yield of 21% that glow at 500 nm. Pb^{2+} ions preferentially quenched these CQDs, offering a quick and accurate way to find Pb^{2+} in actual water samples. Under ideal circumstances, the PL intensity of ZnSeS/Cu:ZnS/ZnS CQDs demonstrated a linear dependency on Pb^{2+} concentration in the 0.04–6 μ M range (Fig. 17C), with a water detection limit of 21 nM. PL lifetime and UV-visible absorption data supported the dynamic quenching theory of the sensing mechanism.²²⁴ Quang-Bac Hoang *et al.*, on the other hand, reported the simultaneous detection of Pb^{2+} and Hg^{2+} , and they synthesized water-soluble, highly photoluminescent CdZnTeS alloyed CQDs. Concerning Pb^{2+} and Hg^{2+} , these alloyed CQDs showed size-dependent reactivity. The results of their investigation showed that Hg^{2+} might replace Cd^{2+} in the core CQDs and that Pb^{2+} and Hg^{2+} functioned as Z-type ligands to passivate Te^{2-} sites on the surfaces of CQDs, therefore increasing the PL intensity. The smaller the CQDs were, the greater the PL enhancement and the cation exchanging capacity. To put it briefly, the increased PL in the presence of Pb^{2+} and Hg^{2+} ions was caused by cation exchange and Z-type ligand interactions, which were part of the detecting process.²²⁵ Novel multifunctional carbon-CdTe quantum dots were developed by Jialing Zhou *et al.* for the simultaneous detection of hydrogen iron(II) (Fe_2^{+}) and peroxide (H_2O_2) in serum. The probe detected H_2O_2 with a linear relationship and a detection limit of 58 nM using dual-emission fluorescence. It then used the Fenton reaction and complexation

process to attain colorimetric measurement of hydroxyl radicals ($•OH$) and Fe^{2+} concentrations.²²⁶

(VI) Gas sensing. Besides sensing gas like H_2S and NO inside cells, CQDs have also been used in sensing gas outside cells. For example, Zhixiang Hu *et al.* followed an atomic ligand engineering strategy for stabilizing PbS CQD gas sensors. The halide ligands (Cl^- , Br^- , and I^-) were selected due to their stable chemical characteristics and wide atomic radius, which make them perfect for surface passivation. Halide ligands lowered sensitivity but greatly increased stability over the long run. With iodine ligands, the top-performing sensor showed an amazing 0.78 ppb NO_2 detection limit and great stability under different humidity conditions (0–90%). According to analysis, stabilization is facilitated by the large atomic radius and high binding energy of halide ligands. Increased surface passivation and p-type conductivity in the PbS-I CQD film result in better carrier collection and stability.²²⁷ Furthermore, Yong Zhang *et al.* built a room-temperature methanol gas sensor based on an alpha-iron oxide/polyaniline/lead sulfide quantum dot (α -Fe₂O₃/PANI/PbS CQDs) nanofilm [where α -Fe₂O₃ and PANI stand for alpha-iron oxide and polyaniline respectively]. The sensor demonstrated high responsiveness, selectivity, and repeatability at room temperature while detecting concentrations of methanol ranging from 10 to 100 ppm.²²⁸

(VII) Virus sensing. Semiconductor quantum dots have also been extensively studied in detecting viruses. To that end, Ghasem Rezanejade Bardajee *et al.* developed a DNA-conjugated CdTe/ZnS CQD nanoprobe that enables the quick identification of Covid-19 viral genome RNA (from an actual sample) or complementary (target) DNA as a positive control. In the detection process, sandwiched hybrids were created by adding varying amounts of complementary DNA (target DNA) to a combination of quencher DNA (BHQ_2 -labeled DNA) and CQD-DNA conjugates. The concentration of target DNA caused a corresponding drop in the fluorescence intensity. It was found that the limit of detection (LOD) was 0.000823 μ M. The efficacy of this approach in validating the RT-PCR method's findings in actual samples demonstrated its potential for rapid COVID-19 identification. The detection method was based on fluorescence-reduction-efficiency transfer (FRET), where an increase in target DNA concentration results in a decrease in fluorescence intensity due to the closeness of quencher DNA to CQD-DNA conjugates.²²⁹ Recently, Ghasem Rezanejade Bardajee *et al.* constructed a FRET-based nano-biosensor for the detection of the SARS-CoV-2 virus, employing Cy3 as the acceptor and oligonucleotide-modified CdTe/ZnS CQDs as donors. The detection limit of complementary target DNA (ctDNA) under optimal circumstances was determined to be $2.19 \times 10^{-9} \mu$ M. The nano-biosensor showed promise in tracking SARS-CoV-2 in actual specimens. The detection method used FRET, in which energy transfer occurs when the acceptor (Cy3) is close to the donor (CdTe/ZnS CQDs), resulting in a detectable shift in fluorescence intensity (Fig. 17D).²³⁰ Furthermore, Fan Yang *et al.* created a new electrochemiluminescence-resonance energy transfer (ECL-RET) biosensor for the identification of circulating tumor DNA

(ctDNA) with the crucial T790M mutation in lung cancer that is linked to the epidermal growth factor receptor (EGFR). The biosensor made use of hairpin DNA probes labeled with Au nanoparticles and capped CdS quantum dots. This ECL-RET system had an advantage over previous methods in that it could identify altered linear DNA molecules with distinctive mutations closer to the ends, unlike PCR-based techniques. With a T790M mutation at the end of a 100-nucleotide linear ctDNA fragment, the biosensor showed remarkable sensitivity, with detection limits as low as 3.4 aM. The process was found to be based on ECL-RET, in which quantifiable variations in electrochemiluminescence were caused by energy transfer between CdS quantum dots and Au nanoparticles, enabling accurate detection.²³¹

(3) **Biomedical application.** Semiconducting colloidal carbon quantum dots (CQDs), due to their superior photostability, high photoluminescence quantum yield (PLQY), and high absorption coefficient, have been extensively utilized in several medicinal applications. These include drug delivery, gene technology, *in vivo* bio-imaging, cell tracking, tumor biology research, fluorescent labeling of cellular proteins, pathogen and toxin detection, and biosensing.²³³ However, concerns regarding toxicity sometimes arise, which leads to the investigation of substitute materials.^{234,235} Silver-based CQDs, such as Ag₂S, AgInS₂, Ag₂Se, Ag₂Te, etc. have shown promise as viable substitutes in biological applications because of their advantageous characteristics and lower toxicity.²³⁶

(I) *Bio-imaging.* Semiconductor colloidal quantum dots (CQDs) serve an important role in bioimaging by acting as adaptable labels and contrast agents, as outlined in Table 5. When compared to traditional fluorophores, CQDs offer several advantages including their compact sizes for cell labeling, unique optical and electrical properties, well-established surface functionalization, and multimeric binding capabilities. As a result, CQDs become a good candidate for enhancing targeting efficiency, especially in scenarios where long-term photoluminescence stability, high brightness, and multi-color detection are essential.

Yufgang Zheng *et al.* reported that glutathione (GSH)-capped CdTe CQDs internalize the cellular membrane through the phagocytosis process and accumulate in the cytoplasm and nuclei with distribution depending on the CdTe CQD size. Smaller GSH-capped CdTe CQDs tend to stain the nuclei, while larger ones are more likely to stain the cytoplasm. This distinction arises because smaller CdTe CQDs can readily penetrate the nuclei, while larger ones face difficulty in accessing this cellular compartment. Additionally, they have bio-conjugated these GSH-capped CdTe CQDs with biotin for immunostaining and F3 peptide for delivery to tumor cells to demonstrate GSH-CdTe CQD's potential as a biomarker.²³⁷ To scan pancreatic cancer cells, Ken-Tye Yong *et al.* synthesized photostable, biocompatible, water-dispersible, and Cd-free indium phosphide (core)-zinc sulfide (shell), or InP/ZnS CQDs. To deliver the InP/ZnS CQDs in pancreatic cancers like MiaPaCa and the low passage cell line, XPA-3, they functionalized the CQD with antibodies like anti-claudin 4 and anti-prostate stem cell antigen (anti-PSCA), whose corresponding antigen receptors are known to be over-expressed in both primary and metastatic pancreatic cancers. In contrast to the poorer staining of the bioconjugates in receptor-negative (KB) cells, they demonstrated receptor-mediated absorption of the bio-conjugated InP/ZnS CQDs in MiaPaCa cells, which is supported by their strong cellular staining.²³⁸ Nevertheless, Chuanzhen Zhao *et al.* reported the versatile and facile way to synthesize water-soluble CuInS₂/ZnS and CuInSe₂/ZnS-based CQDs for biological application. They first synthesized CuInS₂/ZnS and CuInSe₂/ZnS CQDs in organic solvent, and after that, they introduced these CQDs into aqueous media from organic solvent through a ligand exchange method using glutathione (GSH) as a capping agent and 3-mercaptopropionic acid as an additive ligand without significant change in phenolamines quantum yield (PLQY). To understand the potential use of these CQDs, they incubated GSH-capped CuInS₂/ZnS into MCF10CA1a breast tumor cells. They observed that a large fraction of CuInS₂/ZnS CQDs have stained cytoplasm just like in the above-mentioned Yufgang Zheng *et al.* report and minor fractions are in the

Table 5 Illustration of ligand-modified CQDs for bioimaging application

Materials	Functionalized ligands	Cell lines	Specificity	Ref.
CdTe CQDs	GSH	HepG2	Nucleoli (small CQDs) and cytoplasm (large CQDs)	237
InP/ZnS CQDs	Anti-claudin 4 and anti-prostate stem cell antigen	MiaPaCa, XPA-3	<i>In vitro</i> targeting of pancreatic cancer cell lines	238
CuInX ₂ /ZnS CQDs (X = S, Se)	GSH	MCF10CA1a	Cytoplasm and perinuclear area	239
InP/ZnSe/ZnS CQDs	Chitosan, mitochondria monoclonal antibody, and α -tubulin monoclonal antibody	BS-C-1	Microtubules, mitochondria, and lysosomes	240
CdSe/ZnS CQDs	Antibody	HepG2	Microtubules	241
CdSe/CdS CQDs	Bradykinin	Hippocampal neuronal and glial	—	242
CdSe CQDs	—	HeLa	Microtubules	243
CdSe CQDs	Anti- $\alpha v\beta 3$ human antibody (LM 609)	Glioblastoma cell lines (U87MG, U251, A172)	Integrin $\alpha v\beta 3$	244
CdTe CQDs	BSA	HeLa	Lysosomes	245
CdSe/ZnS CQDs	L-Cysteine-polyamine-morpholine	HeLa	Lysosome	246
CdTe CQDs	CD68 ab (lysosomes), mitochondria ab, nuclear antigen ab, and smooth muscle actin ab	HepG2	Lysosomes, mitochondria, nucleus, and actin	247

perinuclear area.²³⁹ Furthermore, practically nonblinking water soluble core-multishell InP/ZnSe/ZnS CQDs with great photostability, antiphotosensitivity, and good biocompatibility were synthesized by Liangliang Zhou *et al.* The plan calls for the synthesis of the InP core, the oil-phase core-multishell InP/ZnSe/ZnS CQDs using hydrogen fluoride and trioctylphosphine (HF-TOP) etching passivation, and then MPA to promote the water solubility and surface coupling technology to improve the targeting of the core-multishell InP/ZnSe/ZnS CQDs. Following that, they bioconjugated InP/ZnSe/ZnS CQDs using three distinct antibodies: chitosan, mitochondria monoclonal antibody, and α -tubulin monoclonal antibody, which were used to mark microtubules, mitochondria, and lysosomes, respectively.²⁴⁰ Following these findings, Jianquan Xu *et al.* showed multiple color super-resolution imaging of microtubules with commercially available antibody conjugated CdSe/ZnS CQDs (core/shell) without losing resolution (Fig. 18), demonstrating that blue-shifted CQDs could be managed to maximize the number of imaged localizations. They also employed Quenched Stochastic Optical Reconstruction Microscopy (QSTORM) using high photon count CQDs to assess microtubule widths and two CQDs with significantly varying excitation wavelengths to split their emission into discrete channels. With the use of these CQDs, they were able to attain a resolution of microtubules as high as 46 nm.²⁴¹ Jennifer M. Urban *et al.* utilized

CdSe/CdS CQDs to image neurons. To do so they functionalized CdSe/CdS CQDs with a neuropeptide (BK-CQDs; BK: bradykinin) and they observed that BK-CQDs produced better STORM images than a BK-labelled organic commercial fluorophore (TAMRA-BK). STORM images of primary rat hippocampal neuronal cultures acquired with the BK-CQD probe have higher localization accuracy than comparable images obtained with TAMRA-BK. This was partly attributed to significantly increased fluorescence intensity and, as a result, a better signal-to-noise ratio when compared to the organic fluorophore. BK-CQDs were also discovered to “blink” at a faster pace, and as expected BK-CQDs demonstrated higher photobleaching stability.²⁴² Xusan Yang *et al.* used commercially available streptavidin-conjugated (SC) CdSe CQDs to unveil microtubule networks through stimulated emission depletion (STED) and structured illumination microscopy (SIM).²⁴³ Tingting Wang *et al.* used anti-mouse IgG (H + L)-conjugated CdSe CQDs to demonstrate the distribution and density of integrin $\alpha v \beta 3$ in single glioblastoma cells, highlighting how drug vulnerability relates to receptor density on test cells and demonstrating glioblastoma phenotypic variability at the single-cell level.²⁴⁴

Kush Kaushik *et al.* used bovine serum albumin (BSA) functionalized CdTe CQDs to visualize lysosomes. Their study revealed that BSA does not only minimize the toxicity of CdTe CQDs but also provides the lysosomal super-resolution image's

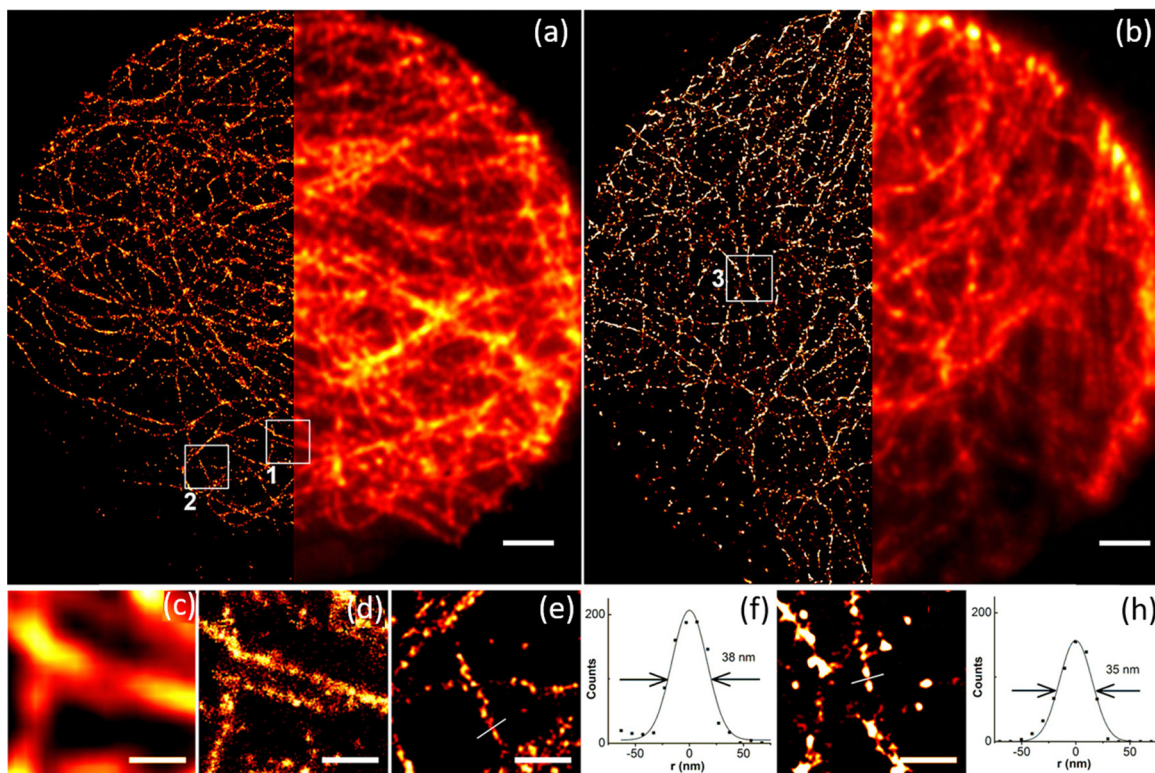


Fig. 18 STORM (left) and wide-field (right) images of microtubules in HepG2 cells labeled with 565 and 705 nm CQDs, (a) and (b) respectively. The scale bar is 2 μ m. Wide-field and STORM images of box 1 in (a), (c) and (d) where the scale bar is 500 nm. STORM image of box 2 in (a) in which the scale bar is 500 nm (e). A cross-section of a microtubule is shown in (f). The full width at half-maximum is 38 nm. STORM image of box 3 in (b) and (g). The scale bar is 500 nm. A cross-section of a microtubule is shown in (h). The full width at half-maximum is 35 nm. Reproduced with permission from ref. 241. Copyright 2015 American Chemical Society.

resolution down to ~ 60 nm (Fig. 19).²⁴⁵ Similarly, Zhi-Qiang Zhang *et al.* synthesized L-cysteine–polyamine–morpholine-modified CdSe/ZnS CQDs that are water soluble and equally disseminated. Because of the presence of the morpholine unit on the surface of these L-cysteine–polyamine–morpholine-

modified CdSe/ZnS CQDs, they were found to be highly selective to the lysosome, making them fluorescent probes that can be targeted to lysosomes.²⁴⁶ Recently, CdTe CQDs with four distinct color coatings made of polydimethyl siloxane (PDMS) were produced by Sulaxna Pandey *et al.* (blue, green, yellow,

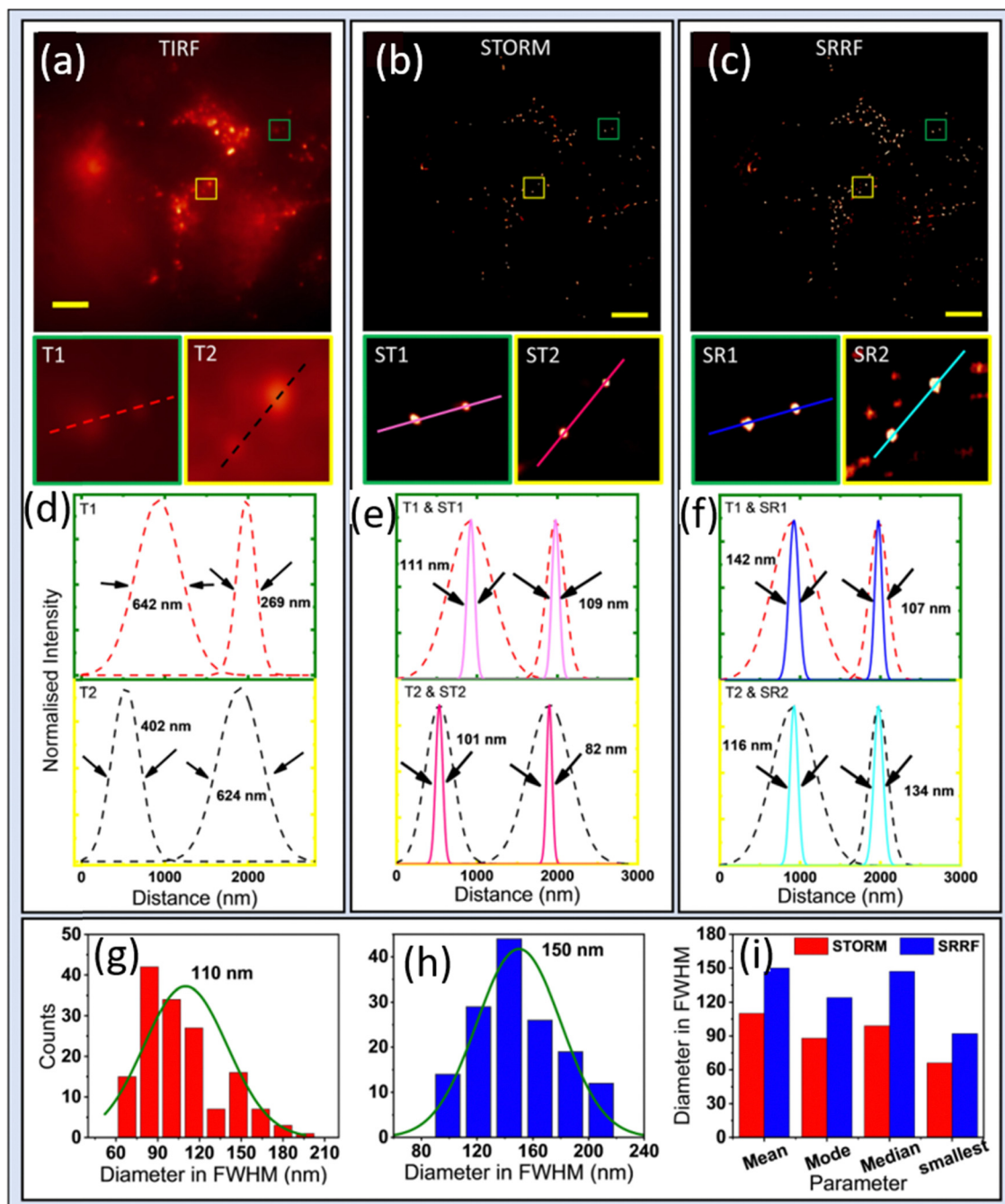


Fig. 19 The TIRF, STORM, and SRRF images are obtained from the same stack of videos recorded for HeLa cells stained with BSA-CQDs which are found to stain lysosomes (scale bar 5 μm) shown in (a), (b) and (c) respectively. The zoomed-in images of the green and yellow boxes in the image (a), (b) and (c) are shown in [T1 and T2], [ST1 and ST2], and [SR1 and SR2] respectively. The line profile of this zoomed-in image is plotted in (d), (e) and (f) [color-coded]. Then the distribution of lysosomes' FWHM from STORM and SRRF are shown in (g) and (h) respectively. A comparison of statistical parameters mean, mode, median, and smallest lysosomes for a better understanding of the distribution of FWHMs is displayed in (i). Baseline correction was performed in the TIRF image, and two peak Gaussian fitting was performed for all line profiles (d)–(f). Reproduced with permission from ref. 245. Copyright 2022 John Wiley and Sons.

Table 6 Summary of CQD-based biosensor applications

Materials	Biosensing molecules	Detection method	Sensitivity	Detection limit	Detection range	Ref.
CdSe/ZnS CQDs	ROS	Modulation of emission intensity	—	—	—	250
AgInS ₂ CQDs	H ₂ O ₂	Modulation of emission intensity	—	0.42 μM	—	251
Si-CdTe CQDs	H ₂ O ₂	Modulation of emission intensity	—	79 nM	—	252
Ag ₂ S CQDs	ONOO [−]	Restoration of CQD emission	—	0.06 μM	—	253
CuInZnS CQDs	SOD	Modulation of ECL signal	—	0.03 μg mL ^{−1}	—	254
PbS/CdS/ZnS CQDs	Temperature	Modulation of emission intensity	1% °C ^{−1}	—	20–70 °C	255
CdSe CQD	Temperature	Shifting of emission wavelength	58.5 pm °C ^{−1}	—	25–48 °C	256
AgInS ₂ CQDs	Temperature	Change in emission intensity	−2.82% °C ^{−1}	—	—	257
Ag ₂ S CQDs	pH	Fluorescence intensity increased	—	—	2.1–7.2	258
Ag ₂ S CQDs	pH	Modulation of emission intensity	—	—	5.0–9.0	259
CdTe CQDs	H ₂ S gas	Restoration of CQD emission	—	15 nM	—	260
DCNP@HSA-Ag ⁺ nanoprobe	H ₂ S gas	Modulation of emission intensity	—	0.22 mM	0–9 mM	261
Ag ₂ S CQDs	Cyt c	Quenching of CQD emission	—	1.7 nM	2.0–150 nM	262
CuInS ₂ /ZnS CQDs	Cyt c	Decline in emission intensity	—	1.1 nM	0.01–7 μM	263
Ag ₂ S CQDs	ALP	Modulation of emission intensity	—	1.28 μM mL ^{−1}	2–100 μM mL ^{−1}	264
Ag ₂ S CQDs	Heparin, heparinase I	Modulation of emission intensity	—	6 nM (heparin) 0.5 ng mL ^{−1} (heparinase I)	0.069–2.275 μM (heparin) 0–103 ng mL ^{−1} (heparinase I)	265
CQDs	EGFR	Decrease in FRET signal	—	80 ± 20 pM	—	266
CdSe/ZnS CQDs	MMP-14	Change in the emission intensity of CQDs	—	—	—	267
MnS:CdS@ZnS CQDs	miRNA let-7a	Modulation of ECL signal	—	4.1 aM	10 aM–1 nM	268
InP CQDs	AFP	Increase in emission intensity	—	0.58 ng mL ^{−1}	—	269
CuInS ₂ /ZnS CQDs	Cd ²⁺	Enhancement of emission intensity	—	—	—	270
Supramolecular systems	Pb ²⁺	Change in the emission intensity of the system	—	—	—	271

and orange). Then, employing EDC-NHS chemistry, they attached them to CD68 ab (lysosomes), mitochondria ab, nuclear antigen ab, and smooth muscle actin ab, respectively, to concurrently scan cellular organelles such as HepG2 lysosomes, mitochondria, nucleus, and actin.²⁴⁷

(II) *Biosensing*. In the past several years, another noteworthy advancement in CQDs has been the development of a sensor for deployment in biosensing applications.^{248,249} CQDs can alter their fluorescence intensity or emission wavelength in response to particular microenvironmental factors which allows them to exhibit superior sensitivity, specificity, and signal-to-background ratios in comparison to other fluorophores, making them ideal options for sensing applications. Thus far, CQDs have been widely used to sense various substances such as reactive oxygen species (ROS), reactive nitrogen species (RNS), superoxide dismutase (SOD), temperature, gas, pH, heavy metals detection in cells, and cancer biomarkers or a particular enzyme, which can be seen in Table 6 with potential detection limits and detection ranges, opening up possibilities for understanding the molecular level biological activities of cells and tissues. Thus, both native and conjugate CQDs may be used to build these CQD-based biosensors, and the appearance or modification of CQD luminescence can be used to detect the presence of target biomolecules.

ROS/RNS/SOD sensing. Numerous diseases, including cancer, tissue damage, infections, and others, are linked to the establishment and progression of an imbalance in the redox environment within the organism.^{272,273} Several studies, including sensing of reactive oxygen species (ROS), reactive nitrogen species (RNS), and superoxide dismutases (SOD), have

been developed with the use of CQDs to track the redox status of organisms.

In 2018 Bong H. Lee *et al.* synthesized ROS-sensitive CdSe/ZnS core/shell type CQDs. They showed that the fluorescence emission spectra of the CQDs is modulated in the presence of ROS produced by common chemotherapeutic drugs, daunorubicin and doxorubicin, and by cells following chemotherapy/radiotherapy.²⁵⁰ In some cases, Si CQDs have been combined with semiconductor CQDs to reduce their toxicity and enhance their selectivity for the sensitive detection of hydrogen peroxide (H₂O₂).^{251,252} For RNS, Chunyan Li *et al.* developed an Ag₂S CQD ONOO[−] activatable probe for traumatic brain injury (TBI) imaging using the principle of Förster resonance energy transfer (FRET) (Fig. 20A). They conjugated the ONOO[−]-responsive A1094 chromophore with Ag₂S CQDs to generate the V&A@Ag₂S probe. The fluorescence intensity of V&A@Ag₂S CQDs remains quenched as a result of the FRET between Ag₂S CQDs and A1094 when they are intact, however, the fluorescence of Ag₂S CQDs is activated and A1094 is quickly quenched after being exposed to ONOO[−].²⁵³ Yang Liu *et al.* fabricated an easy-to-use and fast visual electrochemiluminescence (ECL) sensor made of CuInZnS CQDs for SOD detection (Fig. 20B). In the sensing process, CuInZnS CQDs served as the ECL luminescence (ECL) signal emitted by the CuInZnS CQDs gradually decreased as the concentration of SOD increased. This signal-quenching effect served as a reliable indicator of the SOD concentration in the sample down to 0.03 μg mL^{−1}.²⁵⁴

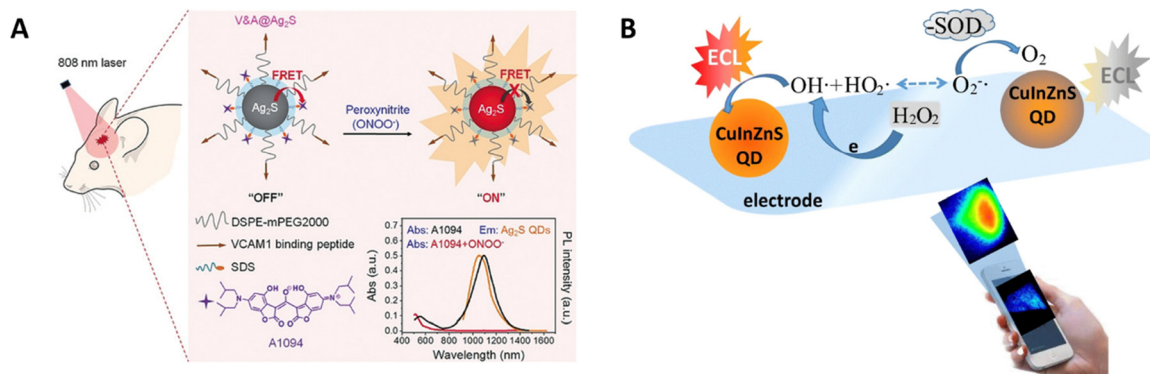


Fig. 20 (A) A schematic illustration of the construction of the V&A@Ag₂S probe and detection of ONOO⁻ *in vivo*. The exposure of ONOO⁻ activates the probe to restore the fluorescence of Ag₂S CQDs by forming a complex with an A1094 quencher. (B) A schematic illustration of the ECL sensor for determination of SOD. CulnZnS and SOD compete for H₂O₂ which acts as a working mechanism for SOD detection. If the SOD concentration is increased, the ECL signal emitted by the CQDs starts decaying. Reproduced with permission from ref. 253. Copyright 2020 John Wiley and Sons. Reproduced with permission from ref. 254. Copyright 2020 Springer Nature.

Temperature sensing. One of the most crucial physiological characteristics of every given organism is its temperature. Antonio Benayas *et al.* synthesized high-quality water-soluble NIR emitting PbS/CdS/ZnS CQDs. In this work, they found that these PbS/CdS/ZnS CQDs showed a significant temperature-dependent fluctuation in emission intensity. The results indicate that CQDs have potential for temperature sensing in biological systems, as evidenced by their 1% °C⁻¹ sensitivity across a temperature range of 20 to 70 °C. Then, an *ex vivo* investigation using breast tissue from chickens revealed that thermally sensitive CQDs could detect tissue temperature down to a depth of one centimeter (Fig. 21).²⁵⁵ Furthermore, Ninik Irawati *et al.* and his co-workers developed a noncontact temperature sensor by using the wavelength shifts of CdSe CQD-doped poly(methyl methacrylate) microfiber. Their results suggested that the CdSe CQD-doped polymer microfiber (PMF) sensor exhibited a remarkable performance, with a high sensitivity of 58.5 pm °C⁻¹, which was approximately 18 times greater than that of the undoped PMF's temperature sensitivity. Moreover, the sensor demonstrated a linear temperature range suitable for physiological measurements, opening possibilities for accurate and stable optical temperature sensing in various applications.²⁵⁶ For the precise and real-time observation of the exothermic behavior of organisms in enzymatic processes at the nanoscale, a novel approach was devised using enzyme–CQD conjugates. The method being used entailed chemically grafting temperature-sensitive amino-AgInS₂ CQDs onto the enzyme to produce -2.82% °C⁻¹ nanothermometers. The fluorescence intensity fluctuations of the quantum dots were utilized as nanothermometers to track the thermal behavior of enzymes in real time. During catalysis, the enzyme–CQD conjugates showed good repeatability with a maximum error of 4% and temperature differences as high as 6 °C above ambient temperature in nano-microregions. The method yielded a detection limit of 0.02 mg mL⁻¹ of enzyme and a temperature resolution of around 0.5 °C.²⁵⁷

pH sensing. The value of pH plays an important role in biological systems, and abnormal pH can also be used as a

pathological microenvironment feature for the diagnosis and treatment of diseases. Recently, Donghui Zhao *et al.* synthesized genetically engineered polypeptide stabilized core/shell Ag₂S CQDs which show pH-responsive fluorescence. They observed that Ag₂S CQDs showed a good linear relationship between fluorescence intensity and pH value in the range of 2.1–7.2. When pH changed from 7.2 to 2.1, the fluorescence intensity increased dramatically, suggesting that Ag₂S CQDs have the potential to serve as pH sensors for applications under acid conditions.²⁵⁸ Nevertheless, Caiping Ding *et al.* designed a luminescence resonance energy transfer (LRET) system UCNPs@SiO₂–Ag₂S using near-infrared (NIR) Ag₂S CQDs as the energy acceptors and upconversion nanoparticles (UCNPs) as the energy donors for pH biosensing and bioimaging (Fig. 22A). They co-modified Ag₂S CQDs with glutathione and mercaptopropionic acid (MPA) and then covalently linked them with silica-coated UCNPs. Their finding suggested that the fluorescence intensity of Ag₂S CQDs collected in the red region of confocal microscopy starts increasing while the green luminescence from the UCNPs in the green channel remains mostly unchanged when the pH of the HeLa cell is changed from 5.0 to 9.0. This behavior demonstrated a strong and linear relationship between the intensity ratio of red and green luminescence and the pH value within the range of 5.0–9.0. They observed a similar trend in fluorescence intensity change with the UCNPs@SiO₂–Ag₂S LRET system when the pH changed in tumor-bearing zebrafish (Fig. 22B). Therefore, the CQD modified UCNPs@SiO₂–Ag₂S probe can be used to image pH *in vivo*.²⁵⁹

Gas sensing. CQDs have also been used for gas sensing within cells. In one study, activatable fluorescence nanoprobe-based quantum dots known as CQD/AgNP nano complexes were created through a strong electrostatic interaction between thioglycolic-acid-stabilized CdTe CQDs and *p*-amino thiophenol capped silver nanoparticles (AgNPs) which showed an excellent H₂S response in the lysosome of live cancer cells with a detection limit of 15 nM. Initially, the fluorescence intensity of CQDs was quenched by the AgNPs due to an inner filter effect. However, when exposed to H₂S, the CQD/AgNP nano

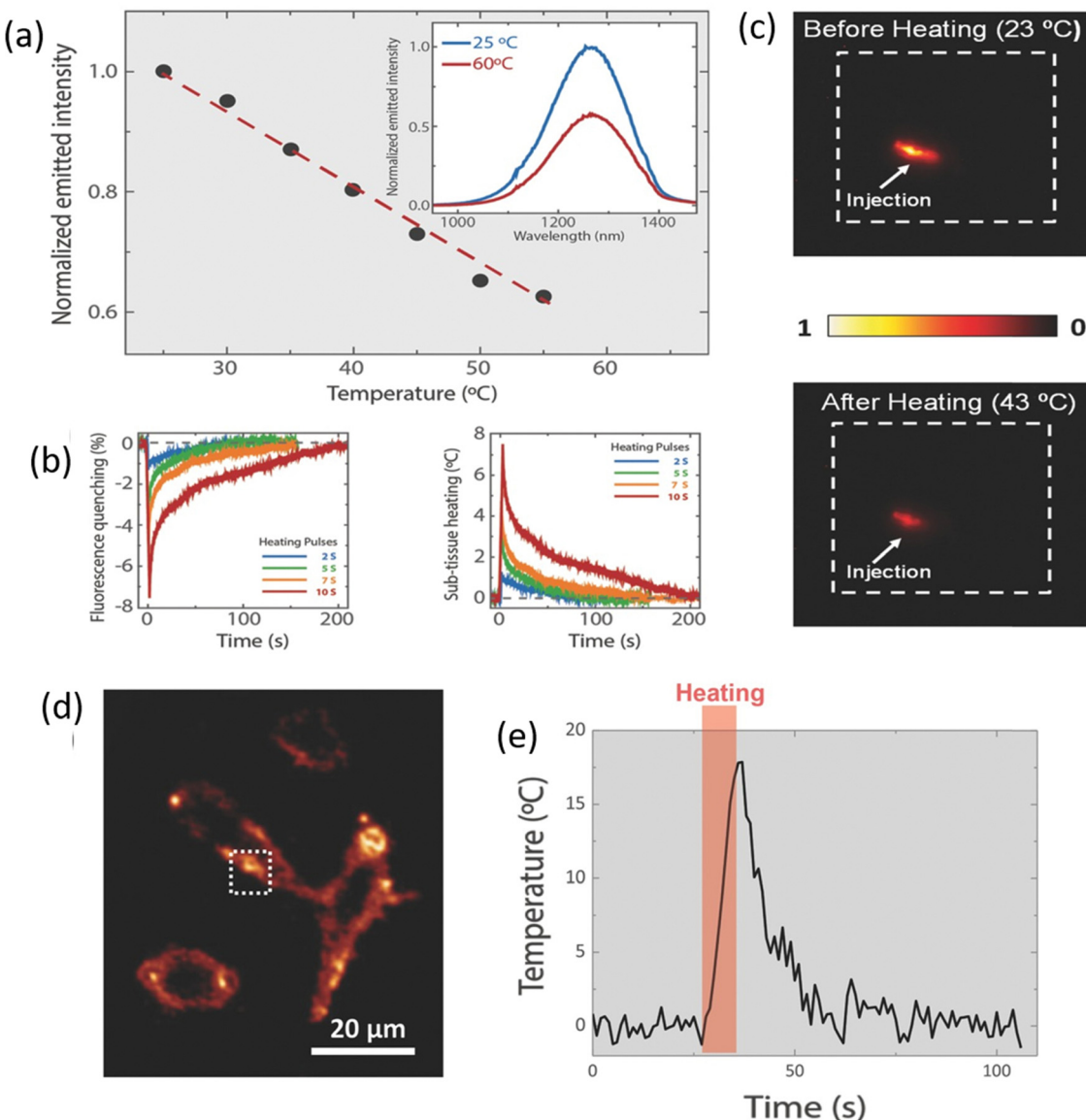


Fig. 21 Emission intensity (normalized by the values measured at room temperature) was collected from CQDs emitting at 1270 nm as a function of the induced temperature of the solution. The inset shows two spectra recorded at the two extreme values (25 and 60 °C) of the temperature span studied (a). Intensity recorded *versus* time from the CQDs after heating the chicken breast tissue using short hot-air pulses. The translation of the time evolution of the fluorescence quenching (left graph) into the corresponding time evolution of the subtissue heating process (right side graph) (b). Subtissue fluorescence images were taken at two different temperatures from the chicken breast previously injected with CQDs emitting at 1270 nm (c). Fluorescence image of four HeLa cells, upon their excitation with an 808 nm laser diode. The cells had been previously incubated with a solution of 1270 nm emitting CQDs [the white dashed square in the figure on the left shows the area under temperature monitoring] (d). Continuous monitoring of the temperature of the HeLa cells before, during, and after a 10 s heat pulse, as a function of time (e). Reproduced with permission from ref. 255. Copyright 2015 John Wiley and Sons.

complexes disassembled, leading to the generation of Ag_2S on the surface of CQDs. This resulted in $\text{CdTe}/\text{Ag}_2\text{S}$ core–shell CQDs with increased fluorescence (Fig. 23).²⁶⁰ Moreover, Chenlu Wang *et al.* developed a NIR-II ratiometric fluorescence nanoprobe for quantitatively detecting and imaging hydrogen sulfide (H_2S) *in vivo*. They used down-conversion nanoparticles (DCNPs) as carriers, which later coordinated with Y^{3+} and Ag^+ through human serum albumin (HSA) to create a DCNP@HSA- Ag^+ nanoprobe. The DCNPs give emission but emission is a lot upon coordination with Ag^+ . In the presence of H_2S , the DCNP@HSA-

Ag^+ nanoprobe gets activated and generates Ag_2S CQDs *in situ* through an H_2S -induced chemical reaction between H_2S and Ag^+ (Fig. 24A). In this study, the ratio metric NIR-II FL intensity between active mode and non-active mode exhibited a linear relationship with endogenous H_2S concentration (0 to 9 mM) along with a detection limit down to 0.22 mM.²⁶¹

Biomolecule sensing. CQDs were found to be a great choice for detecting cell-related signaling biomolecules such as cytochrome *c* (Cyt *c*) and alkaline phosphatase (ALP) activity.

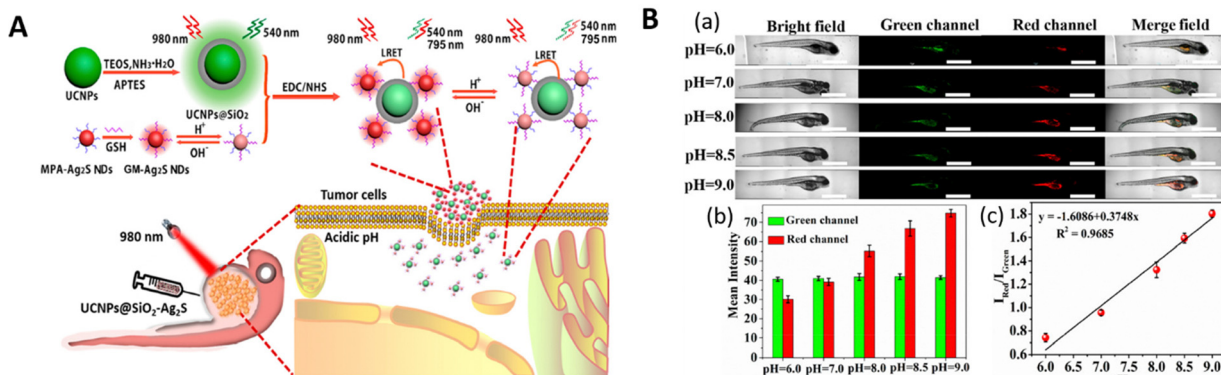


Fig. 22 (A) Schematic illustration of the developed LRET nanoparticle as a ratiometric nanoprobe using pH-responsive GM-Ag₂S NDs as the energy acceptor and UCNPs as the energy donor in tumor cells and tumor zebrafish. (B) Confocal imaging of normal zebrafish incubated with UCNP_s@SiO₂-Ag₂S at different pH values excited at 980 nm (a), luminescence intensity histogram, and the linear relationship between the luminescence intensity ratio of UCNP_s@SiO₂-Ag₂S and pH shown in (b) and (c) respectively. Scale bar = 1000 μm. Reproduced with permission from ref. 259. Copyright 2019 American Chemical Society.

Meifang Cai *et al.* developed a label-free technique for the sensitive and specific detection of cytochrome *c* (Cyt *c*) by using Ag₂S CQDs. In this reaction, trypsin hydrolyzed Cyt *c*, resulting in the formation of a heme-peptide fragment with a peroxidase-

like activity that stimulated the conversion of H₂O₂ into hydroxyl radicals (•OH). Because of the potent oxidizing power of (•OH) in the presence of caffeic acid, caffeic acid-quinone was formed, which subsequently caused the fluorescence of Ag₂S

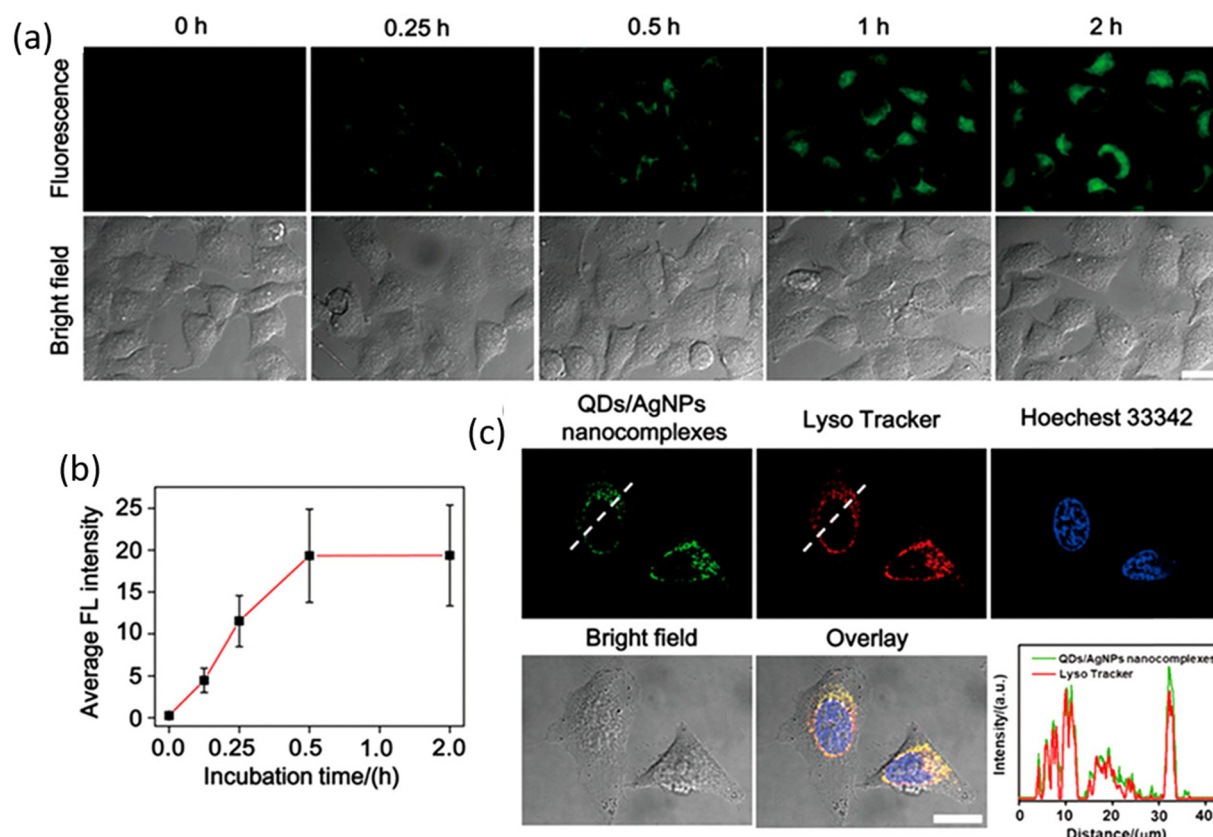


Fig. 23 Time-dependent fluorescence images of HeLa cells incubated with 3.5 μM CQD/AgNP nano complexes for 0, 0.25, 0.5, 1.0, and 2.0 h, respectively. Scale bar: 20 μm (a). Quantification of the mean fluorescence intensity of HeLa cells (b). Fluorescence images of the assembled CQD/AgNP nano complex-loaded HeLa cells following staining with either lysosomal tracker (LysoTracker Red DND-99) or nucleus dye (Hoechst 33342). HeLa cells were treated with 3.5 μM QD/AgNP nanocomplexes for 1 h and then costained with 1 μM LysoTracker Red and 2.0 μg mL⁻¹ Hoechst 33342 for 20 min. Scale bar: 20 μm (c). Reproduced with permission from ref. 260. Copyright 2018 American Chemical Society.

CQDs to be quenched *via* an electron transfer process. Cyt *c* could be detected using this method with a low detection limit (LOD) of 1.7 nM and a linear range of 2.0 to 150 nM.²⁶² In a different study, Xiangyang *et al.* designed negatively charged core-shell CuInS₂/ZnS-GSH CQDs for the sensitive detection and bio-imaging of Cyt *c*. In this study, the fluorescence intensity of CQDs is significantly reduced as soon as it interacts with Cyt *c*. The mechanism involved the interaction between the electron-deficient heme group in Cyt *c* and the electron-rich CuInS₂/ZnS-GSH CQDs through a photo-induced electron transfer process. This method offered a LOD of 1.1 nM and a linear range from 0.01 to 7 μmol L⁻¹ for Cyt *c* concentration.²⁶³ For alkaline phosphatase (ALP) detection, Meifang Cai *et al.* developed a ratiometric fluorescence comprised of calcein and near-infrared (NIR) and green fluorescence from Ag₂S CQDs (Fig. 24B). Both the near-infrared (NIR) and green fluorescence from Ag₂S CQDs were observed in this system at the same excitation wavelength. The fluorescence intensity of Ag₂S CQDs increased because of aggregation-induced emission (AIE) in the presence of Ce³⁺, but calcein's fluorescence dropped as a result of static quenching. Phosphate ions generated by the hydrolysis of *p*-nitrophenyl phosphate by ALP exhibited greater affinity toward Ce³⁺ than toward Ag₂S CQDs and calcein. Consequently, NIR fluorescence from Ag₂S CQDs dropped whereas green fluorescence from calcein was recovered again. The LOD was determined to be 1.28 μM mL⁻¹, and the ratio of the fluorescence signals (green/red) was linearly associated with ALP concentration in the range of 2–100 μM mL⁻¹. Additionally, this sensor has been effectively used to test for ALP inhibitors and detect ALP in human serum.²⁶⁴

Cancer biomarkers and antigen sensing. Cancer biomarkers like heparin, heparinase, metalloproteinase-14 (MMP-14), and miRNA have been selectively sensed by CQDs through methods like aggregation-induced emission (AIEE),²⁶⁵ Förster resonance energy transfer (FRET),^{266–274} immunosensor like electrochemiluminescence (ECL),²⁶⁸ and photoelectrochemical (PEC).²⁷⁵ Dan Yan *et al.* designed a novel dual-detection probe based on a “turn-on-off” fluorescence method for sensitive and selective detection of heparin and heparinase I using polyethyleneimine (PEI)-modified Ag₂S (PEI-Ag₂S CQDs). Heparin was identified through AIEE enhancement that resulted from its electrostatic interaction with the PEI-Ag₂S CQDs. Next, heparinase I was identified by its unique heparin hydrolysis, which disrupted Ag₂S CQD aggregation and AIEE (Fig. 24C). The approach showed a linear connection with heparin and heparinase I concentrations under ideal circumstances, with good correlation coefficients and LODs of 6 nM and 0.5 ng mL⁻¹ respectively.²⁶⁵ Recently, to detect microRNA let-7 (miRNA let-7a) Yu-Ting Yang *et al.* and his co-workers developed an ultrasensitive electrochemiluminescence (ECL) “signal-off” biosensor. They employed highly efficient MnS:CdS@ZnS core–shell CQDs as ECL lumophores. To enable signal amplification, the biosensor used strand displacement amplification (SDA) to transform miRNA let-7a into output DNA labeled with ferrocene (Fc). Because of the MnS:CdS@ZnS CQDs’ strong ECL response, the biosensor first functioned in “signal-on” mode. But when Probe DNA1 and

Probe DNA2 accumulated the output DNA and formed a quenching “Y” structure, it switched to a “signal-off” state.²⁶⁸ FRET strategies can be effectively utilized with CQDs for sensing applications by functionalizing them with specific molecules such as dyes^{267,274} or nanobodies (NBs).²⁶⁶ For instance, in a study by Zhicheng Jin *et al.*, CQDs were conjugated with rhodamine derivative dyes for sensing MMP-14. The fluorescence intensity of the CQDs exhibited a gradual increase, while concurrently, the intensity of the dye gradually decreased in response to the concentration of MMP-14. This increase is attributed to the disruption of FRET between CQDs and the rhodamine dye. As the concentration of MMP-14 rises, it forms bonds with the rhodamine dye, leading to the modulation of FRET and subsequent changes in the fluorescence intensity of the CQDs.²⁶⁷ Nevertheless, Ruifang Su *et al.* created a flexible and straightforward biosensing technique for the detection of the epidermal growth factor receptor (EGFR) and other biomarkers. They effectively functionalized CQDs by attaching nanobodies (NBs) with various C-terminal tags. This method facilitated the development of a speedy and wash-free immunoassay. In this experiment, when EGFR attached to terbium complex (Tb)-labeled nanobodies, they were eliminated from CQD surfaces. The displacement resulted in an EGFR concentration-dependent decrease of the Tb-to CQD Förster resonance energy transfer (FRET), which made it possible to quantify EGFR. They achieved a remarkable LOD of 80 ± 20 pM (16 ± 4 ng mL⁻¹) for quantification of the epidermal growth factor receptor (EGFR).²⁶⁶ Yanbin Zhang *et al.* synthesized InP-based core/shell CQDs for the detection of alpha-fetoprotein (AFP, serum markers of hepatocellular carcinoma [HCC]) antigen by coupling the alpha-fetoprotein by using a CQD-based fluorescence-linked immunosorbent assay (FLISA), which enabled a low detection limit of 0.58 ng mL⁻¹ to be achieved. The fluorescence intensity of CQDs increases as the concentration of AFP increases.²⁶⁹

CQDs have also been extensively used in metal atom sensing and imaging within cells. For example, Jia Liu *et al.* designed two amino acid *i.e.* cysteine (Cys) and threonine (Thr) capped CuInS₂/ZnS core/shell CQDs (CIS/ZnS CQDs) for the selective determination and multicolor imaging of Cd²⁺ ions. Their study demonstrated that the Cys- and Thr-capped CIS/ZnS CQDs can sense Cd²⁺ specifically rather than other metal ions such as Zn²⁺, Ca²⁺, Fe³⁺, etc. The photoluminescence intensity of these CQDs is enhanced when they interact with Cd²⁺ due to cation exchange, where some of the Zn²⁺ on the surface of the CQDs is replaced by Cd²⁺ but the intensity does not improve when exposed to other metal ions because ZnS shells are immune to these metal ions given cation exchange. Furthermore, they evaluated intercellular Cd²⁺ with the help of these CQDs based on intensity enhancement. The intensity significantly increases as the Cd²⁺ concentration increases.²⁷⁰ Ying-Jie Li *et al.* utilized supramolecular systems to form fluorescent CQDs for *in situ* detection of Pb²⁺ in living cells. They designed a tetra-pillar[5]arene derivative (H) as the host, which, along with an amphiphilic guest (G), assembled into supramolecular systems, forming non-fluorescent nanoparticles. Upon introducing S²⁻, the nanoparticles crosslinked, transforming into fluorescent

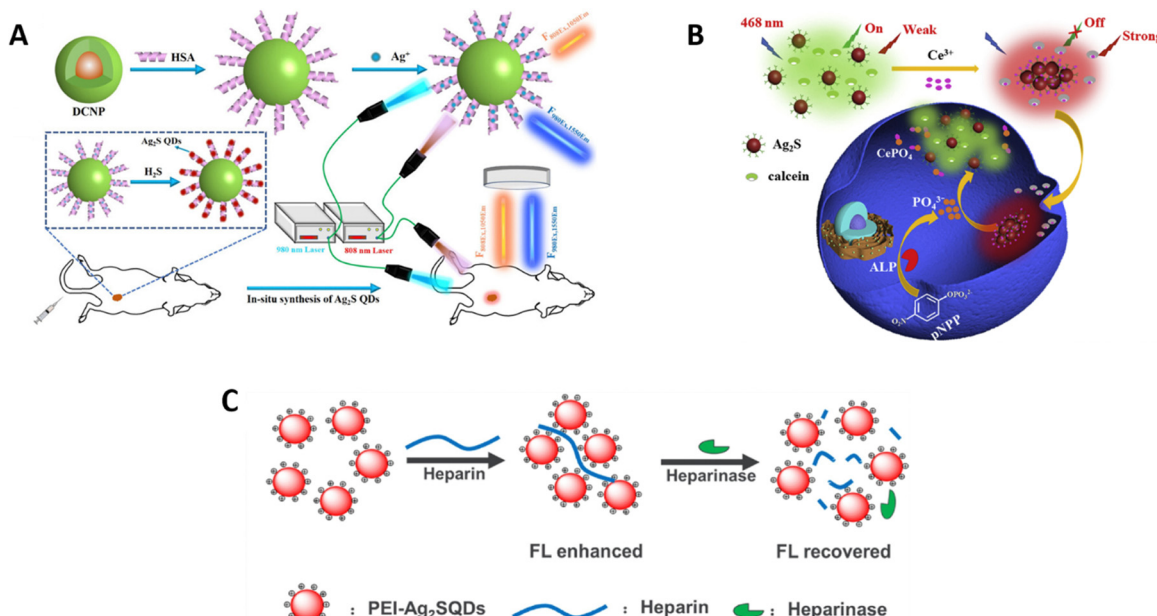
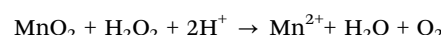


Fig. 24 (A) Schematic diagram of the preparation of DCNP@HSA-Ag⁺ nanoprobe (a). Schematic diagram of the endogenous H₂S-triggered *in situ* formation of Ag₂S CQDs in the DCNP@HSA-Ag⁺ nanoprobe for the NIR-II FL imaging of orthotopic colon tumors in mice (b). The FL signal response at 1050 nm in Ag₂S CQDs excited by an 808 nm laser (F1050, 808Ex) is turned on, whereas the FL signal of DCNP at 1550 nm excited by a 980 nm laser (F1550, 980Ex) is stable, generating a ratiometric F1550, 980Ex/F1050, 808Ex signal. (B) Schematic representation of the ratiometric fluorescent strategy for ALP detection based on NIR Ag₂S CQDs and calcine. (C) Schematic illustration of PEI-Ag₂S CQDs for heparin and heparinase I detection. Reproduced with permission from ref. 261. Copyright 2021 American Chemical Society. Reproduced with permission from ref. 264. Copyright 2019 Elsevier. Reproduced with permission from ref. 265. Copyright 2019 Elsevier.

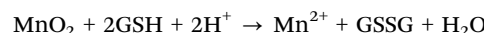
nanorods. Additionally, the presence of Pb²⁺ induced the *in situ* transformation of these nanorods into PbS CQDs, resulting in significant fluorescent changes and a notable increase in fluorescence quantum yield.²⁷¹

(III) Photothermal Therapy (PTT)/Photodynamic therapy (PDT)/Sonodynamic therapy (SDT). Photothermal therapy (PTT), a minimally invasive and potentially beneficial method, has sparked a lot of attention in recent years. It works by activating photosensitizing compounds with pulsed laser irradiation at near-infrared wavelengths to generate heat for the thermal melting of malignant tumors.²⁷⁶ The ability to reach deep tissue layers and the minimal impact of unselected cell death on healthy surrounding tissue are the primary advantages of photothermal therapy over traditional radiotherapy or chemotherapy.²⁷⁷ Besides, PDT is a light-based treatment approach that is clinically approved in which a PS is stimulated with a specific wavelength to generate reactive oxygen species (ROS) such as singlet oxygen (¹O₂) and promote a cytotoxic action to destroy tumor cells.²⁷⁸ A photosensitizer (PSs) should have large optical frequency absorption cross-sections, low toxicity, ease of functionalization, biocompatibility, and be readily soluble in organic solutions.²⁷⁹ However, photo-bleaching, poor solubility, instability, and quick removal of tiny organic PSs from the bloodstream are disadvantages of PTT and PDT clinical applications.²⁸⁰ As a result, in recent years, researchers have used CQDs as a delivery vehicle for the PS to perform PTT and PDT in cancerous cells. In continuation of this, Mahshid Hashemkhani *et al.* fabricated multitask hybrid nanoparticles

(NP) composed of bovine serum albumin (BSA) conjugated Ag₂S CQDs and MnO₂, loaded with 5-aminolevulinic acid (ALA) for NIR imaging-guided, improved PDT/PTT combination therapy of breast cancer. In this approach, Ag₂S CQDs provide NIR imaging and PTT, ALA acts as a pro-drug for PDT, and MnO₂ relieves hypoxia, catalyzes endogenous H₂O₂ to O₂ conversion, and produces hydroxyl radical and glutathione depletion at the tumor site (as shown below)



and



hence improving the PDT efficiency. They observed that the NPs effectively reduced cancer cell viability to 5–10% when exposed to two light wavelengths (640 nm and 808 nm), compared to when treated with PTT or PDT alone, which resulted in viability rates of 35–55%.²⁸¹ In a subsequent study led by Mahshid Hashemkhani *et al.* and his co-workers they synthesized cationic and anionic AgInS₂ (AIS) CQDs. They effectively loaded these AIS CQDs with ALA as a prodrug, demonstrating selective ALA release in acidic tumor environments. This improved tumor localization as well as ALA-induced photodynamic treatment (PDT). The PDT efficacy of the ALA-loaded AIS CQD data indicated that the phototoxicity of these ALA-loaded

AIS CQDs exceeded that of free ALA, drastically lowering cell viability in both 2D and 3D cell cultures. In the 3D spheroids, free ALA, cation, and anionic AIS CQDs reduced cell viability by 25–30%, 45–55%, and 55–60% respectively. The reduced cell viability is attributed to ROS generation and apoptotic/necrotic cell death.²⁸² The same group developed 2-mercaptopropionic acid capped Ag₂S quantum dots (AS-2MPA) which were later conjugated with endothelial growth factor receptor (EGFR)-targeting Cetuximab (Cet) and loaded with ALA or ALA/5-fluorouracil (5FU) for the targeted treatment of EGFR(+) colorectal cancer (CRC) through PDT (Fig. 25A). The study investigated various methods of loading ALA onto AS-2MPA CQDs, resulting in quicker release at acidic pH, which supports tumor microenvironment settings. In EGFR(+) CRC cells, particularly SW480 cells, the tailored therapy generated severe phototoxicity and was significantly more effective than free ALA. The combination of PDT with 5-fluorouracil (5FU) enhanced the therapeutic impact significantly because cell death is caused by the combined effect of 5FU *via* chemotherapy and effective ALA-to-PpIX conversion, which results in the formation of ROS.²⁸³ Moreover, they also produced aqueous colloidal Ag₂S CQDs capped with GSH for NIR image-guided photothermal therapy. At 795 nm, laser treatment of Ag₂S-GSH CQD solutions resulted in a dose and laser power (300 to 800 mW) dependent increase in solution temperature. *In vitro*, investigations revealed that laser treatment of Ag₂S-GSH CQD solutions at 795 nm resulted in a substantial reduction in cell viability in both HT29 and MCF7 cell lines, with the degree of cell death depending on the CQD dose and laser power. The photothermal conversion efficiency of the Ag₂S-GSH CQD at 7 mg mL⁻¹ was found to be 80% which is quite promising.²⁸⁴

Recently, another study led by Eda Celikbas *et al.* developed (GSH)-coated Ag₂S CQDs for combined PDT/PTT. They loaded brominated hemicyanine (Hemi-Br) onto Ag₂S CQDs with folic acid (FA) and glutathione (GSH) coatings, resulting in mitochondria-specific Ag₂S-GSH-FA/Hemi-Br nanoparticles. This system displayed 93% light-to-heat conversion efficiency and demonstrated enhanced phototoxicity when irradiated at 640 nm, indicating substantial PTT potential at this wavelength. In FR-positive HeLa cells, the viability of the HeLa cells decreased from 64% (free Hemi-Br) to 42% (Ag₂S-GSH-FA) to 25% (Ag₂S-GSH-FA/Hemi-Br) at a safe dosage. The steady decline in cell viability is due to the result of an increase in ROS production and temperature in cancer sites.²⁸⁵ Di Cui *et al.* designed bismuth (Bi) doped Ag₂S CQDs for fluorescence imaging-guided photothermal therapy in the second near-infrared region. Bi-doping in Ag₂S CQDs leads to an increase in the photothermal conversion efficiency to 58.9% from 34.5% (undoped one) which is evident in its photo-irradiated cell survival rate. After 10 minutes of irradiation with an 808 nm laser at a density of 1.2 W cm⁻², the survival rate of cancer cells was only 13%.²⁸⁶ Sonodynamic treatment (SDT), which applies particular ultrasonic frequencies to stimulate sonosensitizers inside tumors, is another therapeutic method to treat cancer. Reactive oxygen species (ROS) produced by this activation cause tumor cells to die using processes such as pyroptosis and sonoluminescence. SDT is a potential method for focused cancer treatment.²⁸⁷ Yuanyuan Zhang *et al.* constructed an integrated biomimetic nanoparticle using Ag₂S CQDs, amphiphilic polymers Pluronic F-127, and homologous adjuvant-functionalized cancer cell membrane for SDT therapy. Upon ultrasonic irradiation (SDT), these nanoparticles displayed

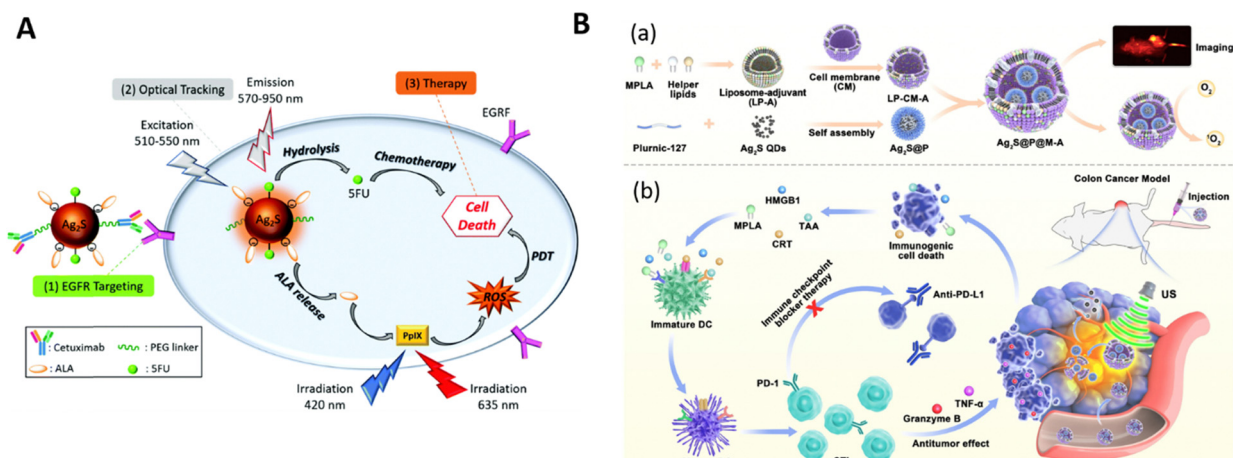


Fig. 25 (A) Schematic illustration of EGFR(+) targeting nanoparticles via combination of PDT/chemotherapy. (B) Schematic illustration of the synthesis route of integrated biomimetic nanocarriers Ag₂S@P@M-A with NIR-II imaging and ROS generation properties (a). Synergistic anticancer mechanism of the sonodynamic-immune combination therapy mediated by Ag₂S@P@M-A. Briefly, the nanoparticles are homologously targeted to the tumor through the cell membrane. Under sonodynamic therapy, ROS produced by sonosensitizer Ag₂S CQDs can induce immunogenic cell death. Dead cells subsequently release tumor-associated antigens (TAAs) and damage-associated molecular patterns (DAMPs). Meanwhile, the adjuvant PLA released from nanoparticles works together with DAMPs and TAAs to promote the maturation of DCs, thus activating cytotoxic T lymphocytes to secrete cytokines to exert antitumor effects. Combined with immune checkpoint blockers PD-L1 antibody, the antitumor effect of nanoparticles is further enhanced (b). Reproduced with permission from ref. 283. Copyright 2021 Royal Society of Chemistry. Reproduced with permission from ref. 288. Copyright 2023 Elsevier.

Table 7 Summary of CQD-based therapeutic system performance

Materials	Therapeutic process	Pro-drug/photosensitizer	Cell lines	Cell viability (%)	Ref.
Ag ₂ S CQDs	Combination of PDT/PTT	ALA	SKBR3 and MDA-MB-231	5–10	281
AgInS ₂ CQDs	PDT	ALA	HT29 and SW480	45 (HT29), 40 (SW480)	282
Ag ₂ S CQDs	PDT/chemotherapy	ALA and 5-FU	SW480 and HT29	18 (SW480), 32 (HT29)	283
Ag ₂ S CQDs	PTT	—	HT29	40	284
Ag ₂ S CQDs	Combination of PDT/PTT	Hemi-Br	HeLa	25	285
Ag ₂ S CQDs	PTT	—	HeLa	13	286
Ag ₂ S CQDs	SDT	—	CT-26 and HCT-116	—	288

targeted cancer cell delivery and triggered ROS generation leading to immunogenic cell death (ICD) (Fig. 25B).²⁸⁸ Simply put, the overall performance of the CQD-based therapeutic system, along with the cell lines and cell viability, is presented in Table 7.

(IV) Drug Delivery. Several nanoparticles (NPs) have been extensively studied for their potential in drug delivery applications, of which CQDs are just one type. The efficient trapping of anti-cancer medications in nanoparticles and their control over distribution in cells and tissue have been reported to enhance antitumor activity while reducing systemic side effects. There have been reports that the drawbacks of standard cancer therapy, such as multidrug resistance, lack of specificity, and cytotoxicity, can be overcome by using nanoparticles as drug delivery agents. The use of NPs as nanocarriers in cancer therapy is encouraged due to their unique benefits, which include improved stability, less toxicity, precision targeting, and biocompatibility.^{289,290} Due to their special qualities such as their unique optical characteristics resulting from quantum confinement effects CQD nanoparticles are being used extensively for targeted medication delivery. The inherent fluorescence of CQDs and their special ability to work as a multifunctional nanosystem make them a great option as well. This involves their capacity to support targeted medication administration and enhance the bioavailability and stability of medications by extending the *in vivo* circulation period and optimizing distribution.²⁹¹ CQDs must have their surface modified with target ligands (such as thioglycolic acid, polyethylene glycol (PEG), antibodies, DNA, biotin, or peptides) in order to be used for drug delivery.²⁹² Certain surface alterations allow the drug molecules to attach to the CQDs *via* electrostatic or covalent bonding, forming nano-drug carriers that subsequently produce luminous labels for the drug molecules in living things and cells. As a result, CQDs can track the distribution of drugs *in vivo* by serving as fluorescent probes and drug carriers.²⁹³ Recently, Ruixin Hao *et al.* constructed a targeted drug delivery system (DDS) based on hyaluronic acid (HA) modified lanthanum-doped zinc oxide (HA-La-ZnO) CQDs. They loaded anti-tumor drug Adriamycin (DOX) to HA-La-ZnO CQDs through covalent interactions and the formation of Zn²⁺-DOX. HA modification of CQDs enables them to bind specifically to receptor CD44. Moreover, PEGylation was used to stabilise the developed system under physiological conditions. Their results showed that lanthanum doping resulted in both an anti-tumor effect and dual fluorescence amplification.²⁹⁴ In another study, Fatma Demir Duman *et al.* utilized silver sulphide (Ag₂S) CQDs for drug delivery application. PEG was applied to the Ag₂S CQD surfaces, which

were then loaded with the anti-cancer medication 5-fluorouracil (5FU) and functionalized with Cetuximab (Cet) antibodies to pinpoint and expose tumour cells. With the use of low and high epidermal growth factor receptors (EGFR), the CQDs were created for targeted NIR imaging and lung cancer therapy. The A549 cells received 5FU from the Cet-conjugated CQDs in an efficient and targeted manner, resulting in a markedly increased level of apoptotic cell death. By comparison with the therapy of 5FU alone, they proposed that their innovative method will eliminate drug resistance drastically.²⁹⁵ In the same group, through electrostatic interaction between cationic Ag₂S CQDs and Doxorubicin (DOX), Fatma Demir Duman *et al.* loaded DOX into the CQDs which later on PEGylated with folic acid for elective delivery to cancer cells. They observed that the targeted delivery of DOX with these CQDs resulted in significantly higher toxicity to cancer cells, reducing the IC₅₀ value.²⁹⁶ For possible camptothecin (CPT) drug administration, Jose Varghese Rajendran *et al.* synthesized a new multifunctional system consisting of β-cyclodextrin (β-CDs) conjugated with CuInS₂/ZnS (CIS/ZnS) CQDs encased in gelatin-stabilized mesoporous silica SBA15. This method effectively improved the photostability and solubility of the medication. The drug release profile of the β-CD-conjugated Gel-SBA15-CIS/ZnS CQD nanocomposite was found to be acceptable, with 80% of the drug released over 9 hours, according to a triphasic model.²⁹⁷ Monika Ruzicka-Ayoush customized a targeted drug delivery system using Ag-In-Zn-S CQDs modified with various molecules, including folic acid (FA), for selective drug administration to adenocarcinomic human alveolar basal epithelial cells (A549). The achievement of the lowest half-maximal inhibitory concentration (IC₅₀) indicates the efficiency of the drug delivery system. The CQD-FA-DOX nanoconjugates revealed successful attachment of FA and doxorubicin (DOX), with considerable cytotoxicity against A549 cells.²⁹⁸ The summary of the performance of CQD-based drug delivery systems, including the types of drugs loaded and cell viability, is provided in Table 8.

Table 8 Summary of CQD-based nanoparticle for drug delivery application

Materials	Loaded drug	Cell lines	Cell viability (%)	Ref.
ZnO CQDs	DOX	B16F10	12	294
Ag ₂ S CQDs	5FU	A549	Close to 45	295
Ag ₂ S CQDs	DOX	HeLa, A549	Close to 10 (HeLa) Close to 25 (A549)	296
CuInS ₂ /ZnS CQDs	CPT	—	—	297
Ag-In-Zn-S CQDs	DOX	A549	—	298

(4) Photocatalysis. Since semiconductor CQDs are naturally strong at absorbing light, generating excitons, and transferring carriers, they are a popular choice for photocatalysis applications such as CO₂ photoreduction, hydrogen production, water splitting, organic pollutant degradation, N₂ fixation, and organic redox processes.^{299,300} The combined effects of these three sequential steps determine the overall photocatalytic efficiency: (i) after incident light excitation, the formation of charge carriers (electron–hole pairs) inside CQDs; (ii) charge separation and migration to the outer part of the CQDs; and (iii) reduction and oxidation reactions on active sites. When incident light's photon energy surpasses the band gap of CQDs (*i.e.*, the energy differential between the valence band maximum (VBM) and the conduction band minimum (CBM)), the electrons on the photocatalyst's VB can obtain sufficient energy to shift towards the CB, resulting in the formation of holes on the VB. The electrons and holes produced by photosynthesis then go to the outside. Recombination and the trapping of electrons and holes invariably accompany this process, lowering the system's efficiency. The surface composition and charge distribution of catalysts may be efficiently adjusted by surface-modifying CQDs with alternative ligands or appropriate cocatalysts, which enhances the activity of photocatalysts and increases the efficiency of photocatalytic reactions. Lastly, a photocatalytic reaction will occur thermodynamically if the energy level of holes (*i.e.*, VBM) is more positive than that of the oxidative reaction and the energy level of electrons (*i.e.*, CBM) is more negative than

the redox potential of the reductive process. In actuality, additional variables such as the reactions over potential on various catalytic sites have a significant impact on whether the reaction takes place or not. The CBM of CQDs, for instance, must be more negative than the redox potential of H⁺/H₂ (0 V against. NHE, pH 0), and the VBM needs to be more positive than the total of the redox potential of O₂/H₂O (1.23 V vs. NHE, pH 0) and the overpotentials for overall H₂O to divide into H₂ and O₂.^{301,302} Now, let us emphasize the recent advances of CQDs as a different photocatalyst.

(I) Photoredox organic transformation. The use of CQDs as photocatalysts for organic transformation like nitroamine reduction, alcohol oxidation, C–H functionalization, oxidation of sulfides and amines, *etc.* has been increasingly studied in recent years because it opens up new and efficient pathways to synthesize high-value-added chemicals.³⁰² Recently, Indra Narayan Chakraborty *et al.* demonstrated the efficient photocatalytic activity of CdSe CQDs in olefination reactions under visible-light irradiation at room temperature. They achieved an impressive 90% yield, which corresponds to a turnover number (TON) of 3913 and an internal quantum efficiency of 0.1% (Fig. 26A). They carried out CdSe photocatalyzed olefination reactions under mild base potassium carbonate (K₂CO₃). They suggested that the charge transfer mechanism behind the olefination is catalyzed by CQDs. The charge transfer from the CQD to the reactant was guided by triphenylphosphine,

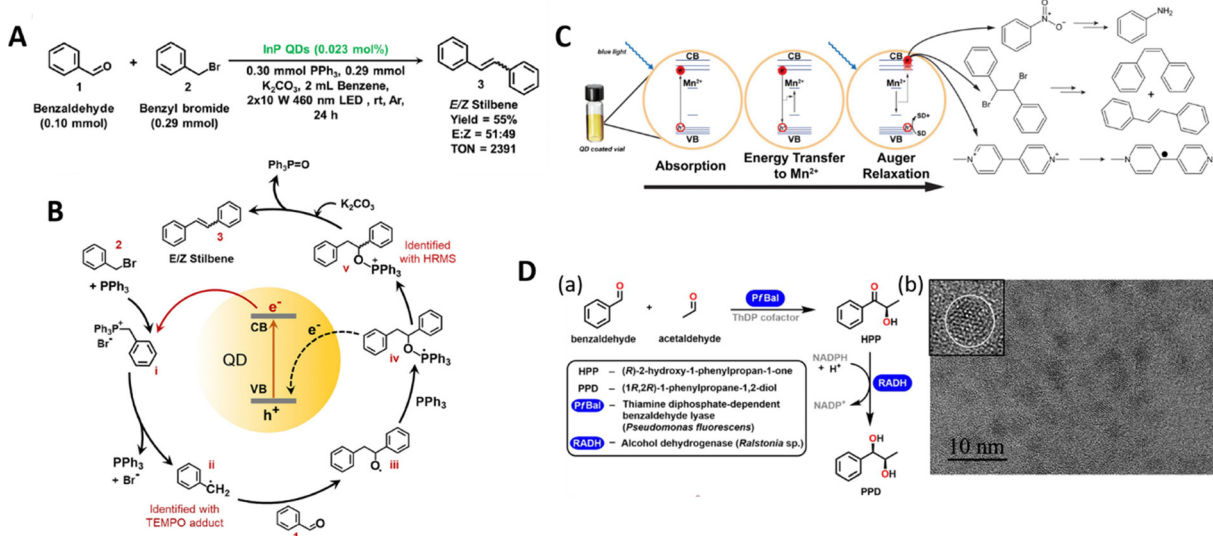


Fig. 26 (A) Reaction scheme and optimization studies for identifying the best reaction conditions for CdSe CQD photocatalyzed olefination between benzaldehyde and benzyl bromide. (B) Plausible photocatalytic cycle for the olefination reaction in the presence of CQDs. The surface passivating and nucleophilic properties of PPh₃ dictate the charge transfer process from the CQDs. The formation of benzylic radical and alkoxyphosphonium cation intermediates was confirmed using radical trapping and high-resolution mass spectroscopy (HRMS) experiments, respectively (represented in red highlights). (C) Mn²⁺-assisted Auger relaxation generates hot electrons that are to be harvested for photoreduction reactions. The electron and hole transfer to the organic substrate and sacrificial donor (SD), respectively. (D) Reaction scheme for individual Bal and coupled Bal-RADH activity. The coupled enzyme activity was monitored by NADPH consumption and the loss of its absorbance at 340 nm. The individual Bal and RADH enzyme activities were monitored as described in text (a). High-resolution TEM micrograph of the 523-nm-emitting CdSe/CdS/ZnS core/shell/shell CQDs with an average diameter of 4.1 ± 0.5 nm as measured from TEM analysis of over 200 representative CQDs in micrographs (b). Reproduced with permission from ref. 303. Copyright 2023 American Chemical Society. Reproduced with permission from ref. 305. Copyright 2022 Royal Society of Chemistry. Reproduced with permission from ref. 306. Copyright 2022 American Chemical Society.

which also served as a nucleophile and surface passivating agent. By producing benzylic radicals that combined with ketone or aldehyde, the benzyl triphenylphosphonium bromide salt catalyzed olefination processes by accepting electrons from photoexcited CQDs. This process, which was used on formaldehyde as a model, produced styrene, a terminal alkene of industrial significance (Fig. 26B). Additionally, photocatalytic olefination under moderate circumstances was achieved using the eco-friendly indium phosphide (InP) CQDs, demonstrating the usefulness of this method. Their research therefore offered a productive way to use room-temperature visible light and CQDs to efficiently introduce double bonds into organic compounds.³⁰³ Using CdSeS/CdZnSeS(Al)/ZnS CQDs as catalysts, Yu-Yun Yin *et al.* developed a photocatalyzed three-component reaction combining malononitrile, benzaldehyde, and *N,N*-dimethylaniline that resulted in the production of α -aminobutyronitrile molecules through C–C bond formation. The well-dispersed CQD catalysts exhibited remarkable catalytic activity and stability, with a maximum quantum yield of 98% and a turnover number (TON) above 1.1×10^3 . In this reaction, *N,N*-dimethylanilines were effectively converted into α -aminoalkyl radicals, which then took part in radical addition reactions with the *in situ* generated electron-deficient alkene benzylidene malononitrile. With the help of this procedure, they synthesized a series of γ -amino nitriles.³⁰⁴ Brian Malile *et al.* developed Mn²⁺-doped CdS/ZnS core/shell CQDs (denoted as Mn:CdS/ZnS or doped CQDs) as photoredox catalysts for model organic reactions including the photoreduction of methyl viologen, dehalogenation of meso-1,2-dibromo-1,2-diphenylethane, and the photoreduction of nitrobenzene to aniline (Fig. 26C). The incorporation of Mn²⁺ ions into CdS nanocrystals enhanced the photoreduction efficiency by promoting Auger cross-relaxation, yielding hot electrons with high reducing power. They observed several key points. First, as compared to CdS CQDs, Mn:CdS/ZnS CQDs showed a 3.4-fold increase in the photoreduction of methyl viologen. Second, in biphasic processes like the photoreduction of meso-stilbene dibromide, the viologen may be employed as an electron shuttle, providing flexible design in cases where the reactants and photocatalysts are not the same. Third, Mn:CdS/ZnS CQDs with an overall internal quantum efficiency of about 3% photocatalyzed the 6-electron reduction of nitrobenzene to aniline. Remarkably, the photoreduction of nitrobenzene was accomplished in 15 minutes using doped CQDs as opposed to more than 48 hours by undoped CQDs – a >190-fold increase.³⁰⁵ To improve enzymatic catalysis, Shelby Hooe *et al.* explored the immobilization of benzaldehyde lyase (Bal) on CdSe/CdS/ZnS core/shell/shell CQDs. The catalytic rate (k_{cat}) of the constructed Bal-CQD system increased by approximately 30%, and its enzymatic efficiency (k_{cat}/K_M) increased by more than three times. Alcohol dehydrogenase (RADH) and linked enzymes efficiently converted acetaldehyde and benzaldehyde to (1*R*,2*R*)-1-phenylpropane-1,2-diol, an important precursor of the medication diltiazem, when mixed within self-assembled CQD nanoaggregates (Fig. 26D). Despite large discrepancies in catalytic speeds and Michaelis constants (K_M) between the two enzymes, the channelling of the (1*R*)-2-hydroxy-1-phenylpropan-1-one intermediate was verified by an approximately 50% increase in the coupled

enzymatic flow.³⁰⁶ Using colloidal CdSe CQDs coated with molecular energy shuttles (polyaromatic compounds tethered to CQDs), Yishu Jiang *et al.* catalyzed intermolecular [2+2] photocycloadditions of freely diffusing olefinic substrates under visible light. To extend CQD-photocatalyzed reactions to substrates without anchoring groups, the shuttles served as noncovalent adsorption sites for substrates on the CQD surface. With a yield of up to 94%, the CQD-shuttle complexes induced both homo- and hetero-intermolecular [2+2] photocycloadditions. Remarkably, the yields were comparable to those achieved with the traditional photosensitizer Ir(ppy)₃ but with improved stability, reduced catalyst loading, and the capacity to recover and reutilize the catalyst for several cycles of the process using straightforward centrifugation. The photocatalysis mechanism involved a two-step triplet-triplet energy transfer process, with energy transfer from the CQD to the shuttle followed by a second energy transfer from the shuttle to the transiently adsorbed substrate.³⁰⁷ Yuxin Liu *et al.* constructed a photocatalytic system employing CdS@Cd_xZn_{1-x}S@ZnS gradient alloyed CQDs as photocatalysts and different acids as proton donors to selectively cleave β -O-4 bonds in lignin *via* the proton-coupled electron transfer (PCET) mechanism. As opposed to single binary CQDs, the gradient alloyed CQDs capped with short ligand mercaptopropionic acid demonstrated a broad absorbance range, quick transfer of photogenerated carriers, and improved redox activity. Significantly more catalytic activity was produced as a result of this improvement, with yields of up to 70% and 65% for the aromatic compounds phenol and acetophenone, respectively. The mechanism of PCET comprised the production of a C _{α} radical from the ketone intermediate with the aid of an acid that possessed an appropriate bond dissociation-free energy (BDFE) and strongly encouraged electronic transmission.³⁰⁸

Moreover, Julianna M. Mouat *et al.* explored CdS CQDs as robust photocatalysts for Ni-mediated cross-electrophile coupling in synthetic photo-redox catalysis. They observed the maximum catalytic transformation (turnover number (TON) up to 40 000 for 5.7 nm size CdS CQDs).³⁰⁹ The ability of CdS CQDs with moderate organic reductants and visible light (450 nm) to function as effective photoreductants for a range of organic transformations that need potent reducing agents was shown by Jonas K. Widness *et al.* By utilizing Auger recombination, a photophysical process that is known to occur in photoexcited anionic CQDs, strong photoreductive capabilities of CdS CQDs allowed for the cleavage of phosphate esters and aryl chlorides by utilising energy from two successive photoexcitations (Fig. 27). Under the influence of blue LED irradiation and sacrificial amine reductants, stable CdS CQDs were able to produce hydrodefunctionalized or functionalized products by photoreduction cleavage of aryl chlorides and phosphate esters, with reduction potentials as high as -3.4 V in comparison to the saturated calomel electrode (SCE). With an astounding turnover number of up to 47 500, stable CQDs perform better than small-molecule catalysts. Furthermore, the system was found to catalyse the reduction of complicated compounds, including the removal of the tosylate protecting group, the debenzylation of cyclopropane carboxylic acid derivatives, and the reductive ring opening of these compounds.³¹⁰

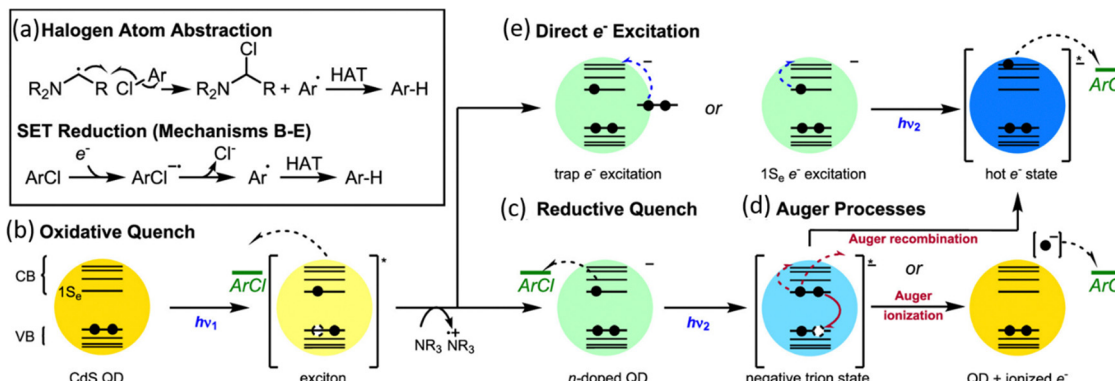


Fig. 27 Mechanistic possibilities for aryl chloride reduction. Halogen atom abstraction by organic radicals derived from the reductant (a). Reduction of substrate by a neutral excited CQD (b). Reduction of substrate by a ground-state anionic CQD after reductive quenching (c). Reduction of substrate by hot or ionized electron generated via Auger processes of a negative trion state (d). Reduction of the substrate by a hot electron generated via direct excitation of electrons in the $1S_e$ state or surface “trap states” (e). Reproduced with permission from ref. 310. Copyright 2022 American Chemical Society.

On a different note, Ting-Ting Zhao *et al.* loaded CdSe/CdS core-shell CQDs onto the surface of titanium dioxide nanotubes (TNTs) to create CQD/TNT composite photocatalysts. Excellent catalytic activity was shown by the resultant composites in the cyclization process between arylamines and different aldehydes, which produced matching N-heterocyclic compounds.³¹¹ Low-toxic ZnSe/ZnS core-shell CQDs were used by Chengming Nie *et al.* as efficient photocatalysts for challenging organic transformations. The surfaces of CQDs were functionalized with benzophenone (BP) ligands to enhance their excited-state energy and photo-redox power. These ligands induced long-lived charge-separated states by quickly removing electrons from photoexcited CQDs. The dehalogenation of aryl chlorides and the additive-free polymerization of acrylates were made possible by the strong electron-relaying properties of the benzophenone anions. On the other hand, by functionalizing the CQDs with biphenyl ligands (BIP), energy was stored in long-lived, energetic triplets, which made it easier to cycloadditionally react carbonyls with alkenes and homo-cyclo-additionally react styrene [2+2]. Under blue-light stimulation, the CQD-BP system showed reductive dehalogenation and polymerization, while the CQD-BIP triplet-sensitization system produced high triplet-energy cycloadditions.³¹² To conclude, Table 9 presents the performance of CQD-based nanoplatforms in

photoredox organic transformation photocatalysis, including the effective values of Turn-Over Number (TON), conversion yield (%), and internal quantum efficiency (%).

(II) H_2 Production. As mentioned earlier the photogenerated e^- at the semiconductor's CB can carry out the reduction process of reducing water's H^+ to become H_2 , while the h^+ at the VB location can take part in the water oxidation reaction to produce O_2 in a typical photocatalytic water splitting reaction. However, it is challenging to achieve photocatalytic total H_2O splitting into H_2 and O_2 , as it is a typical uphill reaction that needs a significant increase in Gibbs free energy ($\Delta G^\circ = 237 \text{ kJ mol}^{-1}$).^{300,301} However, the creation of CQD-based heterojunctions has shown to be a viable approach for achieving extremely effective photocatalytic H_2 evolution reaction (HER) as summarized in Table 10. Stefan Benndorf *et al.* constructed a hybrid photocatalytic system for hydrogen production by combining CdSe CQDs with [FeFe] hydrogenase mimics in a thin-film architecture. The covalent binding of [FeFe] hydrogenase mimics to CQD surfaces *via* carboxylate groups allowed for close interaction between the catalyst and light-harvesting CQDs, which enhanced electron transport and promoted hydrogen evolution. The functionalized thin film showed turnover values in the 130–160 (long linkers) and 360–580 (short linkers) range.³¹³ In a different effort, Hao Yu

Table 9 Summary of CQD catalyzed photoredox organic transformations

Materials	TON	Product yield (%)	Internal quantum efficiency (%)	Ref.
CdSe CQDs	3913	90	0.1	303
InP CQDs	2391	55	—	
CdSeS/CdZnSeS (Al)/ZnS CQDs	1100	98		304
CdS/ZnS CQDs	—	100 (DDE)	2.9 (MV^{2+}) ~3 (nitrobenzene reduction)	305
CdSe/CdS/ZnS CQDs	—	—	>3 fold increase	306
CdSe CQDs	—	Up to 94	—	307
CdS/CdZnS/ZnS CQDs	—	Up to 70 (phenol), 65 (acetophenone)	—	308
CdS CQDs	Up to 40 000	79	—	309
CdS CQDs	Up to 47 500	95	—	310
CdSe/CdS CQDs	—	81	—	311
ZnSe/ZnS CQDs	—	95	—	312

Table 10 Summary of H₂ production by CQD-based systems

Materials	TON	H ₂ production rate	Ref.
CdSe CQDs	130–160 (long linkers) and 360–580 (short linkers)	—	313
AgInS ₂ CQDs	—	9.79 mmol g ⁻¹ h ⁻¹	314
CdSe CQDs	—	6.48 mmol g ⁻¹ h ⁻¹	315
CdSe/CdS CQDs	—	0.54 mL h ⁻¹	316
AgIn ₅ S ₈ /CdS CQDs	—	12.74 mmol g ⁻¹ h ⁻¹	317
AgInS CQDs	—	62.3 μmol g ⁻¹ h ⁻¹	318
CdS/ZnS CQDs	—	9.77 ± 0.37 μmol g ⁻¹ h ⁻¹ (bare CQDs), 4.97 ± 0.28 mmol g ⁻¹ h ⁻¹ (CQDs-Au _{1.6}), 4.16 ± 0.11 mmol g ⁻¹ h ⁻¹ (CQDs-Au _{2.2})	319
InP/ZnS CQDs	310 000 per CQDs	3.49 ± 0.38 mmol g ⁻¹ h ⁻¹ (CQDs-Au _{3.3})	320
PdS CQDs	—	102.04 μmol mg ⁻¹ h ⁻¹	321
Cu _x Ag _{1-x} InS ₂ /ZnS CQDs	—	46.1 mmol g ⁻¹ h ⁻¹ 67.4 μmol cm ⁻² h ⁻¹	322

et al. followed a coordination-assisted self-assembly method to design a nanocomposite by encapsulating AgInS₂ CQDs into metal-organic frameworks (MOFs), forming AgInS₂@ZIF-8/ZnS nanostructures. After six hours of sulfurization, the resultant nanocomposites showed exceptional photocatalytic activity, with an average hydrogen production of 9.79 mmol g⁻¹ h⁻¹, which was over ten times more hydrogen than when using AgInS₂ CQDs. The following factors have been suspected of contributing to the increased photocatalytic activity: the formation of a close heterostructure that prevents CQDs agglomeration and nanocomposite photo corrosion; the introduction of AgInS₂ CQDs to narrow the ZIF-8 band gap improves visible light absorption and increased charge separation; and the formation of interfacial Zn-S bonds between ZIF-8 and AgInS₂ CQDs, which facilitates electron transfer and enables efficient carrier separation.³¹⁴ Meng Chen *et al.* modified CdSe CQDs using a Co-encapsulated N-doped carbon (Co@NC) catalyst that was made by pyrolyzing a ZIF-8@ZIF-67 to photocatalytically reduce Cr(vi) and split water. The resultant Co@NC/CdSe photocatalyst showed dramatically improved separation, photogenerated charge carrier transfer, and light absorption characteristics. With no sacrificial agents needed, the ideal 2% Co@NC/CdSe performed admirably, attaining a high Cr(vi) reduction rate constant of 0.28 min⁻¹ and a noteworthy H₂ evolution rate of 6.48 mmol g⁻¹ h⁻¹ in a 10% lactic acid solution. It was determined that H₂O₂ and electrons were the active species for Cr(vi) reduction. With a 45-minute reduction time of 99.0% Cr(vi) and a notable rate of H₂ generation, the optimised catalyst demonstrated exceptional efficiency in water splitting.³¹⁵ Sub-monolayer ZnSe partial-shell coated CdSe/CdS core/shell CQDs were synthesised by Ping Wang *et al.* as a model catalyst for H₂ photogeneration under light illumination (Fig. 28A). Through the acceleration of hole migration during the H₂ photogeneration process and the retardation of photo-generated electron transfer, the development of the ZnSe partial-shell might modify and optimise the photocatalytic performance. In comparison to the host CdSe/CdS CQDs, coating 0.18 monolayers (ML) of the ZnSe shell onto CdSe/CdS CQDs increased the catalytic performance for H₂ photogeneration by 50.0%, according to experimental findings and theoretical calculations. Nevertheless, the performance decreased as further ZnSe partial-shell coating increased.³¹⁶ In order to facilitate effective solar-driven

hydrogen sulphide (H₂S) splitting as a hydrogen source for H₂ generation, Anqiang Jiang *et al.* proposed a design technique for improving charge carrier separation and transfer efficiency in CQDs. They produced AgIn₅S₈/CdS (AIS/CdS) CQDs with a Type-II core/shell and a short-chain inorganic sulfide ion (S²⁻) ligand. Fast charge carrier extraction and electron transmission were encouraged by this dual charge-accepting engineering. The photocatalytic activity was improved synergistically by the added S²⁻ ligand and shell, resulting in a hydrogen evolution rate of 12.74 mmol g⁻¹ h⁻¹, which is more than four times greater than the pristine AIS core. Charge recombination was efficiently reduced and hole transfer was expedited by the dual charge-accepting structure that is presented in Fig. 28B. Rapid electron injection into the CdS shell was detected by transient absorption spectroscopy in less than 1.7 ps.³¹⁷ Jiahe Song *et al.* concentrated on using Ag-In sulphide CQDs (AIS QDs) *via* an *in situ* growing approach to increase the photocatalytic activity of nonmetallic polymer g-C₃N₄ (GCN) for the breakdown of water contaminants and hydrogen generation. When compared to pure GCN, the synthesised AIS-CQDs/GCN nanocomposite performed better in terms of photocatalysis, especially when 10% of the nanocomposite contained AIS CQDs. In just one hour of exposure to visible light, it was able to degrade tetracycline with an efficiency of 48.5% (3.2 times higher than that of GCN) and demonstrate a noteworthy hydrogen evolution rate of 62.3 μmol g⁻¹ h⁻¹ (bare GCN exhibited insignificant activity). The enhancement was ascribed to the creation of a Type-II heterojunction inside the composite catalyst supported by TRPL spectra (Fig. 28C), which widened the light absorption range, sped up charge transfer, and decreased carrier pair recombination.³¹⁸ The catalytic activity of Type-I CdS/ZnS core/shell CQDs was increased by Jin *et al.* by adding metallic Au domains to the CQD surface. When compared to bare CdS/ZnS CQDs, the resultant CdS/ZnS CQD-Au host-satellite-type hybrid nanocrystals (HNCs) showed a 400-fold increase in photocatalytic hydrogen evolution rate (HER). The 1.6–3.3 nm-sized Au domains were essential in enabling electron extraction and transport to molecules that could take electrons. Ultrafast sub-picosecond charge separation was found in the CQD-Au HNCs by transient absorption spectroscopy, which may have contributed to their higher catalytic efficiency. Density functional theory calculations suggested that an intermediate

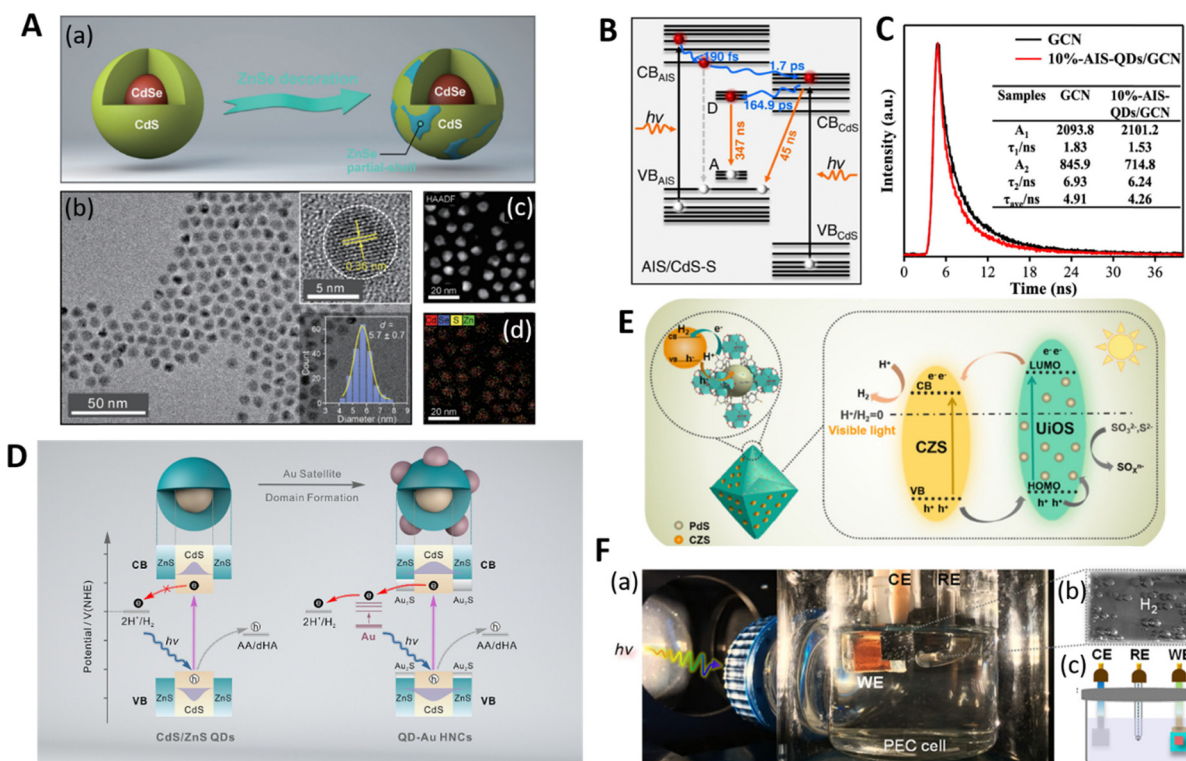


Fig. 28 (A) Schematic illustration of the growth of a ZnSe partial shell onto the host CdSe/CdS core/shell CQDs (a). TEM and HRTEM images (inset) and size distribution histogram (inset) of CdSe/CdS/ZnSeL core/shell CQDs (b). The corresponding overlapping elemental mapping of Cd, Se, S, and Zn, respectively. (B) An illustration of the carrier relaxation process in AIS/CdS-S CQDs. Electrons transition from a more highly excited state to the conduction band edge, and then from the band edge to the conduction band of CdS and finally to the antisite state. Recombination primarily occurs via a donor–acceptor pair of AIS and valence band levels of the CdS shell to AIS valence band levels. (C) TRPL spectra of GCN and 10%-AIS-QDs/GCN. (D) Schematic illustration of the photocatalytic mechanism for the CQD-Au HNCs compared with the Type-I CdS/ZnS Core/Shell CQD counterpart (dHA indicates dehydroascorbic acid). (E) Schematic description of photocatalytic H₂ production by the PdS@UiOS@CZS catalyst. (F) Photograph of Cu_xAg_{1-x}InS₂/ZnS CQD-sensitized PEC cells (a). Photograph of the Pt counter electrode (b). Scheme (c) of Cu_xAg_{1-x}InS₂/ZnS CQD-sensitized PEC cells. Reproduced with permission from ref. 316. Copyright 2022 Springer Nature. Reproduced with permission from ref. 317. Copyright 2023 Elsevier. Reproduced with permission from ref. 318. Copyright 2023 American Chemical Society. Reproduced with permission from ref. 319. Copyright 2023 American Chemical Society. Reproduced with permission from ref. 321. Copyright 2022 American Chemical Society. Reproduced with permission from ref. 322. Copyright 2022 American Chemical Society.

Au₂S layer developed at the semiconductor–metal interface, reducing the energy barrier that the ZnS shell imposed. The catalytic mechanism involved the rapid separation of photogenerated electrons and holes; holes were scavenged by ascorbic acid (AA) and effectively collected by Au domains for future hydrogen production (Fig. 28D). The negative association between the size of the Au domains and HER efficiency demonstrated the importance of domain size in charge recombination and Fermi level shifting.³¹⁹ Rong-Jin Huang *et al.* investigated the photocatalytic performance of InP-based CQDs for hydrogen evolution by employing controlled anion exchange to build an S_x-In-P_{1-x} buffer monolayer between the InP core and ZnS shell. The buffer layer not only minimised misfit dislocation and lattice mismatch, but also made effective charge separation easier. Efficient exciton tunnelling was made possible by the production of a thin ZnS shell by anion exchange using low-reactivity S precursors. The resultant InP/InPS/ZnS core/buffer/shell (CBS) CQDs showed remarkable photocatalytic activity, generating hydrogen within 16 hours of irradiation at a rate of 102.04 μmol mg⁻¹ h⁻¹, with

a turnover number (TON) reaching 310 000 per CQDs. The rate was approximately 77 times greater than the initial InP CQDs at the same concentration. The possible photocatalytic mechanism of InP/InPS/ZnS CBS CQDs has been suggested to work as follows: after absorbing visible light, the CBS CQDs produced electron–hole pairs in the valence and conduction bands of the core InP CQDs. Next, the ZnS shell and buffer layer were tunnelled to the surface of CQDs by the photogenerated electrons and holes. Additionally, photogenerated electrons worked with Ni cocatalysts to convert protons to H₂. Numerous variables affected the total photocatalytic H₂ evolution activity. First, using Ni cocatalysts to help passivate defects in the original InP CQDs, the coating of the S_x-In-P_{1-x} buffer layer and ZnS shell had a good effect on H₂ evolution by reducing unwanted charge recombination at trap sites. Furthermore, the S_x-In-P_{1-x} buffer layer removed interfacial defect sites between the InP core and ZnS shell by reducing lattice mismatch. The delocalization of excitons to the buffer layer helped in the tunnelling out of the CQDs, and the alloyed interface promoted the spread of the radial probability density for

electrons and holes. As a result, the photocatalytic activity of InP CQDs significantly improved a lot. In addition, the protective function of the ZnS shell enhanced stability.³²⁰ Siman Mao *et al.* synthesised the photocatalyst PdS@UiOS@CZS by encasing PdS CQDs in thiol-functionalized UiO-66 (UiOS), a metal–organic framework (MOF), and locking Cd_{0.5}Zn_{0.5}S (CZS) solid solution nanoparticles (NPs) on its exterior. Under visible light irradiation, the optimised PdS@UiOS@CZS photocatalyst demonstrated an impressive hydrogen (H₂) evolution rate of 46.1 mmol g⁻¹ h⁻¹, outperforming pure UiOS, CZS, and UiOS@CZS by 512.0, 9.2, and 5.9 times, respectively. The exterior surface of the encapsulation structure, which included Cd_{0.5}Zn_{0.5}S NPs, allowed electron–hole pairs to migrate and separate quickly. PdS CQDs in UiOS pores functioned as hole traps, successfully preventing the recombination of photogenerated electrons and holes, which improved photocatalytic hydrogen evolution (Fig. 28E). UiOS served as a medium for charge transfer.³²¹ Heng Guo *et al.* improved the photo-electrocatalytic efficiency of heavy metal-free Cu_xAg_{1-x}InS₂/ZnS CQDs for solar-powered hydrogen generation (Fig. 28F). The energy band structure was optimised by the use of Cu ion doping and ZnS shell-assisted defect passivation, which enhanced charge separation and stability in photoelectrochemical devices. With adjustable Cu doping levels, the resultant Cu_xAg_{1-x}InS₂/ZnS CQDs demonstrated improved interfacial charge separation and transfer, attaining a saturated photocurrent density of 5.8 mA cm⁻² at 0.8 V about the reversible hydrogen electrode. The maximum H₂

generation rate by Cu_{0.5}Ag_{0.5}InS₂/ZnS CQDs was found to be 67.4 μmol cm⁻² h⁻¹. Utilising defect passivation in conjunction with this planned Cu doping approach, the photo-electrocatalytic activities of the CQDs were optimised for solar-powered hydrogen production.³²²

(III) Organic dyes and pollutant degradation. These days, as the population grows, one of the main problems is water contamination. Unpurified industrial waste flows into the water supply in enormous quantities. Water supplies get polluted as a result of contaminants and dyes that are bad for the environment. CQDs are frequently used as photocatalysts to eliminate these pollutants and dyes *via* sustainable and renewable energy sources. Recently, Debasish Borah *et al.* synthesised CdS CQDs by using an aqueous extract of the cyanobacterium *Nostoc corneum* as a particle stabilising agent. As-synthesised CdS CQDs mediated by *Nostoc corneum* showed effective catalytic activity, with a high conversion yield of around 90% for the degradation of the water-soluble dyes, methyl orange (MO) and rhodamine B (RhB) (Fig. 29A). For MO and RhB, the photocatalytic degradation had rate constants of 0.02896 and 0.02846 min⁻¹, respectively, indicating pseudo-first-order kinetics. The reduction of dissolved oxygen (O₂) and the interaction of the hole (h⁺) in the VB of CdS CQDs with the adsorbed water molecules on the surface of CQDs, respectively, resulted in the creation of the superoxide radical (O₂^{•-}) and hydroxyl radical (•OH), which were engaged in the

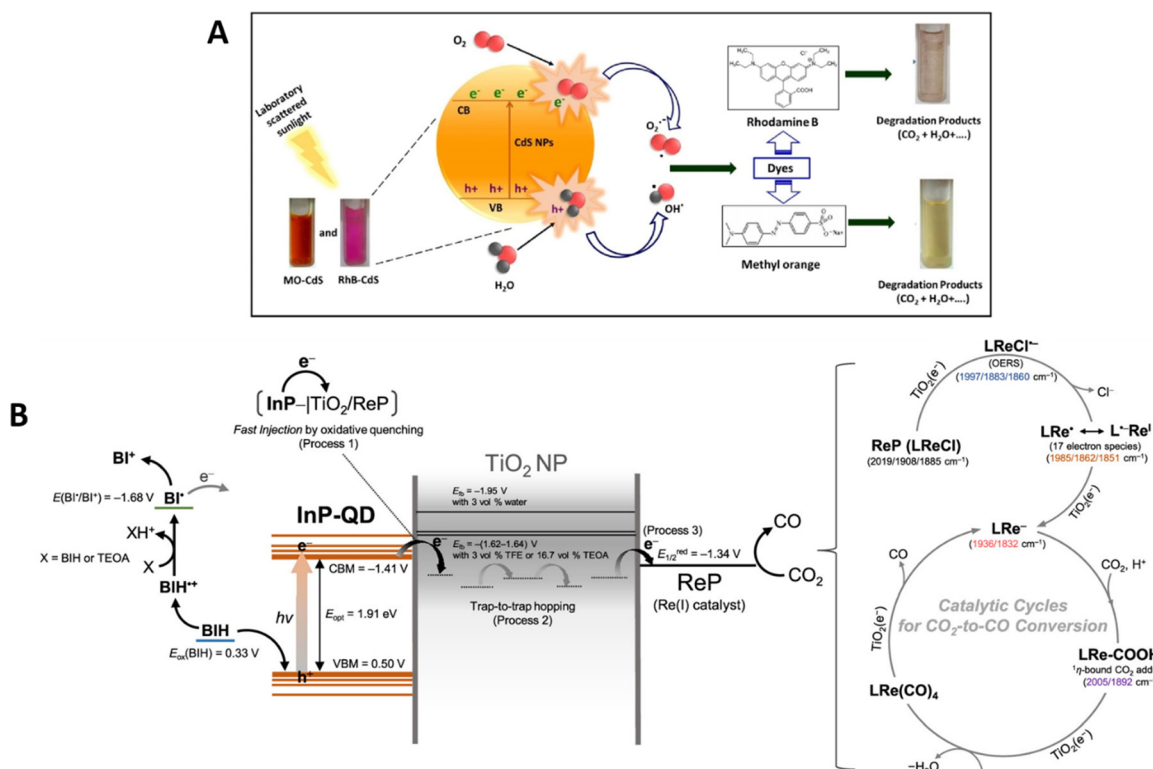


Fig. 29 (A) Representations of photocatalytic degradation of RhB and MO dye using CdS CQDs under laboratory scattered sunlight. (B) Schematic of the electron transfer processes in the InP-CQD-sensitized ternary hybrid system with the relative energy levels (V vs. SCE) of components and the electron donation process of BIH during photocatalysis. Reproduced with permission from ref. 323. Copyright 2023 Springer Nature. Reproduced with permission from ref. 336. Copyright 2022 American Chemical Society.

catalytic reaction mechanism. The organic dye molecules were broken down by these radicals into inorganic byproducts like carbon dioxide (CO_2) and harmless water (H_2O). Furthermore, when tested against specific pathogenic bacterial strains, the CdS CQDs showed notable antibacterial activity.³²³ Tahir Iqbal *et al.* synthesized carbon nanodot (CND) modified CuS CQDs for enhanced photocatalytic activity in the degradation of Panadol in wastewater. CuS CQD–CND composites were produced in two quantities, 2% and 4%. The 4% CuS CQDs–CNDs outperformed pure CuS CQDs and 2% CuS CQDs–CNDs in photocatalytic activity due to their reduced band gap energy and greater transient photocurrent density. The effectiveness of 2% CuS CQDs–CNDs in degrading Panadol was 87.9%, but 4% CuS CQDs–CNDs demonstrated an astounding 96.5% drug elimination from water. Under visible light irradiation, the synergistic action of CuS CQDs and CNDs enhanced photo-generated charge transfers, promoting Panadol degradation.³²⁴ Maroua Mrad *et al.* made heterostructured photocatalysts by fusing quaternary Ag–In–Zn–S (AIZS) CQDs with ZnO nanorods (NRs). ZnO/AIZS catalysts were subsequently manufactured using a sonication-assisted deposition technique and heat treatment. The ZnO/AIZS(10) catalyst with 10wt% AIZS CQDs showed the maximum photocatalytic activity for Acid Orange 7 (AO7) dye degradation under visible light. The better performance of the ZnO/AIZS(10) photocatalyst was attributed to its increased charge separation and greater absorption of visible light. It was able to degrade 98% of AO7 in 90 minutes, whereas ZnO NRs could only break down 11% of the dye. Additionally, this catalyst showed stability across eight reuse cycles with little to no activity loss.³²⁵ To overcome the low photocatalytic activity of polyimide, Qian Liu *et al.* effectively created porous polyimide/carbon nanodot/ZnS quantum dot material aerogels using the supercritical fluid drying method. The resultant aerogels have a porous network structure and a large surface area. While ZnS CQDs changed the valence band, conduction band edge, and band gap edge of polyimide aerogels, the addition of CNDs improved the material's ability to absorb visible light. The separation of photoexcited electrons and holes was made easier by enhanced charge transfer provided by both CNDs and ZnS CQDs. When compared to pure polyimide aerogel, the visible-light photocatalytic performance for the breakdown of oxytetracycline jumped considerably. The essential functions of $\text{O}_2^{\bullet-}$ and h^+ species were involved in the suggested photocatalytic degradation pathway. They discovered that the photocatalytic rate of the synthesised PI/CQDs/ZnS-1 aerogel was 1.5 times higher than that of the pure aerogel.³²⁶ A novel strategy was employed by Yuting Gu *et al.*, utilizing Co-ZnS CQDs for peroxymonosulfate (PMS) activation in water treatment. Using a water phase coprecipitation technique, surface sulphur vacancies (SVs) were introduced into the Co-ZnS CQDs by lattice-doping Co for Zn. As a result, the surface became electron-rich/poor, greatly increasing PMS activation efficiency. Because of the special surface modulation, the system was able to rapidly degrade plasticizer micropollutants in a matter of seconds. The interfacial reaction mechanism included internal electrons being transferred to surface SVs by contaminants adhering to cobalt metal sites as electron donors. In addition, PMS adsorbed on SVs was

simultaneously converted to radicals, allowing for efficient electron recovery. Pollutant degradation was further aided by the attraction of dissolved oxygen molecules to catalyst defect.³²⁷ In another study, for the degradation of organic pollutants, Peiqing Sun *et al.* designed a photosynthetic biohybrid system comprised of Ag_2S CQDs functionalized with *E. coli* cells. When it comes to the photocatalytic destruction of organic contaminants, the biohybrid system performed better. The biohybrid system's increased photocatalytic activity was ascribed to the efficient separation and transfer of photogenerated charges by Ag_2S CQDs. The photocatalytic mechanism revealed photogenerated reactive oxygen species ($\text{O}_2^{\bullet-}$) were the main reactive species that break down organic contaminants when exposed to visible light.³²⁸ Farzad Farahmandzadeh *et al.* employed CdS CQDs as a catalyst to break down dyes in water and as a means of concurrently detecting Pb^{2+} ions. When Pb^{2+} ions were present, the fluorescence intensity of CdS CQDs progressively dropped until it reached full quenching at 100 μM lead ions. Excellent photocatalytic activity was found when CdS CQDs were tested under UV and daylight conditions using pollutant dyes such as methylene blue (MB), methylene orange (MO), and rhodamine B (RhB). In particular, 94.9% of MO, 94.4% of RhB, and 81.2% of MB were destroyed following 60 minutes of UV irradiation. Radical scavenger tests revealed that holes were essential to understanding the critical parameters in the photodegradation process of MO by CdS CQDs under UV light. The CdS CQD-based fluorescence sensor exhibited a linear relationship between Pb^{2+} concentration and fluorescence intensity, with a detection limit of 60 nm.³²⁹ By successively hydrothermally synthesising zero-dimensional (0D) CdSe (CE) CQDs anchored on two-dimensional (2D) $\text{HSr}_2\text{Nb}_3\text{O}_{10}$ nanosheets (HSNO-ns) with the aid of microwave heating, Yibin Chen *et al.* were able to effectively construct a unique CdSe/HSr₂Nb₃O₁₀ n-n heterojunction. Methyl orange (MO) photodegradation was used to assess the system's photocatalytic performance, and photocurrent and PL curves were used to examine the influence of n-n heterojunctions on the mechanism behind the increased photocatalytic activity. The CE50/HSNO-ns photocatalyst showed the best photo-degradation efficiency when compared to pure CE-CQDs and HSNO-ns. Under visible light irradiation ($\lambda > 420 \text{ nm}$), it degraded MO solution (25 mg L⁻¹). For instance, the photocatalyst surpassed single HSNO-ns and CE-CQDs by 193.7 and 4.9 times, respectively, demonstrating the greatest photocatalytic performance. The significant augmentation of optical absorption and the efficient separation of photo-induced electron–hole pairs resulting from the n-n heterojunction formed by CE-CQDs and HSNO-ns were responsible for the significant improvement in photocatalytic performance.³³⁰ The potential of CQDs as a catalyst for dye degradation and as a photo-redox catalyst was recently investigated by Zhiyuan Huang *et al.* They successfully prepared Pickering emulsions with amphiphilic PbS CQDs. Amphiphilic PbS CQDs were synthesized by constructing Janus-ligand shells using lipophilic oleic acid (OA) and hydrophilic 4-(2,2-dicyanovinyl)cinnamic acid (CAH) ligands. Stable Pickering emulsions were formed at the water–dichloromethane interface by the self-assembly of CQDs with Janus-ligand shells by homogenization. The breakdown of methyl orange (MO) dye

molecules is used as a test for the photocatalytic qualities. When PbS CQDs without Janus-ligand shells were used, no degradation happened, but the CQD Pickering emulsions showed a considerable deterioration of MO under the same circumstances. Furthermore, they proposed that Pickering emulsions could improve the reaction yield of PbS CQD-catalyzed heterogeneous photocatalyzed reactions, hence providing opportunities for a wider spectrum of organic transformations, including C–C coupling and dehalogenation.³³¹ It was suggested by Shenjie Li *et al.* to make use of Ag–In–S (AIS) CQDs as a catalyst to break down the MO solvent itself, as well as to produce them in a methyl orange (MO) solution. They observed that the AIS CQDs that were synthesised had a degrading efficiency of more than 90%.³³² Coacervate nanodroplets (NDs) embedded with CQDs have been created by Shivendra Singh *et al.* as effective photocatalytic nanoreactors for visible-light-driven chemical reactions. In comparison to CQDs alone, these nanoreactors with CdTe CQDs and poly(diallyl dimethyl) ammonium chloride (PDADMAC) showed increased photocatalytic activity in bulk aqueous solution. The NDs demonstrated effective recyclability without appreciably lowering reaction kinetics or conversion yield. The breakdown of the dyes MB and RhB as well as the conversion of Fe^{3+} to Fe^{2+} were among the photocatalytic reactions. The enhanced activity was ascribed to modified CQD surface charge density and elevated reactant concentrations inside the restricted ND structure. Furthermore, they predicted that the observed photocatalytic reactions may have been facilitated by photogenerated electrons and holes from implanted CQDs.³³³ Barium (Ba)-doped CdS CQDs (3 and 6 wt% Ba) were produced by Ata Ur Rehman *et al.* for the degradation of MB dye. In neutral, basic, and acidic solutions, the catalytic activity against MB dye was substantial for both virgin and Ba-doped CQDs, with degradation percentages of 62.59%, 70.15%, and 72.74%, respectively.³³⁴ Somayeh Naseri Pourtakallo mentioned a simple method for the growth of the CdS shell around CdTe QDs and the formation of the CdTe/CdS core–shell structure, which they used for Hg^{2+} sensing and dye degradation. The produced CQDs performed exceptionally well and had greater selectivity when it came to detecting Hg^{2+} in water. Furthermore, they demonstrated

improved photocatalytic capabilities in comparison to bare CdTe CQDs; the CdTe/CdS core–shell CQDs degraded the MO dye by 88.2% when exposed to UV light.³³⁵ The degradation efficiencies of the CQD-based systems, along with the types of dyes and pollutants, are listed in Table 11.

(IV) CO_2 reduction. For photocatalytic CO_2 reduction (CO_2R), a unique strategy was recently used to improve the stability and catalytic activity of CdS CQDs as described in Table 12. Thioglycolate-capped CdS CQDs were used to assemble amphiphilic metallopolymers, specifically rhenium complex-containing polymers [P(Re-IL)], into stable CdS/P(Re-IL) hybrids. Photoinduced electron transfer (PET) from CdS CQDs to the rhenium complex was enhanced by the interfacial contact between CdS and P(Re-IL), which promoted CO_2 reduction to CO under LED 370 nm irradiation. With a CO generation rate of 38.3 mmol g⁻¹ h⁻¹ and a selectivity of 93.8% within under two hours, CdS/P(5% Re-IL) demonstrated the best catalytic performance. Effective electron transfer and improved stability of CdS CQDs were identified as the reasons for the synergistic impact between the P(Re-IL) complex and CdS CQDs.³³⁷ Another experiment involved the photocatalytic conversion of lignin oils and CO_2 into diesel precursors and H₂/syngas using a heterogeneous photocatalytic system free of noble metals and made of electrostatically self-assembled CdSe CQDs/B-SiO₂. The spherical SiO₂ carrier efficiently circulated the CdSe CQDs, improving the availability of active sites. The system demonstrated remarkable efficacy in the green solvent H₂O, with elevated yields for the generation of H₂ (6.0–7.3 mmol g_{cat}⁻¹) and diesel precursors (71–96%). Likewise, high to exceptional yields were achieved when lignin oils and CO_2 were transformed simultaneously into syngas and diesel precursors (diesel precursors: 64–87%, H₂: 5.1–6.7 mmol g_{cat}⁻¹, CO: 5.2–5.6 mmol g_{cat}⁻¹). Well-dispersed CdSe CQDs on SiO₂, which increased active sites, and the synergistic effects of CdSe CQDs engineering with SiO₂ light scattering, which allowed for the recycling of scattered light in the near field of SiO₂, were linked with the improved photocatalytic performance.³³⁸ Constantin D. Sahm *et al.* explored the use of dithiols as surface modifiers for enhancing photocatalytic CO_2 reduction on ZnSe CQDs. They showed that the CQD's surface can be activated and HER can be affected by dithiols, an organic

Table 11 Summary of the performance rate of CQD-based systems' dye and pollutant degradation

Materials	Dye and pollutant names	Degradation efficiency (%)	Ref.
CdS CQDs	MO and RhB	91.4 (MO) 90.0 (RhB)	323
CuS CQDs	Panadol	96.5	324
Ag–In–Zn–S CQDs	AO7	98	325
ZnS CQDs	Oxytetracycline	73	326
Co–ZnS CQDs	Bisphenol A	>80	327
Ag ₂ S CQDs	MB	70.8	328
CdS CQDs	MB, MO, and RhB	94.9 (MO), 94.4 (RB), 81.2 (MB)	329
CdSe CQDs	MO	84	330
PbS CQDs	MO	>80	331
Ag–In–S CQDs	MO	>90	332
CdTe CQDs	MB, and RhB Fe^{3+} to Fe^{2+}	96 (RhB), 84 (MB), ~85 (Fe^{3+} to Fe^{2+})	333
CdS CQDs	MB	62.59 (neutral media), 70.15 (basic media), 72.74 (acidic media)	334
CdTe/CdS CQDs	MO	88.2	335

Table 12 Summary of H₂O₂ generation and CO₂ reduction using advanced CQD systems

Materials	Catalysis type	CO generation rate	H ₂ O ₂ generation rate	Selectivity (%)	Ref.
CdS CQDs	CO ₂ reduction to CO	38.3 mmol g ⁻¹ h ⁻¹	—	93.8	337
CdSe CQDs	CO ₂ reduction to CO	5.2–5.6 mmol g ⁻¹ h ⁻¹	—	93	338
ZnSe CQDs	CO ₂ reduction to CO	4 μmol g ⁻¹ h ⁻¹ (HexDT)	—	—	339
CdSe CQDs	CO ₂ reduction to CO	15 μmol g ⁻¹ h ⁻¹	—	~100	340
CdS CQDs	CO ₂ reduction to CO and H ₂ (syngas)	5500 μmol g ⁻¹ h ⁻¹ (syngas)	—	—	341
InP CQDs	CO ₂ reduction to CO	51 000 TON	—	—	336
Cd-In-S CQDs	CO ₂ reduction to CO	22.9 μmol g ⁻¹ h ⁻¹	—	~80	342
InP/ZnSe/ZnS CQDs	CO ₂ reduction to acetate	0.89 mmol L ⁻¹ h ⁻¹	—	—	343
CuInS ₂ /ZnS CQDs	CO ₂ reduction to CO and H ₂ (syngas)	184.21 μmol with a CO/H ₂ ratio of 0.74	—	—	344
Zn–Cu–In–S–Se CQDs	Formation of H ₂ O ₂	—	2565.5 μmmol g ⁻¹ h ⁻¹	—	345
Cd–Mo–Se CQDs	Formation of H ₂ O ₂	—	1403.5 μmmol g ⁻¹ h ⁻¹	—	346
CuInS ₂ CQDs	Formation of H ₂ O ₂	—	1685.2 μmmol g ⁻¹ h ⁻¹	—	347

molecule class that had not been studied before for CO₂ reduction. Short dithiols inhibited the HER while activating the CQD's surface for CO₂ reduction, such as 1,2-ethanedithiol (EDT). Conversely, in the presence of an immobilised Ni(cyclam) co-catalyst, longer dithiols such as 1,6-hexanedithiol (HexDT) increased the reduction of CO₂.³³⁹ Next, using inorganic (NH₄)₂S ligands and H₂O as a dispersion solvent, Guocan Jiang *et al.* presented a simple and novel approach for creating CQDs aerogels with enhanced photocatalytic performance for CO₂ reduction. Their method prevented the presence of remaining organic ligands on the aerogel surface, which can limit photocatalyst activity, in contrast to conventional procedures that rely on oxidative treatments. They took CdSe CQDs as a model. The resultant CdSe CQD aerogels showed a notable increase in the photocatalytic activity for CO₂ reduction in the absence of sacrificial agents. The CO production rate was 12 times greater than that of pristine-aggregated CQD powders, reaching 15 μmmol g⁻¹ h⁻¹. While the ligand-free surface encouraged close contact between adjacent CQDs and facilitated CO₂ activation on the CQDs' surface, the self-supported porous structure improved light harvesting and CO₂ collection. Also, as co-catalysts immobilised on the gel surface of CQDs, transition-metal cations (Fe²⁺, Co²⁺, and Ni²⁺) helped to separate charges and functioned as catalytic sites for CO₂ reduction.³⁴⁰ Hong-Yan Wang *et al.* immobilised Ni poly-pyridine polymers onto CdS CQDs *via* thiophene immobilisation to form a hybrid photocatalytic assembly. This novel hybrid system produced syngas at a rate above 5500 μmol g_{cat}⁻¹ by enabling effective charge separation. Robust activity in the photo-reduction of CO₂ was facilitated by the molecular-level design of the hybrid photocatalyst, which included Ni poly-pyridine molecular catalysts attached to CdS CQD substrate by thiophene immobilisation. The hybrid proved its capacity to efficiently decrease CO₂ with regulated syngas ratios by exhibiting good selectivity, a favourable interface micro-environment, and effective charge separation.³⁴¹ Bumsoo Chonet *et al.* applied physical immobilisation of InP CQDs onto TiO₂ particles functionalized with a reduction catalyst [(4,4-Y2-by)Re^I(CO)₃Cl, where Y = CH₂PO(OH)₂] to construct a novel hybrid photocatalyst. This innovative InP CQDs-sensitized photocatalyst (InP-CQDs/TiO₂/ReP) functioned as a photosensitizer at lower energy. The process of photoexcited electron transfer was improved by the TiO₂ heterogenization of InP CQDs, leading to a quick electron injection (about 25 ps) *via* oxidative quenching from

photoexcited InP-CQD* to inorganic TiO₂. The very efficient and long-lasting photochemical CO₂ to CO conversion was the outcome of this effective charge separation at the InP-CQD/TiO₂ interface (Fig. 29B). Through ten occurrences of photolysis, the stability of TiO₂-bound InP-CQDs was shown to exist, producing an impressive TON of almost 51 000 over a 420-hour duration.³³⁶ Then there is another study where an effective visible light-responsive photocatalyst for turning CO₂ into CO, Cd-In-S (CIS) colloidal nanocrystals was developed. They found that the electrical structure of CIS and charge carrier separation were significantly influenced by the Cd to In ratio. Various Cd to In ratios were obtained by varying the quantity of Cd precursors using an easy and inexpensive manufacturing method. Under the influence of visible light, the optimised CIS sample (3-CIS) demonstrated a high CO evolution rate of 22.9 μmmol h⁻¹ and selectivity of up to 80% alongside the assistance of Co(bpy)₃²⁺ as a co-catalyst. Moreover, at 400 nm, an apparent quantum yield (AQY) of 1.75% was attained.³⁴² Na Wen *et al.* implanted low-toxic InP/ZnSe/ZnS CQDs into non-photosynthetic bacteria to function as the light-harvesting semiconductor in a photosynthetic biohybrid system for the synthesis of compounds with added value. With perfect biocompatibility, the CQDs effectively penetrated the bacterial core and encouraged the conversion of CO₂ to acetate. Compared to extracellular electrons transported *via* an electron mediator, intracellularly produced electrons were more important in the conversion process. With a quantum efficiency (QE) of 6–8%, the hybrid photosynthetic system that combined CQDs with non-photosynthetic bacteria showed total productivity of photosynthesis products of roughly 0.89 mmol L⁻¹ h⁻¹. The generated acetate was further transformed into a high-value product with the aid of genetically modified *E. coli*. When compared to the *S. ovata*-only group, the *S. ovata*/CQDs hybrid system converted CO₂ to acetate at a significantly higher rate, indicating that intracellular CQDs play a critical function in the photosynthetic biohybrid system.³⁴³ Ying-Yi Ren *et al.* adopted the host-guest interaction technique to create C1@CD-CuInS₂/ZnS CQDs, a self-assembly hybrid photocatalyst that can produce CO and H₂ simultaneously in CO₂-saturated water when exposed to visible light. The hybrid system consisted of cyclodextrin (CD)-modified CuInS₂/ZnS CQDs and a molecular catalyst (C1) connected to [Co(TPA)Cl]_nCl (TPA = tris(2-pyridylmethyl)amine). Through host-guest interaction, the C1@CD-CuInS₂/ZnS CQDs assemblies were created, with CD-CuInS₂/ZnS

CQDs acting as a centre for producing hydrogen and as the molecular catalytic centre for CO₂ reduction. Over 200 hours, the self-assembly system demonstrated strong syngas production activity, yielding 184.21 μmol of syngas with a CO/H₂ ratio of 0.74 (about 2:3). This showed improved syngas generation efficiency over both the pristine Cd-CuInS₂/ZnS CQDs and the non-assembled system.³⁴⁴

(V) H₂O₂ production & N₂ fixation. In a very small number of instances, semiconductor CQDs have also been configured as a photocatalyst for the creation of H₂O₂ and N₂. Deeptimayee Prusty *et al.* used a cation/anion co-alloying approach to form ternary Cu-In-S (CIS) and quaternary ZnCuInS (ZCIS) CQDs, as well as quinary Zn–Cu–In–S–Se (ZCISSe) alloyed CQDs. Given photocatalytic processes, the quinary ZCISSe alloyed CQDs performed better than the other CQDs in terms of light absorption capacity and exciton separation-migration efficiencies. The quinary ZCISSe CQDs showed exceptional photocatalytic activity, especially in the degradation of GMF and the formation of H₂O₂. The H₂O₂ generation rate was 2565.5 μmmol g⁻¹ h⁻¹, with a solar conversion coefficient (SCC) of 0.36%, which is around 2 times higher than CIS and 8 times more than CIS CQDs. Furthermore, after two hours of exposure to visible light, the quinary CQDs showed a GMF degradation rate of 98.8% (k_1 -258 × 10⁻⁴ min⁻¹).³⁴⁵ Jyotirmayee Sahu synthesised Cd–Mo–Se CQDs, utilising thioglycolic acid as a capping ligand to control development for photocatalytic H₂O₂ generation and Cr(vi) reduction. The different Cd and Mo molar ratios in the alloyed CQDs addressed issues such as photoinduced exciton recombination, migration, and surface degradation by enhancing charge movement, improving light harvesting, and reducing charge recombination. Under visible light, the Cd-rich ternary CMSe-1 CQDs outperformed other ternary and Se-based CQD photocatalysts with an amazing photocatalytic H₂O₂ production of 1403.5 μmmol g⁻¹ h⁻¹ (solar-to-chemical conversion efficiency, 0.27%). Furthermore, CMSe-1 demonstrated Cr(vi) photoreduction as high as 93.6% in 2 hours. CMSe-1's enhanced catalytic activity was ascribed to efficient charge carrier separation and transfer.³⁴⁶ Nevertheless, nonstoichiometric Zn–Cu–In–S (ZCIS) quaternary alloyed CQDs were synthesized by Deeptimayee Prusty *et al.*, aiming for efficient photocatalytic H₂O₂ production and ciprofloxacin (CIP) degradation under visible light irradiation. ZCIS-2, the optimised catalyst, produced a noteworthy amount of H₂O₂ at 1685.2 μmmol g⁻¹ h⁻¹, attaining a 0.19% solar-to-chemical conversion efficiency (SCC), which is 5.3 times greater than CuInS₂ (CIS). Plus, ZCIS-2 demonstrated a better 2-hour CIP degradation effectiveness at 96%. Optimised exciton separation/transfer, wide photon absorption, adjustable band alignment, and efficient adsorption/activation were credited with the increased activity. Both single-electron two-step superoxide radical routes and direct two-electron single-step reduction were implicated in the oxygen reduction in the ZCIS system. Scavenger tests, on the other hand, verified that CIP degradation occurred through both direct O₂^{•-} and indirect •OH radical routes.³⁴⁷ Table 12 presents some examples of H₂O₂ production and CO₂ reduction based on CQD systems.

3. Conclusion

In summary, this review looked in depth at the distinctive features of colloidal semiconductor quantum dots (CQDs) that set them apart from other fluorescent compounds and nanomaterials. We thoroughly investigated their unique optoelectronic properties including size and composition-tunable bandgaps, narrow linewidth emissions, tunable surface chemistry and charge transport, excitation-dependent photoluminescence quantum yields, fluorescence blinking, and “dark fractions”. Moreover, we also provided types of blinking observed in CQDs and different models to explain the occurrence of blinking. Furthermore, we extensively covered the diverse applications of CQDs across different domains, including optoelectronic devices (LEDs, solar cells, and photodetectors), analytical sensing (drugs, hazardous chemicals and pesticides, heavy metal ions, etc.), biomedical applications (bio-imaging, biosensing, photothermal therapy, and drug delivery), and photocatalysis (photo redox organic transformations, H₂ and H₂O₂ production, CO₂ reduction, dye degradation, organic/inorganic pollutant degradation, and N₂ fixation). Overall, our analysis provides an in-depth review of current advances in CQDs for a variety of applications, as well as their fundamental properties. Given their exceptional optical and electronic properties with really high PLQY, we predicted that CQDs would be very effective semiconductor-based nanomaterials with a wide range of multidisciplinary applications. Intensive work utilizing these inexpensive nanomaterials is still required to bring these applications out of the lab and into markets and day-to-day life, since several important steps still need to be resolved, including large-scale production, reproducibility, material safety and long-term stability.

Conflicts of interest

The authors declare no competing financial interests.

References

- M. Makkar and R. Viswanatha, Frontier Challenges in Doping Quantum Dots: Synthesis and Characterization, *RSC Adv.*, 2018, **8**(39), 22103–22112.
- K. Agarwal, H. Rai and S. Mondal, Quantum Dots: An Overview of Synthesis, Properties, and Applications, *Mater. Res. Express*, 2023, **10**(6), 062001.
- J. Kim, J. Roh, M. Park and C. Lee, Recent Advances and Challenges of Colloidal Quantum Dot Light-Emitting Diodes for Display Applications, *Adv. Mater.*, 2024, **36**, 2212220.
- S. M. Reimann and M. Manninen, Electronic Structure of Quantum Dots, *Rev. Mod. Phys.*, 2002, **74**(4), 1283–1342.
- A. P. Alivisatos, A. L. Harris, N. J. Levinos, M. L. Steigerwald and L. E. Brus, Electronic States of Semiconductor Clusters: Homogeneous and Inhomogeneous Broadening of the Optical Spectrum, *J. Chem. Phys.*, 1988, **89**(7), 4001–4011.
- V. I. Klimov, Multicarrier Interactions in Semiconductor Nanocrystals in Relation to the Phenomena of Auger Recombination and Carrier Multiplication, *Annu. Rev. Condens. Matter Phys.*, 2014, **5**(1), 285–316.

- 7 F. P. García de Arquer, D. V. Talapin, V. I. Klimov, Y. Arakawa, M. Bayer and E. H. Sargent, Semiconductor Quantum Dots: Technological Progress and Future Challenges, *Science*, 2021, **373**, 6555.
- 8 C. S. M. Martins, A. P. LaGrow and J. A. V. Prior, Quantum Dots for Cancer-Related miRNA Monitoring, *ACS Sens.*, 2022, **7**(5), 1269–1299.
- 9 Z. Liang, M. B. Khawar, J. Liang and H. Sun, Bio-Conjugated Quantum Dots for Cancer Research: Detection and Imaging, *Front. Oncol.*, 2021, **11**, 749970.
- 10 J. Brunetti, G. Riolo, M. Gentile, A. Bernini, E. Paccagnini, C. Falciani, L. Lozzi, S. Scali, L. Depau, A. Pini, P. Lupetti and L. Bracci, Near-Infrared Quantum Dots Labelled with a Tumor Selective Tetrabranched Peptide for in Vivo Imaging, *J. Nanobiotechnol.*, 2018, **16**(1), 1–10.
- 11 Z. Ranjbar-Navazi, M. Eskandani, M. Johari-Ahar, A. Nemati, H. Akbari, S. Davaran and Y. Omidi, Doxorubicin-Conjugated D-Glucosamine- and Folate-Bi-Functionalised InP/ZnS Quantum Dots for Cancer Cells Imaging and Therapy, *J. Drug Target*, 2017, **26**(3), 267–277.
- 12 O. A. Aladesuyi and O. S. Synthesis Oluwafemi, Strategies and Application of Ternary Quantum Dots – in Cancer Therapy, *Nano-Struct. Nano-Objects.*, 2020, **24**, 100568.
- 13 D. Wang, Y. Zhu, X. Wan, X. Zhang and J. Zhang, Colloidal Semiconductor Nanocrystals for Biological Photodynamic Therapy Applications: Recent Progress and Perspectives, *Prog. Nat. Sci.-Mater.*, 2020, **30**(4), 443–455.
- 14 S. Jung and X. Chen, Quantum Dot-Dye Conjugates for Biosensing, Imaging, and Therapy, *Adv. Healthcare Mater.*, 2018, **7**(14), 1800252.
- 15 T. Kim, D. Shin, M. Kim, H. Kim, E. Cho, M. Choi, J. Kim, E. Jang and S. Jeong, Development of Group III-V Colloidal Quantum Dots for Optoelectronic Applications, *ACS Energy Lett.*, 2022, **8**(1), 447–456.
- 16 A. A. Chistyakov, M. A. Zvaigzne, V. R. Nikitenko, A. R. Tameev, I. L. Martynov and O. V. Prezhdo, Optoelectronic Properties of Semiconductor Quantum Dot Solids for Photovoltaic Applications, *J. Phys. Chem. Lett.*, 2017, **8**(17), 4129–4139.
- 17 J. Tang and E. H. Sargent, Infrared Colloidal Quantum Dots for Photovoltaics: Fundamentals and Recent Progress, *Adv. Mater.*, 2010, **23**(1), 12–29.
- 18 A. G. Shulga, S. Kahmann, D. N. Dirin, A. Graf, J. Zaumseil, M. V. Kovalenko and M. A. Loi, Electroluminescence Generation in PbS Quantum Dot Light-Emitting Field-Effect Transistors with Solid-State Gating, *ACS Nano*, 2018, **12**(12), 12805–12813.
- 19 I. J. Kramer and E. H. Sargent, The Architecture of Colloidal Quantum Dot Solar Cells: Materials to Devices, *Chem. Rev.*, 2013, **114**(1), 863–882.
- 20 M. Hoang and H. Chen, Cubic- and Hexagonal-Phase MgZnO Nanoparticles for Electron Transport Layers in Electroluminescent Quantum-Dot Light-Emitting Diodes, *ACS Appl. Nano Mater.*, 2023, **6**(16), 15294–15301.
- 21 C. Li, W. Chen, D. Wu, D. Quan, Z. Zhou, J. Hao, J. Qin, Y. Li, Z. He and K. Wang, Large Stokes Shift and High Efficiency Luminescent Solar Concentrator Incorporated with CuInS₂/ZnS Quantum Dots, *Sci. Rep.*, 2015, **5**(1), 17777.
- 22 H. Kuang, Y. Zhao, W. Ma, L. Xu and L. Wang, Recent Developments in Analytical Applications of Quantum Dots, *Trends, Anal. Chem.*, 2011, **30**(10), 1620–1636.
- 23 N. Gaponik and A. L. Rogach, Thiol-Capped CdTe Nanocrystals: Progress and Perspectives of the Related Research Fields, *Phys. Chem. Chem. Phys.*, 2010, **12**(31), 8685.
- 24 F. M. Raymo and İ. Yıldız, Luminescent Chemosensors Based on Semiconductor Quantum Dots, *Phys. Chem. Chem. Phys.*, 2007, **9**(17), 2036.
- 25 W. R. Algar, A. J. Tavares and U. J. Krull, Beyond Labels: A Review of the Application of Quantum Dots as Integrated Components of Assays, Bioprobes, and Biosensors Utilizing Optical Transduction, *Anal. Chim. Acta*, 2010, **673**(1), 1–25.
- 26 R. Freeman and I. Willner, Optical Molecular Sensing with Semiconductor Quantum Dots (QDs), *Chem. Soc. Rev.*, 2012, **41**(10), 4067.
- 27 E. A. Weiss, Designing the Surfaces of Semiconductor Quantum Dots for Colloidal Photocatalysis, *ACS Energy Lett.*, 2017, **2**(5), 1005–1013.
- 28 K. P. McClelland and E. A. Weiss, Selective Photocatalytic Oxidation of Benzyl Alcohol to Benzaldehyde or C-c Coupled Products by Visible-Light-Absorbing Quantum Dots, *ACS Appl. Energy Mater.*, 2018, **2**(1), 92–96.
- 29 X. Li, C. Tung and L. Wu, Semiconducting Quantum Dots for Artificial Photosynthesis, *Nat. Rev. Chem.*, 2018, **2**(8), 160–173.
- 30 A. I. Ekimov and A. A. Onushchenko, Quantum Size Effect in Three-Dimensional Microscopic Semiconductor Crystals, *JETP Lett.*, 1981, **34**, 345–349.
- 31 R. Rossetti and L. Brus, Electron-Hole Recombination Emission as a Probe of Surface Chemistry in Aqueous Cadmium Sulfide Colloids, *J. Phys. Chem.*, 1982, **86**(23), 4470–4472.
- 32 R. Rossetti, S. Nakahara and L. E. Brus, Quantum Size Effects in the Redox Potentials, Resonance Raman Spectra, and Electronic Spectra of CdS Crystallites in Aqueous Solution, *J. Chem. Phys.*, 1983, **79**(2), 1086–1088.
- 33 A. L. Efros and A. L. Efros, Interband Absorption of Light in A Semiconductor Sphere, *Sov. Phys. Semicond.*, 1982, **16**, 1209–1214.
- 34 W. J. Albery, P. N. Bartlett and J. D. Porter, The electrochemistry of colloidal semiconductor particles, *J. Electrochem. Soc.*, 1984, **131**(12), 2896–2900.
- 35 A. Fojtik, H. Weller and A. Henglein, Photochemistry of Semiconductor Colloids. Size Quantization Effects in Q-Cadmium Arsenide, *Chem. Phys. Lett.*, 1985, **120**(6), 552–554.
- 36 H. Gerischer and M. Luebke, A Particle Size Effect in the Sensitization of TiO₂ Electrodes by a CdS Deposit, *J. Electroanal. Chem.*, 1986, **204**, 225–227.
- 37 C. J. Sandroff, D. M. Hwang and W. M. Chung, Carrier confinement and special crystallite dimensions in layered semiconductor colloids, *Phys. Rev. B: Condens. Matter Mater. Phys.*, 1986, **33**, 5953–5955.

- 38 A. P. Alivisatos, A. L. Harris, N. J. Levinos, M. L. Steigerwald and L. E. Brus, Electronic States of Semiconductor Clusters: Homogeneous and Inhomogeneous Broadening of the Optical Spectrum, *J. Chem. Phys.*, 1988, **89**, 4001–4011.
- 39 C. Murray, D. Norris and M. Bawendi, Synthesis and Characterization of Nearly Monodisperse CdE (E = S, Se, Te) Semiconductor, *J. Am. Chem. Soc.*, 1993, **115**, 8706–8715.
- 40 S. Shyamal and N. Pradhan, Nanostructured Metal Chalcocahide Photocatalysts: Crystal Structures, Synthesis, and Applications, *ACS Energy Lett.*, 2023, **8**(9), 3902–3926.
- 41 H. Hu, B. Dong and W. Zhang, Low-Toxic Metal Halide Perovskites: Opportunities and Future Challenges, *J. Mater. Chem. A*, 2017, **5**(23), 11436.
- 42 P. Reiss, M. Carrière, C. Lincheneau, L. Vaure and S. Tamang, Synthesis of Semiconductor Nanocrystals, Focusing on Nontoxic and Earth-Abundant Materials, *Chem. Rev.*, 2016, **116**, 10731–10819.
- 43 S. Shyamal and N. Pradhan, Nanostructured Metal Chalcocahide Photocatalysts: Crystal Structures, Synthesis, and Applications, *ACS Energy Lett.*, 2023, **8**, 3902–3926.
- 44 W. R. Algar, K. Susumu, J. B. Delehanty and I. L. Medintz, Semiconductor Quantum Dots in Bioanalysis: Crossing the Valley of Death, *Anal. Chem.*, 2011, **83**(23), 8826–8837.
- 45 A. M. Smith and S. Nie, Semiconductor Nanocrystals: Structure, Properties, and Band Gap Engineering, *Acc. Chem. Res.*, 2010, **43**(2), 190–200.
- 46 X. Zhong, M. Han, Z. Dong, T. J. White and W. Knoll, Composition-Tunable $Zn_xCd_{1-x}Se$ Nanocrystals with High Luminescence and Stability, *J. Am. Chem. Soc.*, 2003, **125**(28), 8589–8594.
- 47 X. Jin, K. Xie, T. Zhang, H. Lian, Z. Zhang, B. Xu, D. Li and Q. Li, Cation Exchange Assisted Synthesis of $ZnCdSe/ZnSe$ Quantum Dots with Narrow Emission Line Widths and near-Unity Photoluminescence Quantum Yields, *Chem. Commun.*, 2020, **56**(45), 6130–6133.
- 48 D. A. Hanifi, N. D. Bronstein, B. A. Koscher, Z. Nett, J. K. Swabeck, K. Takano, A. M. Schwartzberg, L. Maserati, K. Vandewal, Y. van de Burgt, A. Salleo and A. P. Alivisatos, Redefining Near-Unity Luminescence in Quantum Dots with Photothermal Threshold Quantum Yield, *Science*, 2019, **363**(6432), 1199–1202.
- 49 F. Meinardi, F. Bruni and S. Brovelli, Luminescent Solar Concentrators for Building-Integrated Photovoltaics, *Nat. Rev. Mater.*, 2017, **2**(12), 1–9.
- 50 Y. Arakawa and H. Sakaki, Multidimensional Quantum Well Laser and Temperature Dependence of Its Threshold Current, *Appl. Phys. Lett.*, 1982, **40**(11), 939–941.
- 51 G. Yang, W. Liu, Y. Bao, X. Chen, C. Ji, B. Wei, F. Yang and X. Wang, Performance Optimization of In(Ga)As Quantum Dot Intermediate Band Solar Cells. *Discover, NANO*, 2023, **18**(1), 67.
- 52 J. Owen, The Coordination Chemistry of Nanocrystal Surfaces, *Science*, 2015, **347**(6222), 615–616.
- 53 I. L. Medintz, H. T. Uyeda, E. R. Goldman and H. Mattoussi, Quantum Dot Bioconjugates for Imaging, Labelling and Sensing, *Nat. Mater.*, 2005, **4**(6), 435–446.
- 54 D. V. Talapin and C. B. Murray, PbSe Nanocrystal Solids for N- and p-Channel Thin Film Field-Effect Transistors, *Science*, 2005, **310**(5745), 86–89.
- 55 J.-S. Lee, M. V. Kovalenko, J. Huang, D. S. Chung and D. V. Talapin, Band-like Transport, High Electron Mobility and High Photoconductivity in All-Inorganic Nanocrystal Arrays, *Nat. Nanotech.*, 2011, **6**(6), 348–352.
- 56 X. Lan, M. Chen, M. H. Hudson, V. Kamysbayev, Y. Wang, P. Guyot-Sionnest and D. V. Talapin, Quantum Dot Solids Showing State-Resolved Band-like Transport, *Nat. Mater.*, 2020, **19**(3), 323–329.
- 57 A. A. Cordones, T. J. Bixby and S. R. Leone, Evidence for Multiple Trapping Mechanisms in Single CdSe/ZnS Quantum Dots from Fluorescence Intermittency Measurements over a Wide Range of Excitation Intensities, *J. Phys. Chem. C*, 2011, **115**(14), 6341–6349.
- 58 A. L. Efros and D. J. Nesbitt, Origin and Control of Blinking in Quantum Dots, *Nat. Nanotech.*, 2016, **11**(8), 661–671.
- 59 M. Nirmal, B. O. Dabbousi, M. G. Bawendi, J. J. Macklin, J. K. Trautman, T. D. Harris and L. E. Brus, Fluorescence Intermittency in Single Cadmium Selenide Nanocrystals, *Nature*, 1996, **383**(6603), 802–804.
- 60 T. S. Bischof, R. E. Correa, D. Rosenberg, E. A. Dauler and M. G. Bawendi, Measurement of Emission Lifetime Dynamics and Biexciton Emission Quantum Yield of Individual InAs Colloidal Nanocrystals, *Nano Lett.*, 2014, **14**(12), 6787–6791.
- 61 V. V. Protasenko, K. L. Hull and M. Kuno, Disorder-induced Optical Heterogeneity in Single CdSe Nanowires, *Adv. Mater.*, 2005, **17**(24), 2942–2949.
- 62 W. Guo, J. Tang, G. Zhang, B. Li, C. Yang, R. Chen, C. Qin, J. Hu, H. Zhong, L. Xiao and S. Jia, Photoluminescence Blinking and Biexciton Auger Recombination in Single Colloidal Quantum Dots with Sharp and Smooth Core/Shell Interfaces, *J. Phys. Chem. Lett.*, 2021, **12**(1), 405–412.
- 63 G. Yuan, D. E. Gómez, N. Kirkwood, K. Boldt and P. Mulvaney, Two Mechanisms Determine Quantum Dot Blinking, *ACS Nano*, 2018, **12**(4), 3397–3405.
- 64 A. L. Efros and M. Rosen, Random Telegraph Signal in the Photoluminescence Intensity of a Single Quantum Dot, *Phys. Rev. Lett.*, 1997, **78**(6), 1110–1113.
- 65 A. A. Cordones and S. R. Leone, Mechanisms for Charge Trapping in Single Semiconductor Nanocrystals Probed by Fluorescence Blinking, *Chem. Soc. Rev.*, 2013, **42**(8), 3209.
- 66 W. Hoheisel, V. L. Colvin, C. S. Johnson and A. P. Alivisatos, Threshold for Quasicontinuum Absorption and Reduced Luminescence Efficiency in CdSe Nanocrystals, *J. Chem. Phys.*, 1994, **101**(10), 8455–8460.
- 67 J. Hoy, P. J. Morrison, L. K. Steinberg, W. E. Buhro and R. A. Loomis, Excitation Energy Dependence of the Photoluminescence Quantum Yields of Core and Core/Shell Quantum Dots, *J. Phys. Chem. Lett.*, 2013, **4**(12), 2053–2060.
- 68 B. Li, P. J. Brosseau, D. P. Strandell, T. G. Mack and P. Kambhampati, Photophysical Action Spectra of Emission from Semiconductor Nanocrystals Reveal Violations

- to the Vavilov Rule Behavior from Hot Carrier Effects, *J. Phys. Chem. C*, 2019, **123**(8), 5092–5098.
- 69 D. Roy, A. Das, C. K. De, S. Mandal, P. R. Bangal and P. K. Mandal, Why Does the Photoluminescence Efficiency Depend on Excitation Energy in Case of a Quantum Dot? A Case Study of CdSe-Based Core/Alloy Shell/Shell Quantum Dots Employing Ultrafast Pump-Probe Spectroscopy and Single Particle Spectroscopy, *J. Phys. Chem. C*, 2019, **123**(11), 6922–6933.
- 70 C. K. De, S. Mandal, D. Roy, S. Ghosh, A. Konar and P. K. Mandal, Ultrafast Dynamics and Ultrasensitive Single-Particle Intermittency in Small-Sized Toxic Metal Free InP-Based Core/Alloy-Shell/Shell Quantum Dots: Excitation Wavelength Dependency toward Variation of PLQY, *J. Phys. Chem. C*, 2019, **123**(46), 28502–28510.
- 71 D. Roy, S. Ghosh, C. K. De, S. Mukherjee, S. Mandal and P. K. Mandal, Excitation-Energy-Dependent Photoluminescence Quantum Yield Is Inherent to Optically Robust Core/Alloy-Shell Quantum Dots in a Vast Energy Landscape, *J. Phys. Chem. Lett.*, 2022, **13**(10), 2404–2417.
- 72 S. Ghosh, S. Mukherjee, S. Mandal, C. K. De, S. Mardanya, A. Saha and P. K. Mandal, Beneficial Intrinsic Hole Trapping and Its Amplitude Variation in a Highly Photoluminescent Toxic-Metal-Free Quantum Dot, *J. Phys. Chem. Lett.*, 2023, **14**(1), 260–266.
- 73 W. M. Sanderson, J. Hoy, C. Morrison, F. Wang, Y. Wang, P. J. Morrison, W. E. Buhro and R. A. Loomis, Excitation Energy Dependence of Photoluminescence Quantum Yields in Semiconductor Nanomaterials with Varying Dimensionalities, *J. Phys. Chem. Lett.*, 2020, **11**(9), 3249–3256.
- 74 D. Tonti, F. van Mourik and M. Chergui, On the Excitation Wavelength Dependence of the Luminescence Yield of Colloidal CdSe Quantum Dots, *Nano Lett.*, 2004, **4**(12), 2483–2487.
- 75 D. Geißler, C. Würth, C. Wolter, H. Weller and U. Resch-Genger, Excitation Wavelength Dependence of the Photoluminescence Quantum Yield and Decay Behavior of CdSe/CdS Quantum Dot/Quantum Rods with Different Aspect Ratios, *Phys. Chem. Chem. Phys.*, 2017, **19**(19), 12509–12516.
- 76 P. Kukura, M. Celebrano, A. Renn and V. Sandoghdar, Imaging a Single Quantum Dot When It Is Dark, *Nano Lett.*, 2009, **9**(3), 926–929.
- 77 Y. Ebenstein, T. Mokari and U. Banin, Fluorescence Quantum Yield of CdSe/ZnS Nanocrystals Investigated by Correlated Atomic-Force and Single-Particle Fluorescence Microscopy, *Appl. Phys. Lett.*, 2002, **80**(21), 4033–4035.
- 78 T. Pons, I. L. Medintz, D. Farrell, X. Wang, A. F. Grimes, D. S. English, L. Berti and H. Mattoussi, Single-molecule Colocalization Studies Shed Light on the Idea of Fully Emitting versus Dark Single Quantum Dots, *Small*, 2011, **7**(14), 2101–2108.
- 79 J. Yao, D. R. Larson, H. D. Vishwasrao, W. R. Zipfel and W. W. Webb, Blinking and Nonradiant Dark Fraction of Water-Soluble Quantum Dots in Aqueous Solution, *Proc. Natl. Acad. Sci. U. S. A.*, 2005, **102**(40), 14284–14289.
- 80 N. Durisic, P. W. Wiseman, P. Grütter and C. D. Heyes, A Common Mechanism Underlies the Dark Fraction Formation and Fluorescence Blinking of Quantum Dots, *ACS Nano*, 2009, **3**(5), 1167–1175.
- 81 N. Durisic, A. G. Godin, D. Walters, P. Grütter, P. W. Wiseman and C. D. Heyes, Probing the “Dark” Fraction of Core-Shell Quantum Dots by Ensemble and Single Particle pH-Dependent Spectroscopy, *ACS Nano*, 2011, **5**(11), 9062–9073.
- 82 B. S. Mashford, M. Stevenson, Z. V. Popović, C. A. Hamilton, Z. Zhou, C. Breen, J. S. Steckel, V. Bulović, M. G. Bawendi, S. Coe-Sullivan and P. T. Kazlas, High-Efficiency Quantum-Dot Light-Emitting Devices with Enhanced Charge Injection, *Nat. Photon.*, 2013, **7**(5), 407–412.
- 83 V. L. Colvin, M. C. Schlamp and A. P. Alivisatos, Light-Emitting Diodes Made from Cadmium Selenide Nanocrystals and a Semiconducting Polymer, *Nature*, 1994, **370**(6488), 354–357.
- 84 G. E. Cragg and A. L. Efros, Suppression of Auger Processes in Confined Structures, *Nano Lett.*, 2009, **10**(1), 313–317.
- 85 A. A. Bakulin, S. Neutzner, H. J. Bakker, L. Ottaviani, D. Barakel and Z. Chen, Charge Trapping Dynamics in PbS Colloidal Quantum Dot Photovoltaic Devices, *ACS Nano*, 2013, **7**(10), 8771–8779.
- 86 J. Hu, Y. Shi, Z. Zhang, R. Zhi, Y. Shen and B. S. Zou, Recent Progress of Infrared Photodetectors Based on Lead Chalcogenide Colloidal Quantum Dots, *Chin. Phys. B*, 2019, **28**(2), 020701.
- 87 H. Zhao, H. Hu, J. Zheng, Y. Qie, K. Yu, Y. Zhu, Z. Luo, L. Lin, K. Yang, T. Guo and F. Li, One-Pot Synthesis of InP Multishell Quantum Dots for Narrow-Bandwidth Light-Emitting Devices, *ACS Appl. Nano Mater.*, 2023, **6**(5), 3797–3802.
- 88 Q. Wu, F. Cao, S. Wang, Y. Wang, Z. Sun, J. Feng, Y. Liu, L. Wang, Q. Cao, Y. Li, B. Wei, W. Wong and X. Yang, Quasi-Shell-Growth Strategy Achieves Stable and Efficient Green InP Quantum Dot Light-Emitting Diodes, *Adv. Sci.*, 2022, **9**(21), 2200959.
- 89 E. Soheyli, A. Biçer, S. S. Ozel, K. Sahin Tiras and E. Mutlugun, Tuning the Shades of Red Emission in InP/ZnSe/ZnS Nanocrystals with Narrow Full Width for Fabrication of Light-Emitting Diodes, *ACS Omega*, 2023, **8**(42), 39690–39698.
- 90 B. Karadza, P. Schiettecatte, H. Van Avermaet, L. Mingabudinova, L. Giordano, D. Respekta, Y.-H. Deng, I. Nakonechnyi, K. De Nolf, W. Walravens, Y. Meuret and Z. Hens, Bridging the Green Gap: Monochromatic InP-Based Quantum-Dot-on-Chip LEDs with over 50% Color Conversion Efficiency, *Nano Lett.*, 2023, **23**(12), 5490–5496.
- 91 J. Feng, M. Jiang, D. Li, Y. Zhang, P. Chen, L. Zhou, Z. Chen, Y. Li, X. Li and X. Xu, Top-Emission ZnSeTe/ZnSe/ZnS-Based Blue Quantum Dot Light-Emitting Diodes with Enhanced Chroma Efficiency, *J. Phys. Chem. Lett.*, 2023, **14**(10), 2526–2532.
- 92 M. De Franco, D. Zhu, A. Asaithambi, M. Prato, E. Charalampous, S. Christodoulou, I. Kriegel, L. De Trizio, L. Manna, H. B. Jalali and F. Di Stasio, Near-Infrared Light-Emitting Diodes Based on ROHS-Compliant InAs/ZnSe Colloidal Quantum Dots, *ACS Energy Lett.*, 2022, **7**(11), 3788–3790.

- 93 S. Zhang, L. Yang, G. Liu, S. Zhang, Q. Shan and H. Zeng, Eco-Friendly Zn–Ag–In–Ga–S Quantum Dots: Amorphous Indium Sulfide Passivated Silver/Sulfur Vacancies Achieving Efficient Red Light-Emitting Diodes, *ACS Appl. Mater. Interfaces*, 2023, **15**(43), 50254–50264.
- 94 L. J. Lim, X. Zhao and Z. Tan, Non-Toxic CuInS₂/ZnS Colloidal Quantum Dots for Near-Infrared Light-Emitting Diodes, *Adv. Mater.*, 2023, **35**(28), 2301887.
- 95 X. Liu, L. Wang, Y. Gao, Y. Zeng, F. Liu, H. Shen, L. Manna and H. Li, Ultrastable and High-Efficiency Deep Red QLEDs through Giant Continuously Graded Colloidal Quantum Dots with Shell Engineering, *Nano Lett.*, 2023, **23**(14), 6689–6697.
- 96 F. Li, J. J. Liu, Q. Xu, R. Chang, L. Wang, Z. Wu, H. Shen and Z. Du, High-Radiance Shortwave Infrared Light-Emitting Diodes Based on Highly Stable PbS Colloidal Quantum Dots, *J. Phys. Chem. Lett.*, 2023, **14**(18), 4252–4258.
- 97 Z. Fu, L. Zhou, Y. Yin, K. Weng, F. Li, S. Lu, D. Liü, W. Liu, L. Wu, Y. Yang, H. Li, L. Duan, H. Xiao, H. Zhang and S. Li, Direct Photo-Patterning of Efficient and Stable Quantum Dot Light-Emitting Diodes via Light-Triggered, Carbocation-Enabled Ligand Stripping, *Nano Lett.*, 2023, **23**(5), 2000–2008.
- 98 R. Singh, S. Akhil, M. Palabathuni, S. Biswas and N. Mishra, Near-Unity Photoluminescence Quantum Yield of Green-Emitting Graded-Alloy Core/Shell Giant Quantum Dots by Z-Type Ligand Passivation for Display Applications, *ACS Appl. Nano Mater.*, 2022, **5**(12), 18014–18022.
- 99 H. Li, W. Zhang, Y. Bian, T. K. Ahn, H. Shen and B. Ji, ZNF2-Assisted Synthesis of Highly Luminescent InP/ZnSe/ZnS Quantum Dots for Efficient and Stable Electroluminescence, *Nano Lett.*, 2022, **22**(10), 4067–4073.
- 100 Z. Zheng, Z. Ren, W. Xia, C. Luo, J. Li, W. Ma, H. Ji, H. Shi and Y. Chen, Bromide Decorated Eco-Friendly ZnSeTe/ZnSe/ZnS Quantum Dots for Efficient Blue Light-Emitting Diodes, *Adv. Mater. Interfaces*, 2022, **10**(5), 2202241.
- 101 Y. Wang, X. Shan, Y. Tang, T. Li, B. Li, P. Jin, K. Liang, D. Li, Y. M. Yang, H. Shen, B. Zhu and B. Ji, Direct Optical Patterning of Nanocrystal-Based Thin-Film Transistors and Light-Emitting Diodes through Native Ligand Cleavage, *ACS Appl. Nano Mater.*, 2022, **5**(6), 8457–8466.
- 102 L. Li, Y. Luo, Q. Wu, L. Wang, G. Jia, T. Chen, C. Zhang and X. Yang, Efficient and Bright Green InP Quantum Dot Light-Emitting Diodes Enabled by a Self-Assembled Dipole Interface Monolayer, *Nanoscale*, 2023, **15**(6), 2837–2842.
- 103 J. Lin, F. Hsu, Y. Chao, G. Lu, M. Mustaqueem and Y. Chen, Self-Assembled Monolayer for Low-Power-Consumption, Long-Term-Stability, and High-Efficiency Quantum Dot Light-Emitting Diodes, *ACS Appl. Mater. Interfaces*, 2023, **15**(21), 25744–25751.
- 104 Y.-K. Wang, H. Wan, J. Xu, Y. Zhong, E. D. Jung, S. Park, S. Teale, M. Imran, Y. Yu, P. Xia, Y. H. Won, K. Kim, Z. Lu, L. Liao, S. Hoogland and E. H. Sargent, Bifunctional Electron-Transporting Agent for Red Colloidal Quantum Dot Light-Emitting Diodes, *J. Am. Chem. Soc.*, 2023, **145**(11), 6428–6433.
- 105 M. Hoang, J. Lü, H. H. Hsieh and H. Chen, The Influence of Spinodal Decomposition-Based Phase Separation in a Hybrid Polymer Hole Transport Layer on Electroluminescent Quantum Dot Light-Emitting Diodes, *J. Mater. Chem. C*, 2023, **11**(33), 11128–11136.
- 106 C. Yuan, F. Tian and S. Chen, ZnSeTe Blue Top-Emitting QLEDs with Color Saturation near Rec.2020 Standards and Efficiency over 18.16%, *Nano Research*, 2022, **16**(4), 5517–5524.
- 107 Q. Li, S. Cao, Y. Bi, Y. Peng, K. J. Xing, Y. Song, Z. Du, B. S. Zou and J. Zhao, Enhancing Performance of Blue ZnTeSe-Based Quantum Dot Light-Emitting Diodes through Dual Dipole Layers Engineering, *Appl. Phys. Lett.*, 2023, **123**(6), DOI: [10.1063/5.0155001](https://doi.org/10.1063/5.0155001).
- 108 M.-M. Gong, F. Li, L. Wang, Q. Xu, Z. Wu, H. Shen, L. S. Li and Z. Du, Highly Monodisperse PbS Quantum Dots with Facet Engineering for High-Radiance Light-Emitting Diodes in the NIR-II Window, *ACS Photonics*, 2022, **10**(7), 2241–2248.
- 109 J. Y. Lee, E. A. Kim, Y. Choi, J. Han, D. Hahm, D. Shin, W. K. Bae, J. Lim and S. Cho, High-Resolution Multicolor Patterning of InP Quantum Dot Films by Atomic Layer Deposition of ZnO, *ACS Photonics*, 2023, **10**(8), 2598–2607.
- 110 R. Özdemir, H. Van Avermaet, O. Erdem, P. Schiettecatte, Z. Hens and T. Aubert, Quantum Dot Patterning and Encapsulation by Maskless Lithography for Display Technologies, *ACS Appl. Mater. Interfaces*, 2023, **15**(7), 9629–9637.
- 111 Z. Ma, Z. Sun, H. Yang, Z. Wang, F. Ren, N. Yin, Q. Chen, Y. Zhang, C. Li, L. Chen and Q. Wang, Interface-Mediation-Enabled High-Performance Near-Infrared AgAuSe Quantum Dot Light-Emitting Diodes, *J. Am. Chem. Soc.*, 2023, **145**(45), 24972–24980.
- 112 S. Pradhan, M. Dalmases, N. Taghipour, B. Kundu and G. Konstantatos, Colloidal Quantum Dot Light Emitting Diodes at Telecom Wavelength with 18% Quantum Efficiency and Over 1 MHz Bandwidth, *Adv. Sci.*, 2022, **9**(20), 2200637.
- 113 A. Onal, G. O. Eren, S. Sadeghi, R. Melikov, M. Han, O. Karatum, M. S. Ozer, H. Bahmani Jalali, I. B. Dogru-Yuksel, I. Yilgor, Ö. Metin and S. Nizamoglu, High-Performance White Light-Emitting Diodes over 150 Lm W⁻¹ Using near-Unity-Emitting Quantum Dots in a Liquid Matrix, *ACS Photonics*, 2022, **9**(4), 1304–1314.
- 114 E. A. Kim, J. Y. Lee, J. Han, H. G. Kang, M. Kim, J. Lim and S.-Y. Cho, Facile Synthesis of Multicolored Stacked Quantum Dot Films for Efficient White Light Emission, *ACS Appl. Nano Mater.*, 2023, **6**(13), 11455–11464.
- 115 Y. Sun, L. Zhang, Y. Lv, Q. Zeng, X. Guo, W. Ji and X. Liu, Highly Stable Core/Shell AgIn₅S₈/ZnS Quantum Dots for Pure White Light-Emitting Diodes, *ACS Appl. Nano Mater.*, 2023, **6**(23), 22311–22319.
- 116 Z. Qin, Y. Chen, T. Chen, M. Liang, P. Wen, C. Guo, C. Ye and Z. Xie, Improved Luminous Efficiency of AgInS₂ Quantum Dots and Zeolitic Imidazolate Framework-70 Composite for White Light Emitting Diode Applications, *Chem. – Eur. J.*, 2023, **29**(45), e202301123.
- 117 N. Li, Y. Gao, Y. Lv, L. Wang, J. Li, Y. He, J. Fan, H. Shen, R. Wu and L. S. Li, Fabrication of Photostable Siloxane-Coated Quantum Dots for White-Light-Emitting Diodes, *ACS Appl. Nano Mater.*, 2023, **6**(13), 11371–11380.

- 118 H. Lu, Z. Hu, H. Liu, Z. Fu, H. Dai, W. Zhang and R. Guo, Single-Phase Cu,Mn-Codoped ZnGaS/ZnS Quantum Dots for Full-Spectrum White-Light-Emitting Diodes, *ACS Appl. Nano Mater.*, 2023, **6**(9), 7375–7383.
- 119 M. Yuan, M. Liu and E. H. Sargent, Colloidal Quantum Dot Solids for Solution-Processed Solar Cells, *Nat. Energy*, 2016, **1**(3), 1–9.
- 120 I. J. Kramer, J. C. Minor, G. Moreno-Bautista, L. Rollny, P. Kanjanaboops, D. Kopilovic, S. M. Thon, G. H. Carey, K. W. Chou, D. Zhitomirsky, A. Amassian and E. H. Sargent, Efficient Spray-coated Colloidal Quantum Dot Solar Cells, *Adv. Mater.*, 2015, **27**(1), 116–121.
- 121 N. C. Greenham, X. Peng and A. P. Alivisatos, Charge Separation and Transport in Conjugated-Polymer/Semiconductor-Nanocrystal Composites Studied by Photoluminescence Quenching and Photoconductivity, *Phys. Rev. B: Condens. Matter Mater. Phys.*, 1996, **54**(24), 17628–17637.
- 122 I. Gur, N. A. Fromer, M. L. Geier and A. P. Alivisatos, Air-Stable All-Inorganic Nanocrystal Solar Cells Processed from Solution, *Science*, 2005, **310**(5747), 462–465.
- 123 L. Rajen Singh and M. A. Hussain, The Temperature Dependent Current-Voltage Characteristics of Chemically Prepared AL/(P)PBS Schottky Barrier Junction, *Chalcogenide Lett.*, 2022, **19**(2), 131–142.
- 124 H. T. Tung, D. Van Thuan, J. H. Kiat and H. P. Dang, Ag⁺ Ion Doped on the CdSe Quantum Dots for Quantum-Dot-Sensitized Solar Cells' Application, *Appl. Phys. A: Mater. Sci. Process.*, 2019, **125**(8), 505.
- 125 V. Venkatachalam, S. Ganapathy, I. Perumal and M. Anandhan, Crystal Shape and Size of CdTe Colloidal Quantum Dots Controlled by Silver Doping for Enhanced Quantum Dots Sensitized Solar Cells Performance, *Colloids Surf., A*, 2023, **656**, 130296.
- 126 A. Alexandrov, M. Zvaigzne, D. Lypenko, I. Nabiev and P. Samokhvalov, Al-, Ga-, Mg-, or Li-Doped Zinc Oxide Nanoparticles as Electron Transport Layers for Quantum Dot Light-Emitting Diodes, *Sci. Rep.*, 2020, **10**(1), 1–11.
- 127 S.-W. Baek, S. Jun, B. Kim, A. H. Proppe, O. Ouellette, O. Voznyy, C. Kim, J. Kim, G. Walters, J. H. Song, S. Jeong, H. R. Byun, M. S. Jeong, S. Hoogland, F. P. García de Arquer, S. O. Kelley, J.-Y. Lee and E. H. Sargent, Efficient Hybrid Colloidal Quantum Dot/Organic Solar Cells Mediated by near-Infrared Sensitizing Small Molecules, *Nat. Energy*, 2019, **4**(11), 969–976.
- 128 F. Tan, S. Qu, Q. Jiang, J. Liu, Z. Wang, F. Li, G. Yue, S. Li, C. Chen, W. Zhang and Z. Wang, Interpenetrated Inorganic Hybrids for Efficiency Enhancement of PbS Quantum Dot Solar Cells, *Adv. Energy Mater.*, 2014, **4**, 17.
- 129 B. B. Jin, X. J. Liu, L. C. Dong, X. X. Zhong, M. Y. Liang, J. Gan, M. Chen and F. Guo, Improving Loading of CdS/CdSe Co-Sensitized Quantum Dots to Enhance the Performance of Solar Cells by Voltage-Assisted SILAR Deposition, *Sol. Energy Mater. Sol. Cells*, 2023, **255**, 112293.
- 130 J. Lee, B. Kim, C. Kim, M.-H. Lee, I. Kozakci, S. Cho, B. Kim, S. Y. Lee, J. Kim, J. Oh and J.-Y. Lee, Unlocking the Potential of Colloidal Quantum Dot/Organic Hybrid Solar Cells: Band Tunable Interfacial Layer Approach, *ACS Appl. Mater. Interfaces*, 2023, **15**(33), 39408–39416.
- 131 S. Kumar, R. Upadhyay and B. Pradhan, Performance Enhancement of Heterojunction ZnO/PbS Quantum Dot Solar Cells by Interface Engineering, *Sol. Energy*, 2020, **211**, 283–290.
- 132 Y. Jung, H. Shin, S.-W. Baek, T. B. Tai, B. Scheffel, O. Ouellette, M. Biondi, S. Hoogland, F. P. García de Arquer and E. H. Sargent, Near-Unity Broadband Quantum Efficiency Enabled by Colloidal Quantum Dot/Mixed-Organic Heterojunction, *ACS Energy Lett.*, 2023, **8**(5), 2331–2337.
- 133 Y. Cao, Y.-J. Dong, H.-Y. Chen, D.-B. Kuang and C.-Y. Su, CdS/CdSe Co-Sensitized Hierarchical TiO₂ Nanofiber/ZnO Nanosheet Heterojunction Photoanode for Quantum Dot-Sensitized Solar Cells, *RSC Adv.*, 2016, **6**(81), 78202–78209.
- 134 J. Ge, W. Li, L. Zhao, Y. Li, X. He, W. Fang, H. Chen and F. Zhang, Constructing Cellular Network TiO₂ Photoanode for Simultaneous Regulation of Charge Transport and Light Harvesting Properties of Quantum Dots Sensitized Solar Cells, *Ceram. Int.*, 2019, **45**(3), 3715–3722.
- 135 Y. Li, W. Li, L. Zhao, J. Ge, X. He, W. Fang and H. Chen, Constructing Micro-Flower Modified Porous TiO₂ Photoanode for Efficient Quantum Dots Sensitized Solar Cells, *J. Photochem. Photobiol., A*, 2019, **375**, 77–84.
- 136 M. Yuan, H. Hu, Y. Wang, H. Xia, X. Zhang, B. Wang, Z. He, M. Yu, Y. Tan, Z. Shi, K. Li, X. Yang, J. Yang, M. Li, X. Chen, L. Hu, X. Peng, J. He, C. Chen, X. Lan and J. Tang, Cation-exchange Enables in Situ Preparation of PbSe Quantum Dot Ink for High Performance Solar Cells, *Small*, 2022, **18**(48), 2205356.
- 137 Y. Liu, H. Wu, G. Shi, Y. Li, Y. Gao, S. Fang, H. Tang, W. Chen, T. Ma, I. Khan, K. Wang, C. Wang, X. Li, Q. Shen, Z. Liu and W. Ma, Merging Passivation in Synthesis Enabling the Lowest Open-circuit Voltage Loss for PbS Quantum Dot Solar Cells, *Adv. Mater.*, 2023, **35**(5), 2207293.
- 138 J. Chen, S. Zheng, D. Jia, W. Liu, A. Andruszkiewicz, C. Qin, M. Yu, J. Liu, E. M. J. Johansson and X. Zhang, Regulating Thiol Ligands of P-Type Colloidal Quantum Dots for Efficient Infrared Solar Cells, *ACS Energy Lett.*, 2021, **6**(5), 1970–1979.
- 139 X. Liu, T. Fu, J. Liu, Y. Wang, Y. Jia, C. Wang, X. Li, X. Zhang and Y. Liu, Solution Annealing Induces Surface Chemical Reconstruction for High-Efficiency PbS Quantum Dot Solar Cells, *ACS Appl. Mater. Interfaces*, 2022, **14**(12), 14274–14283.
- 140 J. Yang, J. T. Oh, M. Kim, H. Song, D. W. Boukhvalov, S. H. Lee, H. Choi and W. Yi, Hybrid Surface Passivation for Retrieving Charge Collection Efficiency of Colloidal Quantum Dot Photovoltaics, *ACS Appl. Mater. Interfaces*, 2020, **12**(39), 43576–43585.
- 141 S. Fang, J. Huang, R. Tao, Q. Wei, X. Ding, S. Yajima, Z. Chen, W. Zhu, C. Liu, Y. Li, N. Yin, L. Song, Y. Liu, G. Shi, H. Wu, Y. Gao, X. Wen, Q. Chen, Q. Shen, Y. Li, Z. Liu, Y. Li and W. Ma, Open-shell Diradical-sensitized

- Electron Transport Layer for High-performance Colloidal Quantum Dot Solar Cells, *Adv. Mater.*, 2023, **35**(21), 2212184.
- 142 Z. Zhang, H. Song, W. Wang, H. Rao, Y. Fang, Z. Pan and X. Zhong, Dual Ligand Capped Quantum Dots Improving Loading Amount for High-Efficiency Quantum Dot-Sensitized Solar Cells, *ACS Energy Lett.*, 2023, **8**(1), 647–656.
- 143 D. V. Talapin, J.-S. Lee, M. V. Kovalenko and E. V. Shevchenko, Prospects of Colloidal Nanocrystals for Electronic and Optoelectronic Applications, *Chem. Rev.*, 2010, **110**(1), 389–458.
- 144 A. De Iacovo, C. Venettacci, L. Colace, L. Scopa and S. Foglia, PbS Colloidal Quantum Dot Photodetectors Operating in the near Infrared, *Sci. Rep.*, 2016, **6**(1), 1–9.
- 145 M. Hopkinson, T. Martin and P. Smowton, III-V Semiconductor Devices Integrated with Silicon, *Semicond. Sci. Technol.*, 2013, **28**(9), 090301.
- 146 L. Colace, G. Assanto, D. Fulgoni and L. Nash, Near-Infrared p-i-n Ge-on-Si Photodiodes for Silicon Integrated Receivers, *J. Lightwave Technol.*, 2008, **26**(16), 2954–2959.
- 147 M. J. R. Heck, J. F. Bauters, M. L. Davenport, J. K. Doylend, S. Jain, G. Kurczveil, S. Srinivasan, Y. Tang and J. E. Bowers, Hybrid Silicon Photonic Integrated Circuit Technology, *IEEE J. Sel. Top. Quantum Electron.*, 2013, **19**(4), 6100117.
- 148 L. Colace and G. Assanto, Germanium on Silicon for Near-Infrared Light Sensing, *IEEE Photonics J.*, 2009, **1**(2), 69–79.
- 149 P. P. Absil, P. Verheyen, P. De Heyn, M. Pantouvaki, G. Lepage, J. De Coster and J. Van Campenhout, Silicon Photonics Integrated Circuits: A Manufacturing Platform for High Density, Low Power Optical I/O's, *Opt. Express*, 2015, **23**(7), 9369.
- 150 V. Sorianello, A. Perna, L. Colace, G. Assanto, H. C. Luan and L. C. Kimerling, Near-Infrared Absorption of Germanium Thin Films on Silicon, *Appl. Phys. Lett.*, 2008, **93**(11), 111115.
- 151 I. Moreels, K. Lambert, D. Smeets, D. De Muynck, T. Nollet, J. C. Martins, F. Vanhaecke, A. Vantomme, C. Delerue, G. Allan and Z. Hens, Size-Dependent Optical Properties of Colloidal PbS Quantum Dots, *ACS Nano*, 2009, **3**(10), 3023–3030.
- 152 M. V. Kovalenko, Opportunities and Challenges for Quantum Dot Photovoltaics, *Nat. Nanotech.*, 2015, **10**(12), 994–997.
- 153 T. Rauch, M. Böberl, S. F. Tedde, J. Fürst, M. V. Kovalenko, G. Hesser, U. Lemmer, W. Heiss and O. Hayden, Near-Infrared Imaging with Quantum-Dot-Sensitized Organic Photodiodes, *Nat. Photonics*, 2009, **3**(6), 332–336.
- 154 R. J. Ellingson, M. C. Beard, J. C. Johnson, P. Yu, O. I. Micic, A. J. Nozik, A. Shabaev and A. L. Efros, Highly Efficient Multiple Exciton Generation in Colloidal PbSe and PbS Quantum Dots, *Nano Lett.*, 2005, **5**(5), 865–871.
- 155 J.-S. Lee, M. V. Kovalenko, J. Huang, D. S. Chung and D. V. Talapin, Band-like Transport, High Electron Mobility and High Photoconductivity in All-Inorganic Nanocrystal Arrays, *Nat. Nanotech.*, 2011, **6**(6), 348–352.
- 156 C. Zhang, X. Yin, G. Chen, Z. Sang, Y. Yang and W. Que, High-Performance Photodetector with a-IGZO/PbS Quantum Dots Heterojunction, *ACS Photonics*, 2023, **10**(3), 790–800.
- 157 C. Zhang, X. Yin, G. Qian, Z. Sang, Y. Yang and W. Que, Gate Voltage Adjusting PbS-I Quantum-dot-sensitized InGaZnO Hybrid Phototransistor with High-sensitivity, *Adv. Funct. Mater.*, 2023, **34**(4), 2308897.
- 158 W. Pan, M. Tan, Y. He, H. Wei and B. Yang, Organic Amine-Bridged Quasi-2D Perovskite/PbS Colloidal Quantum Dots Composites for High-Gain near-Infrared Photodetectors, *Nano Lett.*, 2022, **22**(6), 2277–2284.
- 159 S. Wang, A. Ashokan, S. Balendhran, W. Yan, B. C. Johnson, A. Peruzzo, K. B. Crozier, P. Mulvaney and J. Bullock, Room Temperature Bias-Selectable, Dual-Band Infrared Detectors Based on Lead Sulfide Colloidal Quantum Dots and Black Phosphorus, *ACS Nano*, 2023, **17**(12), 11771–11782.
- 160 T. Dey, S. Singh, S. Jana, S. Das and S. K. Ray, X-Graphene Quantum Dot/PbX (X = S, Se) Hybrid Nanostructures for Self-Powered Two-Color UV-NIR Photodetectors, *ACS Appl. Nano Mater.*, 2023, **6**(22), 20878–20886.
- 161 R. Saran and R. J. Curry, Lead Sulphide Nanocrystal Photodetector Technologies, *Nat. Photonics*, 2016, **10**(2), 81–92.
- 162 J. Zhang, R. W. Crisp, J. Gao, D. M. Kroupa, M. C. Beard and J. M. Luther, Synthetic Conditions for High-Accuracy Size Control of PbS Quantum Dots, *J. Phys. Chem. Lett.*, 2015, **6**(10), 1830–1833.
- 163 I. Moreels, Y. Justo, B. De Geyter, K. Haustraete, J. C. Martins and Z. Hens, Size-Tunable, Bright, and Stable PbS Quantum Dots: A Surface Chemistry Study, *ACS Nano*, 2011, **5**(3), 2004–2012.
- 164 S. A. McDonald, G. Konstantatos, S. Zhang, P. W. Cyr, E. J. D. Klem, L. Levina and E. H. Sargent, Solution-Processed PbS Quantum Dot Infrared Photodetectors and Photovoltaics, *Nat. Mater.*, 2005, **4**(2), 138–142.
- 165 W. Lin, K. Fritz, G. Guerin, G. R. Bardajee, S. Hinds, V. Sukhovatkin, E. H. Sargent, G. D. Scholes and M. A. Winnik, Highly Luminescent Lead Sulfide Nanocrystals in Organic Solvents and Water through Ligand Exchange with Poly(Acrylic Acid), *Langmuir*, 2008, **24**(15), 8215–8219.
- 166 J. Tang, L. Brzozowski, D. A. R. Barkhouse, X. Wang, R. Debnath, R. Wolowiec, E. Palmiano, L. Levina, A. G. Pattantyus-Abraham, D. Jamakosmanovic and E. H. Sargent, Quantum Dot Photovoltaics in the Extreme Quantum Confinement Regime: The Surface-Chemical Origins of Exceptional Air- and Light-Stability, *ACS Nano*, 2010, **4**(2), 869–878.
- 167 H. T. Nguyen, T. T. Tran, V. Bhatt, M. Kumar and J.-H. Yun, Photoluminescence Properties of CdSe/ZnS Quantum Dot Donor-Acceptor via Plasmon Coupling of Metal Nanostructures and Application on Photovoltaic Devices, *J. Phys. Chem. Lett.*, 2022, **13**(19), 4394–4401.
- 168 M. G. Kim, N.-K. Cho, J. H. Ma, M. H. Park, J. H. Park, W. Jeon and S. J. Kang, Controllable Layer-by-Layer CdSe/

- ZnS Quantum-Dot Thin Films for Enhanced Performance of Light-Emitting Diodes and Photodetectors, *ACS Appl. Nano Mater.*, 2023, **6**(15), 14114–14126.
- 169 P. Zhao, T. Qin, G. Mu, S. Zhang, Y. Luo, M. Chen and X. Tang, Band-Engineered Dual-Band Visible and Short-Wave Infrared Photodetector with Metal Chalcogenide Colloidal Quantum Dots, *J. Mater. Chem. C Mater. Opt. Electron. Devices*, 2023, **11**(8), 2842–2850.
- 170 J. Yang, H. Hu, Y. Lv, M. Yuan, B. Wang, Z. He, S. Chen, Y. Wang, Z. Hu, M. Yu, X. Zhang, J. He, J. Zhang, H. Liu, H.-Y. Hsu, J. Tang, H. Song and X. Lan, Ligand-Engineered HgTe Colloidal Quantum Dot Solids for Infrared Photodetectors, *Nano Lett.*, 2022, **22**(8), 3465–3472.
- 171 L. Chen, J. Liu, P. Liu, S. Lu, Y. Yang, X. Liang, L. Zhang, J. Hu, J. Yang, Y. Liu, W. Ma, X. Zhao, X. Lan, J. Zhang, L. Gao and J. Tang, Improved Operation Stability of Colloidal Quantum Dots Photodiodes via Suppressing Ion Migration, *ACS Photonics*, 2023, **10**(7), 2374–2381.
- 172 P. Xia, B. Sun, M. Biondi, J. Xu, O. Atan, M. Imran, Y. Hassan, Y. Liu, J. M. Pina, A. M. Najarian, L. Grater, K. Bertens, L. K. Sagar, H. Anwar, M.-J. Choi, Y. Zhang, M. Hasham, F. P. García de Arquer, S. Hoogland, M. W. B. Wilson and E. H. Sargent, Sequential Co-passivation in InAs Colloidal Quantum Dot Solids Enables Efficient Near-infrared Photodetectors, *Adv. Mater.*, 2023, **35**(28), 2301842.
- 173 T. Guan, W. Chen, H. Tang, D. Li, X. Wang, C. L. Weindl, Y. Wang, Z. Liang, S. Liang, T. Xiao, S. Tu, S. V. Roth, L. Jiang and P. Müller-Buschbaum, Decoding the Self-Assembly Plasmonic Interface Structure in a PbS Colloidal Quantum Dot Solid for a Photodetector, *ACS Nano*, 2023, **17**(22), 23010–23019.
- 174 S. Lu, P. Liu, J. Yang, S. Liu, Y. Yang, L. Chen, J. Liu, Y. Liu, B. Wang, X. Lan, J. Zhang, L. Gao and J. Tang, High-Performance Colloidal Quantum Dot Photodiodes via Suppressing Interface Defects, *ACS Appl. Mater. Interfaces*, 2023, **15**(9), 12061–12069.
- 175 R. Schwanninger, S. M. Koepfli, O. Yarema, A. Dorodnyy, M. Yarema, A. Moser, S. Nashashibi, Y. Fedoryshyn, V. Wood and J. Leuthold, Highly Responsive Mid-Infrared Metamaterial Enhanced Heterostructure Photodetector Formed out of Sintered PbSe/PbS Colloidal Quantum Dots, *ACS Appl. Mater. Interfaces*, 2023, **15**(8), 10847–10857.
- 176 I. Ramiro, O. Özdemir, S. Christodoulou, S. Gupta, M. Dalmases, I. Torre and G. Konstantatos, Mid- and Long-Wave Infrared Optoelectronics via Intraband Transitions in PbS Colloidal Quantum Dots, *Nano Lett.*, 2020, **20**(2), 1003–1008.
- 177 M. Dolatyari, A. Rostami, S. Mathur and A. Klein, Trap Engineering in Solution Processed PbSe Quantum Dots for High-Speed MID-Infrared Photodetectors, *J. Mater. Chem. C Mater. Opt. Electron. Devices*, 2019, **7**(19), 5658–5669.
- 178 M. Chen, X. Lan, X. Tang, Y. Wang, M. H. Hudson, D. V. Talapin and P. Guyot-Sionnest, High Carrier Mobility in HgTe Quantum Dot Solids Improves Mid-IR Photodetectors, *ACS Photonics*, 2019, **6**(9), 2358–2365.
- 179 J. C. Peterson and P. Guyot-Sionnest, Room-Temperature 15% Efficient Mid-Infrared HgTe Colloidal Quantum Dot Photodiodes, *ACS Appl. Mater. Interfaces*, 2023, **15**(15), 19163–19169.
- 180 J. Yang, Y. Lv, Z. He, B. Wang, S. Chen, F. Xiao, H. Hu, M. Yu, H. Liu, X. Lan, H.-Y. Hsu, H. Song and J. Tang, Bi₂S₃Electron Transport Layer Incorporation for High-Performance Heterostructure HgTe Colloidal Quantum Dot Infrared Photodetectors, *ACS Photonics*, 2023, **10**(7), 2226–2233.
- 181 S.-H. Kim, D. Lee, S. Moon, J.-H. Choi, D. Kim, J. Kim and S.-W. Baek, Sulfurized Colloidal Quantum Dot/Tungsten Disulfide Multi-dimensional Heterojunction for an Efficient Self-powered visible-to-SWIR Photodetector, *Adv. Funct. Mater.*, 2023, **33**(43), 2303778.
- 182 S. Li, J. H. Jang, W. Chung, H. Seung, S. I. Park, H. Ma, W. J. Pyo, C. Choi, D. S. Chung, D.-H. Kim, M. K. Choi and J. Yang, Ultrathin Self-Powered Heavy-Metal-Free Cu-in-Se Quantum Dot Photodetectors for Wearable Health Monitoring, *ACS Nano*, 2023, **17**(20), 20013–20023.
- 183 M. Chen, Q. Hao, Y. Luo and X. Tang, Mid-Infrared Intraband Photodetector *via* High Carrier Mobility HgSe Colloidal Quantum Dots, *ACS Nano*, 2022, **16**(7), 11027–11035.
- 184 H. Zhang, J. C. Peterson and P. Guyot-Sionnest, Intraband Transition of HgTe Nanocrystals for Long-Wave Infrared Detection at 12 Mm, *ACS Nano*, 2023, **17**(8), 7530–7538.
- 185 L. Peng, L. Hu and X. Fang, Low-dimensional Nanostructure Ultraviolet Photodetectors, *Adv. Mater.*, 2013, **25**(37), 5321–5328.
- 186 Y. Jin, J. Wang, B. Sun, J. C. Blakesley and N. C. Greenham, Solution-Processed Ultraviolet Photodetectors Based on Colloidal ZnO Nanoparticles, *Nano Lett.*, 2008, **8**(6), 1649–1653.
- 187 S. Liang, H. Sheng, Y. Liu, Z. Huo, Y. Lu and H. Shen, ZnO Schottky Ultraviolet Photodetectors, *J. Cryst. Growth*, 2001, **225**(2–4), 110–113.
- 188 X. Xu, C. Xu and J. Hu, High-Performance Deep Ultraviolet Photodetectors Based on ZnO Quantum Dot Assemblies, *J. Appl. Phys.*, 2014, **116**(10), 103105.
- 189 M.-Y. Li, Z. Li, H. Li, S. Liu, H. Lu, X. Wen and Y. Yang, ZnO Quantum Dot/MXene Nanoflake Hybrids for Ultraviolet Photodetectors, *ACS Appl. Nano Mater.*, 2021, **4**(12), 13674–13682.
- 190 N. Alwadai, S. Mitra, M. N. Hedhili, H. Alamoudi, B. Xin, N. Alaal and I. S. Roqan, Enhanced-Performance Self-Powered Solar-Blind UV-C Photodetector Based on n-ZnO Quantum Dots Functionalized by p-CuO Micro-Pyramids, *ACS Appl. Mater. Interfaces*, 2021, **13**(28), 33335–33344.
- 191 S. Lin, R. Mandavkar, R. Kulkarni, S. Burse, M. A. Habib, S. H. Kim, M.-Y. Li, S. Kunwar and J. Lee, MoS₂ Nanoflake and ZnO Quantum Dot Blended Active Layers on AuPd Nanoparticles for UV Photodetectors, *ACS Appl. Nano Mater.*, 2022, **5**(3), 3289–3302.
- 192 S. Lin, M. A. Habib, S. Burse, R. Mandavkar, T. Khalid, M. H. Joni, M.-Y. Li, S. Kunwar and J. Lee, Hybrid UV

- Photodetector Design Incorporating AuPt Alloy Hybrid Nanoparticles, ZnO Quantum Dots, and Graphene Quantum Dots, *ACS Appl. Mater. Interfaces*, 2023, **15**(1), 2204–2215.
- 193 M. Ganesan and P. Nagaraj, Quantum Dots as Nanosensors for Detection of Toxics: A Literature Review, *Anal. Methods*, 2020, **12**(35), 4254–4275.
- 194 S. Xu, J. Cui and L. Wang, Recent Developments of Low-Toxicity NIR II Quantum Dots for Sensing and Bioimaging, *TrAC, Trends Anal. Chem.*, 2016, **80**, 149–155.
- 195 M. A. Boles, D. Ling, T. Hyeon and D. V. Talapin, The Surface Science of Nanocrystals, *Nat. Mater.*, 2016, **15**(2), 141–153.
- 196 Y. Kim, J. H. Chang, H. Choi, Y.-H. Kim, W. K. Bae and S. Jeong, III–V Colloidal Nanocrystals: Control of Covalent Surfaces, *Chem. Sci.*, 2020, **11**(4), 913–922.
- 197 G. Yuan, D. E. Gómez, N. Kirkwood, K. Boldt and P. Mulvaney, Two Mechanisms Determine Quantum Dot Blinking, *ACS Nano*, 2018, **12**(4), 3397–3405.
- 198 J. Liu, Y. Li, L. Liu, Y. Gao, Y. Zhang, Z. Yin, F. Pi and X. Sun, Current Progress on Antibiotic Sensing Based on Ratiometric Fluorescent Sensors, *Bull. Environ. Contam. Toxicol.*, 2021, **107**(2), 176–184.
- 199 S. Rajendran, V. UshaVipinachandran, K. H. Badagoppam Haroon, I. Ashokan and S. K. Bhunia, A Comprehensive Review on Multi-Colored Emissive Carbon Dots as Fluorescent Probes for the Detection of Pharmaceutical Drugs in Water, *Anal. Methods*, 2022, **14**(43), 4263–4291.
- 200 S. Sargazi, I. Fatima, M. Hassan Kiani, V. Mohammadzadeh, R. Arshad, M. Bilal, A. Rahdar, A. M. Díez-Pascual and R. Behzadmehr, Fluorescent-Based Nanosensors for Selective Detection of a Wide Range of Biological Macromolecules: A Comprehensive Review, *Int. J. Biol. Macromol.*, 2022, **206**, 115–147.
- 201 S. Liu, Z. Zheng and X. Li, Advances in Pesticide Biosensors: Current Status, Challenges, and Future Perspectives, *Anal. Bioanal. Chem.*, 2013, **405**(1), 63–90.
- 202 B. Unnikrishnan, C.-W. Lien, H.-W. Chu and C.-C. Huang, A Review on Metal Nanozyme-Based Sensing of Heavy Metal Ions: Challenges and Future Perspectives, *J. Hazard. Mater.*, 2021, **401**, 123397.
- 203 R. Freeman and I. Willner, Optical Molecular Sensing with Semiconductor Quantum Dots (QDs), *Chem. Soc. Rev.*, 2012, **41**(10), 4067.
- 204 T. Zhang, Z. Gan, S. Zhen, Y. Hu and X. Hu, Ratiometric Fluorescent Probe Based on Carbon Dots and Zn-Doped CdTe QDs for Detection of 6-mercaptopurine, *Opt. Mater.*, 2022, **134**, 113196.
- 205 K. Burton, N. Nic Daeid and O. Adegoke, Surface Plasmon-Enhanced Aptamer-Based Fluorescence Detection of Cocaine Using Hybrid Nanostructure of Cadmium-Free ZnSe/In₂S₃ Core/Shell Quantum Dots and Gold Nanoparticles, *J. Photochem. Photobiol. A*, 2022, **433**, 114131.
- 206 H. Elmizadeh, G. R. Bardajee and A. Moaddeli, Ultrasensitive and Rapid Detection of Methamphetamine in Forensic Biological Fluids Using Fluorescent Aptamer-Nanobiosensors Based on CdTe Quantum Dots, *Microchem. J.*, 2023, **189**, 108519.
- 207 H. Elmizadeh and G. R. Bardajee, Rapid Ultrasensitive Detection of Methamphetamine Based on the FRET Mechanism between Aptamer-Nanobiosensor Based on CdTe/ZnS Quantum Dots and DNA-Conjugated Cy3 Fluorophore: Forensic Biological Fluids, *J. Mol. Liq.*, 2023, **383**, 122093.
- 208 X. Chen, J. Lin, Y. Zhuang, S. Huang, J. Chen and Z. Han, Dual-Mode Turn-on Ratiometric Fluorescence Sensor Based on Carbon Dots and CuInS₂/ZnS Quantum Dots for Detection of Chlorotetracycline, *Spectrochim. Acta, Part A*, 2022, **270**, 120851.
- 209 H. Chen, Z. Cai, J. Gui, Y. Tang, P. Yin, X. Zhu, Y. Zhang, H. Li, M. Liu and S. Yao, A Redox Reaction-Induced Ratiometric Fluorescence Platform for the Specific Detection of Ascorbic Acid Based on Ag₂S Quantum Dots and Multifunctional CoOOH Nanoflakes, *J. Mater. Chem. B*, 2023, **11**(6), 1279–1287.
- 210 J. Wang, L. Wang, X. Su and H. Yu, Core–Shell Quantum Dot-Based Honeycomb Films on Capillary Walls for Rapid in Situ Ascorbic Acid Detection, *ACS Appl. Nano Mater.*, 2023, **6**(13), 12231–12239.
- 211 S. Safari, A. Amiri and A. Badiei, Selective Detection of Aspartic Acid in Human Serum by a Fluorescent Probe Based on CuInS₂@ZnS Quantum Dots, *Spectrochim. Acta, Part A*, 2023, **291**, 122294.
- 212 Y. Shu, J. Gao, J. Chen, J. Yan, J. Sun, D. Jin, Q. Xu and X. Hu, A Near-infrared Fluorescent Sensor Based on the Architecture of Low-toxic Ag₂S Quantum Dot and MnO₂ Nanosheet for Sensing Glutathione in Human Serum Sample, *Talanta*, 2021, **221**, 121475.
- 213 J. Yan, Q. Fu, S. Zhang, Y. Liu, X. Shi, J. Hou, J. Duan and S. Ai, A Sensitive Ratiometric Fluorescent Sensor Based on Carbon Dots and CdTe Quantum Dots for Visual Detection of Biogenic Amines in Food Samples, *Spectrochim. Acta, Part A*, 2022, **282**, 121706.
- 214 S. Chen, S.-N. Yun, Y. Liu, R. Yu, Q. Tu, J. Wang and M.-S. Yuan, A Highly Selective and Sensitive CdS Fluorescent Quantum Dot for the Simultaneous Detection of Multiple Pesticides, *Analyst*, 2022, **147**(14), 3258–3265.
- 215 H. Ehzari, M. Safari, M. Samimi, M. Shamsipur and M. Bagher Gholivand, A Highly Sensitive Electrochemical Biosensor for Chlорpyrifos Pesticide Detection Using the Adsorbent Nanomatrix Contain the Human Serum Albumin and the Pd:CdTe Quantum Dots, *Microchem. J.*, 2022, **179**, 107424.
- 216 K.-Y. Hwa, A. Ganguly, A. Santhan and T. S. K. Sharma, Synthesis of Water-Soluble Cadmium Selenide/Zinc Sulfide Quantum Dots on Functionalized Multiwalled Carbon Nanotubes for Efficient Covalent Synergism in Determining Environmental Hazardous Phenolic Compounds, *ACS Sustainable Chem. Eng.*, 2022, **10**(3), 1298–1315.
- 217 Y. Li, T. Wang, Z. Li, J. Yang, Z. Yan, F. Luo, R. Zhou, T. Luan, L. Shui and X. Xing, Photothermal Waveguide-Directed Microreactor for Enhanced Copper Ion Detection from Quantum Dots, *ACS Appl. Nano Mater.*, 2022, **5**(7), 9179–9187.

- 218 S. P. Aswathy, devi Vaisakh, S. S. MPTS Modified ZnS–Mn²⁺ Quantum Dot Probes for Cu²⁺ Ions Fluorescent Sensing in Aqueous Solution, *J. Anal. Chem.*, 2023, **78**(2), 175–184.
- 219 J. V. Rajendran, S. Parani, R. Pillay, V. Remya, T. C. Lebepe, R. Maluleke, S. Thomas and O. S. Oluwafemi, Selective and Sensitive Detection of Cu²⁺ Ions in the Midst of Other Metal Ions Using Glutathione Capped CuInS₂/ZnS Quantum Dots, *Phys. E*, 2022, **136**, 115026.
- 220 F. K. Algethami, I. Saidi, H. Ben Jannet, M. Khairy, B. Y. Abdulkhair, Y. O. Al-Ghamdi and H. N. Abdelhamid, Chitosan-CdS Quantum Dots Biohybrid for Highly Selective Interaction with Copper(II) Ions, *ACS Omega*, 2022, **7**(24), 21014–21024.
- 221 S. Das and S. Paul, Optimized One-pot Synthesis of CdSe Quantum Dot Capped with 3-mercaptopropionic Acid as an Efficient Fluorescent Probe for Selective Detection of Hg (II), *Water Environ. J.*, 2022, **36**(3), 541–552.
- 222 G. Granados-Oliveros, B. S. G. Pineros and F. G. O. Calderon, CdSe/ZnS Quantum Dots Capped with Oleic Acid and L-Glutathione: Structural Properties and Application in Detection of Hg²⁺, *J. Mol. Struct.*, 2022, **1254**, 132293.
- 223 Y. Elkony, M. Ali, S. Ebrahim and R. Adel, High Photoluminescence Polyindole/CuInS Quantum Dots for Pb Ions Sensor, *J. Inorg. Organomet. Polym. Mater.*, 2022, **32**(8), 3106–3116.
- 224 S. Mabrouk, H. Rinnert, L. Balan, J. Jasniewski, G. Medjahdi, R. Ben Chaabane and R. Schneider, Aqueous Synthesis of Core/Shell/Shell ZnSeS/Cu:ZnS/ZnS Quantum Dots and Their Use as a Probe for the Selective Photoluminescent Detection of Pb²⁺ in Water, *J. Photochem. Photobiol. A*, 2022, **431**, 114050.
- 225 Q.-B. Hoang, T.-N. Nguyen, T.-P. Nguyen, A.-D. Nguyen, N.-H. Chu, V.-T. Ta, V.-H. Nguyen and X.-D. Mai, Size-Dependent Reactivity of Highly Photoluminescent CdZnTeS Alloyed Quantum Dots to Mercury and Lead Ions, *Chem. Phys.*, 2022, **552**, 111378.
- 226 J. Zhou, Y. Zhang, Y. Du, R. Zhao, S. Liu, W. Li, Q. Wang and P. Yang, C-CdTe Quantum Dots as Dual-Wavelength Fluorescence and Colorimetric Probes to Detect Hydrogen Peroxide, Hydroxyl Radicals, and Iron(II) in Serum, *ACS Appl. Nano Mater.*, 2022, **5**(10), 15875–15884.
- 227 Z. Hu, L. Zhou, L. Li, J. Liu, H.-Y. Li, B. Song, J. Zhang, J. Tang and H. Liu, Stabilization of PbS Colloidal-Quantum-Dot Gas Sensors Using Atomic-Ligand Engineering, *Sens. Actuators B*, 2023, **388**, 133850.
- 228 Y. Zhang, W. Pan, G. Dong and D. Zhang, A High-Performance Room Temperature Methanol Gas Sensor Based on Alpha-Iron Oxide/Polyaniline/PbS Quantum Dots Nanofilm, *J. Mater. Sci.: Mater. Electron.*, 2019, **30**(19), 17907–17915.
- 229 G. R. Bardajee, M. Zamani, H. Mahmoodian, H. Elmizadeh, H. Yari, L. Jouyandeh, R. Shirkavand and M. Sharifi, Capability of Novel Fluorescence DNA-Conjugated CdTe/ZnS Quantum Dots Nanoprobe for COVID-19 Sensing, *Spectrochim. Acta, Part A*, 2022, **269**, 120702.
- 230 G. R. Bardajee, R. Shirkavand and M. Zamani, Specific Oligonucleotide-Modified QDs as a Powerful Platform for SARS Cov-2 Virus Detection by FRET-Based Biosensors, *Mater. Sci. Eng. B Solid State Mater. Adv. Technol.*, 2023, **297**, 116756.
- 231 F. Yang, J. Gong, M. Li, X. Jiang, J. Zhang, M. Liao, H. Zhang, P.-L. Tremblay and T. Zhang, Electrochemiluminescent CdS Quantum Dots Biosensor for Cancer Mutation Detection at Different Positions on Linear DNA Analytes, *Anal. Chem.*, 2023, **95**(37), 14016–14024.
- 232 A. S. Khan, T. H. Ibrahim, N. A. Jabbar, M. I. Khamis, P. Nancarrow and F. S. Mjalli, Ionic Liquids and Deep Eutectic Solvents for the Recovery of Phenolic Compounds: Effect of Ionic Liquids Structure and Process Parameters, *RSC Adv.*, 2021, **11**(20), 12398–12422.
- 233 D. Ren, B. Wang, C. Hu and Z. You, Quantum Dot Probes for Cellular Analysis, *Anal. Methods*, 2017, **9**(18), 2621–2632.
- 234 R. Lamba, A. Salam, F. Anjum, A. Yadav, R. Garg, K. Kaushik, S. Sharma and C. K. Nandi, NIR-emissive carbon nanodots as a tool to mark ribosomal RNA and nucleolus components using super-resolution microscopy, *Nanoscale*, 2024, **16**, 11739–11748.
- 235 R. Lamba, Y. Yukta, J. Mondal, R. Kumar, B. Pani and B. Singh, Carbon Dots: Synthesis, Characterizations, and Recent Advancements in Biomedical, Optoelectronics, Sensing, and Catalysis Applications, *ACS Appl. Bio Mater.*, 2024, **7**(4), 2086–2127.
- 236 M. Borovaya, I. Horiunova, S. Plokhovska, N. Pushkarova, Y. Blume and A. Yemets, Synthesis, Properties and Bioimaging Applications of Silver-Based Quantum Dots, *Int. J. Mol. Sci.*, 2021, **22**(22), 12202.
- 237 Y. Zheng, S. Gao and J. Y. Ying, Synthesis and Cell-imaging Applications of Glutathione-capped CdTe Quantum Dots, *Adv. Mater.*, 2007, **19**(3), 376–380.
- 238 K.-T. Yong, H. Ding, I. Roy, W.-C. Law, E. J. Bergey, A. Maitra and P. N. Prasad, Imaging Pancreatic Cancer Using Bioconjugated InP Quantum Dots, *ACS Nano*, 2009, **3**(3), 502–510.
- 239 C. Zhao, Z. Bai, X. Liu, Y. Zhang, B. Zou and H. Zhong, Small GSH-Capped CuInS₂ Quantum Dots: MPA-Assisted Aqueous Phase Transfer and Bioimaging Applications, *ACS Appl. Mater. Interfaces*, 2015, **7**(32), 17623–17629.
- 240 L. Zhou, B. Yu, L. Huang, H. Cao, D. Lin, Y. Jing, F. Wali and J. Qu, Nonblinking Core–Multishell InP/ZnSe/ZnS Quantum Dot Bioconjugates for Super-Resolution Imaging, *ACS Appl. Nano Mater.*, 2022, **5**(12), 18742–18752.
- 241 J. Xu, K. F. Tehrani and P. Kner, Multicolor 3D Super-Resolution Imaging by Quantum Dot Stochastic Optical Reconstruction Microscopy, *ACS Nano*, 2015, **9**(3), 2917–2925.
- 242 J. M. Urban, W. Chiang, J. W. Hammond, N. M. B. Cogan, A. Litzburg, R. Burke, H. A. Stern, H. A. Gelbard, B. L. Nilsson and T. D. Krauss, Quantum Dots for Improved Single-Molecule Localization Microscopy, *J. Phys. Chem. B*, 2021, **125**(10), 2566–2576.
- 243 X. Yang, K. Zhanghao, H. Wang, Y. Liu, F. Wang, X. Zhang, K. Shi, J. Gao, D. Jin and P. Xi, Versatile Application of

- Fluorescent Quantum Dot Labels in Super-Resolution Fluorescence Microscopy, *ACS Photonics*, 2016, **3**(9), 1611–1618.
- 244 T. Wang, G. Li, D. Wang, F. Li, D. Men, T. Hu, Y. Xi and X.-E. Zhang, Quantitative Profiling of Integrin Av β 3 on Single Cells with Quantum Dot Labeling to Reveal the Phenotypic Heterogeneity of Glioblastoma, *Nanoscale*, 2019, **11**(39), 18224–18231.
- 245 K. Kaushik, A. Yadav, F. Anjum, P. Mani Mishra, S. Sharma, C. Rao and C. Kanti Nandi, Protein Conjugation Helped CdTe Quantum Dots for the Specific Labeling and Super-resolution Imaging of Lysosomes, *ChemNanoMat*, 2022, **8**(10), e202200235.
- 246 Z.-Q. Zhang, W.-J. Yao, L.-L. Qiao, X. Yang, J. Shi and M.-X. Zhao, A Lysosome-Targetable Fluorescence Probe Based on L-Cysteine-Polyamine-Morpholine-Modified Quantum Dots for Imaging in Living Cells, *Int. J. Nanomedicine*, 2020, **15**, 1611–1622.
- 247 S. Pandey and D. Bodas, Exploiting the UV Excited Size-Dependent Emission of PDMS-Coated CdTe Quantum Dots for *in Vitro* Simultaneous Multicolor Imaging of HepG2 Cellular Organelles, *Mater. Adv.*, 2023, **4**(7), 1694–1701.
- 248 N. Hildebrandt, C. M. Spillmann, W. R. Algar, T. Pons, M. H. Stewart, E. Oh, K. Susumu, S. A. Diaz, J. B. Delehanty and I. L. Medintz, Energy Transfer with Semiconductor Quantum Dot Bioconjugates: A Versatile Platform for Biosensing, Energy Harvesting, and Other Developing Applications, *Chem. Rev.*, 2017, **117**(2), 536–711.
- 249 I. V. Martynenko, A. P. Litvin, F. Purcell-Milton, A. V. Baranov, A. V. Fedorov and Y. K. Gun'ko, Application of Semiconductor Quantum Dots in Bioimaging and Biosensing, *J. Mater. Chem. B*, 2017, **5**(33), 6701.
- 250 Z. Lou, P. Li and K. Han, Redox-Responsive Fluorescent Probes with Different Design Strategies, *Acc. Chem. Res.*, 2015, **48**(5), 1358–1368.
- 251 Y. Tang, Y. Li, Z. Wang, F. Pei, X. Hu, Y. Ji, X. Li, H. Zhao, W. Hu, X. Lu, Q. Fan and W. Huang, Organic Semiconducting Nanoprobe with Redox-Activatable NIR-II Fluorescence for *in Vivo* Real-Time Monitoring of Drug Toxicity, *Chem. Commun.*, 2019, **55**(1), 27–30.
- 252 J. Zhou, R. Zhao, Y. Du, S. Liu, W. Li, S. Gai, F. He, L. Feng and P. Yang, A Si–CdTe Composite Quantum Dots Probe with Dual-wavelength Emission for Sensitive Monitoring Intracellular H₂O₂, *Adv. Funct. Mater.*, 2022, **32**(20), 2112083.
- 253 C. Li, W. Li, H. Liu, Y. Zhang, G. Chen, Z. Li and Q. Wang, An Activatable NIR-II Nanoprobe for *in Vivo* Early Real-time Diagnosis of Traumatic Brain Injury, *Angew. Chem., Int. Ed.*, 2020, **59**(1), 247–252.
- 254 Y. Liu, K. Jiang, Y. Nie, Y. Guo and Q. Ma, A Visual Electrochemiluminescence Biosensor Based on CuInZnS Quantum Dots for Superoxide Dismutase Detection, *Anal. Bioanal. Chem.*, 2020, **412**(8), 1893–1899.
- 255 A. Benayas, F. Ren, E. Carrasco, V. Marzal, B. del Rosal, B. A. Gonfa, Á. Juarranz, F. Sanz-Rodríguez, D. Jaque, J. García-Solé, D. Ma and F. Vetrone, PbS/CdS/ZnS Quantum Dots: A Multifunctional Platform for *in Vivo* Near-infrared Low-dose Fluorescence Imaging, *Adv. Funct. Mater.*, 2015, **25**(42), 6650–6659.
- 256 N. Irawati, S. W. Harun, H. A. Rahman, S. S. Chong, N. A. Hamizi and H. Ahmad, Temperature Sensing Using CdSe Quantum Dot Doped Poly(Methyl Methacrylate) Microfiber, *Appl. Opt.*, 2017, **56**(16), 4675.
- 257 H. Zhang, Y. Wu, P. Tang, H. Zhu, Z. Gan, H.-Q. Zhang and D. Wu, Accurate and Real-time Detection Method for the Exothermic Behavior of Enzymatic Nano-microregions Using Temperature-sensitive amino-AgInS₂ Quantum Dots, *Small Methods*, 2022, **6**(1), 2100811.
- 258 D. Zhao, J. Yang, R. Jin, X. Hou, C. Li, W. Chen, Y. Zhao, Q. Wang and B. Liu, Seed-Mediated Synthesis of Polypeptide-Engineered Stabilized Fluorescence-Enhanced Core/Shell Ag₂S Quantum Dots and Their Application in pH Sensing and Bacterial Imaging in Extreme Acidity, *ACS Sustainable Chem. Eng.*, 2019, **7**(15), 13098–13104.
- 259 C. Ding, S. Cheng, C. Zhang, Y. Xiong, M. Ye and Y. Xian, Ratiometric Upconversion Luminescence Nanoprobe with Near-Infrared Ag₂S Nanodots as the Energy Acceptor for Sensing and Imaging of pH *in Vivo*, *Anal. Chem.*, 2019, **91**(11), 7181–7188.
- 260 Y. Wu, Q. Wang, T. Wu, W. Liu, H. Nan, S. Xu and Y. Shen, Detection and Imaging of Hydrogen Sulfide in Lysosomes of Living Cells with Activatable Fluorescent Quantum Dots, *ACS Appl. Mater. Interfaces*, 2018, **10**(50), 43472–43481.
- 261 C. Wang, M. Niu, W. Wang, L. Su, H. Feng, H. Lin, X. Ge, R. Wu, Q. Li, J. Liu, H. Yang and J. Song, *In Situ* Activatable Ratiometric NIR-II Fluorescence Nanoprobe for Quantitative Detection of H₂S in Colon Cancer, *Anal. Chem.*, 2021, **93**(27), 9356–9363.
- 262 M. Cai, C. Ding, X. Cao, F. Wang, C. Zhang and Y. Xian, Label-Free Fluorometric Assay for Cytochrome c in Apoptotic Cells Based on near Infrared Ag₂S Quantum Dots, *Anal. Chim. Acta*, 2019, **1056**, 153–160.
- 263 X. An, Y. Zhang, J. Wang, D.-M. Kong, X.-W. He, L. Chen and Y. Zhang, The Preparation of CuInS₂-ZnS-Glutathione Quantum Dots and Their Application on the Sensitive Determination of Cytochrome c and Imaging of HeLa Cells, *ACS Omega*, 2021, **6**(27), 17501–17509.
- 264 M. Cai, C. Ding, F. Wang, M. Ye, C. Zhang and Y. Xian, A Ratiometric Fluorescent Assay for the Detection and Bioimaging of Alkaline Phosphatase Based on near Infrared Ag₂S Quantum Dots and Calcein, *Biosens. Bioelectron.*, 2019, **137**, 148–153.
- 265 D. Yan, Y. He, Y. Ge and G. Song, Fluorescence “Turn on-off” Detection of Heparin and Heparinase I Based on the near-Infrared Emission Polyethyleneimine Capped Ag₂S Quantum Dots, *Sens. Actuators, B*, 2017, **240**, 863–869.
- 266 R. Su, Y.-T. Wu, S. Doulkeridou, X. Qiu, T. J. Sørensen, K. Susumu, I. L. Medintz, P. M. P. van Bergen Henegouwen and N. Hildebrandt, A Nanobody-on-quantum Dot Displacement Assay for Rapid and Sensitive Quantification of the Epidermal Growth Factor Receptor (EGFR), *Angew. Chem. Int. Ed.*, 2022, **61**(33), e202207797.

- 267 Z. Jin, N. Dridi, G. Palui, V. Palomo, J. V. Jokerst, P. E. Dawson, Q.-X. A. Sang and H. Mattoussi, Quantum Dot–Peptide Conjugates as Energy Transfer Probes for Sensing the Proteolytic Activity of Matrix Metalloproteinase-14, *Anal. Chem.*, 2023, **95**(5), 2713–2722.
- 268 Y.-T. Yang, J.-L. Liu, M.-F. Sun, R. Yuan and Y.-Q. Chai, Highly Efficient Electrochemiluminescence of MnS:CdS@ZnS Core–Shell Quantum Dots for Ultrasensitive Detection of MicroRNA, *Anal. Chem.*, 2022, **94**(18), 6874–6881.
- 269 Y. Zhang, Y. Lv, L.-S. Li, X.-J. Zhao, M.-X. Zhao and H. Shen, Aminophosphate Precursors for the Synthesis of Near-unity Emitting InP Quantum Dots and Their Application in Liver Cancer Diagnosis, *Exploration*, 2022, **2**(4), 20220082.
- 270 J. Liu, X. Zhao, H. Xu, Z. Wang and Z. Dai, Amino Acid-Capped Water-Soluble near-Infrared Region CuInS₂/ZnS Quantum Dots for Selective Cadmium Ion Determination and Multicolor Cell Imaging, *Anal. Chem.*, 2019, **91**(14), 8987–8993.
- 271 Y.-J. Li, T.-T. Huang, J. Liu, Y.-Q. Xie, B. Shi, Y.-M. Zhang, H. Yao, T.-B. Wei and Q. Lin, Detection of Lead(II) in Living Cells by Inducing the Transformation of a Supramolecular System into Quantum Dots. *ACS Sustain. Chem. Eng.*, 2022, **10**(24), 7907–7915.
- 272 B. H. Lee, S. Suresh and A. Ekpenyong, Fluorescence Intensity Modulation of CdSe/ZnS Quantum Dots Assesses Reactive Oxygen Species during Chemotherapy and Radiotherapy for Cancer Cells, *J. Biophotonics*, 2019, **12**(2), e201800172.
- 273 L. Wang, X. Kang and D. Pan, Gram-Scale Synthesis of Hydrophilic PEI-Coated AgInS₂ Quantum Dots and Its Application in Hydrogen Peroxide/Glucose Detection and Cell Imaging, *Inorg. Chem.*, 2017, **56**(11), 6122–6130.
- 274 Q. Zhang, S. Zhao, C. Su, Q. Han, Y. Han, X. Tian, Y. Li and C.-Y. Zhang, Construction of a Quantum-Dot-Based FRET Nanosensor through Direct Encoding of Streptavidin-Binding RNA Aptamers for N6-Methyladenosine Demethylase Detection, *Anal. Chem.*, 2023, **95**(35), 13201–13210.
- 275 D. Gholamin, P. Karami, Y. Pahlavan and M. Johari-Ahar, Highly Sensitive Photoelectrochemical Immunosensor for Detecting Cancer Marker CA19-9 Based on a New SnSe Quantum Dot, *Mikrochim. Acta*, 2023, **190**(4), 154.
- 276 J. F. Y. Fong, Y. H. Ng and S. M. Ng, Carbon Dots as a New Class of Light Emitters for Biomedical Diagnostics and Therapeutic Applications, *Fullerenes, Graphenes Nanotubes.*, 2018, 227–295.
- 277 L. Zhao, X. Zhang, X. Wang, X. Guan, W. Zhang and J. Ma, Recent Advances in Selective Photothermal Therapy of Tumor, *J. Nanobiotechnol.*, 2021, **19**(1), 1–15.
- 278 Z. U. Khan, L. U. Khan, H. F. Brito, M. Gidlund, O. L. Malta and P. Di Mascio, Colloidal Quantum Dots as an Emerging Vast Platform and Versatile Sensitizer for Singlet Molecular Oxygen Generation, *ACS Omega*, 2023, **8**(38), 34328–34353.
- 279 M. Dolatyari, F. A. Aghdam, G. Rostami, A. Rostami and I. S. Amiri, Introducing New Conjugated Quantum Dots for Photothermal Therapy in Biological Applications, *Plasmonics*, 2020, **15**(6), 1565–1575.
- 280 G. Gunaydin, M. E. Gedik and S. Ayan, Photodynamic Therapy—Current Limitations and Novel Approaches, *Front. Chem.*, 2021, **9**, 691697.
- 281 M. Hashemkhani, E. Celikbas, M. Khan, A. Sennaroglu and H. Yagci Acar, ALA/Ag₂S/MnO₂ Hybrid Nanoparticles for near-Infrared Image-Guided Long-Wavelength Phototherapy of Breast Cancer, *ACS Biomater. Sci. Eng.*, 2023, **9**(7), 4126–4137.
- 282 M. Hashemkhani, M. Loizidou, A. J. MacRobert and H. Yagci Acar, One-Step Aqueous Synthesis of Anionic and Cationic AgInS₂ Quantum Dots and Their Utility in Improving the Efficacy of ALA-Based Photodynamic Therapy, *Inorg. Chem.*, 2022, **61**(6), 2846–2863.
- 283 M. Hashemkhani, G. Demirci, A. Bayir, A. Muti, A. Sennaroglu, L. Mohammad Hadi, E. Yaghini, M. Loizidou, A. J. MacRobert and H. Yagci Acar, Cetuximab-Ag₂S Quantum Dots for Fluorescence Imaging and Highly Effective Combination of ALA-Based Photodynamic/Chemo-Therapy of Colorectal Cancer Cells, *Nanoscale*, 2021, **13**(35), 14879–14899.
- 284 M. Hashemkhani, K. Bilici, A. Muti, A. Sennaroglu and H. Y. Acar, Ag₂S-Glutathione Quantum Dots for NIR Image Guided Photothermal Therapy, *New J. Chem.*, 2020, **44**(14), 5419–5427.
- 285 E. Celikbas, A. Saymaz, H. Gunduz, I. Koc, E. Cakir, A. Sennaroglu, S. Kolemen, H. Yagci Acar and K. Onbasli, Image-Guided Enhanced PDT/PTT Combination Therapy Using Brominated Hemicyanine-Loaded Folate Receptor-Targeting Ag₂S Quantum Dots, *Bioconjug. Chem.*, 2023, **34**(5), 880–892.
- 286 D. Cui, L. Han, W. Jiang, L. Chen and N. Niu, Ag_{2-3x}Bi_xS Quantum Dots as Single-Component Theranostic Agents for Second near-Infrared Fluorescence Imaging-Guided Photothermal Therapy, *ACS Appl. Nano Mater.*, 2023, **6**(2), 1303–1314.
- 287 T. Yamaguchi, S. Kitahara, K. Kusuda, J. Okamoto, Y. Horise, K. Masamune and Y. Muragaki, Current Landscape of Sonodynamic Therapy for Treating Cancer, *Cancers*, 2021, **13**(24), 6184.
- 288 Y. Zhang, Y. Zhang, Y. Li, Y. Fu, Y. Zhao, W. Zhao, R. Li, Y. Xian, K. Tu, F. Wu, C. Li, Y. Hou and M. Zhang, Harnessing Ag₂S Quantum Dots with Immune Adjuvant for NIR-II Fluorescence Imaging-Guided Sonodynamic Immunotherapy of Colon Cancer, *Chem. Eng. J.*, 2023, **474**, 145685.
- 289 A. Shah, S. Aftab, J. Nisar, M. N. Ashiq and F. J. Iftikhar, Nanocarriers for Targeted Drug Delivery, *J. Drug Delivery Sci. Technol.*, 2021, **62**, 102426.
- 290 Q. Hu, W. Sun, C. Wang and Z. Gu, Recent Advances of Cocktail Chemotherapy by Combination Drug Delivery Systems, *Adv. Drug Delivery Rev.*, 2016, **98**, 19–34.
- 291 M.-X. Zhao and B.-J. Zhu, The Research and Applications of Quantum Dots as Nano-Carriers for Targeted Drug Delivery and Cancer Therapy, *Nanoscale Res. Lett.*, 2016, **11**(1), 1–9.
- 292 A. Banerjee, T. Pons, N. Lequeux and B. Dubertret, Quantum Dots–DNA Bioconjugates: Synthesis to Applications, *Interface Focus*, 2016, **6**(6), 20160064.

- 293 O. S. Wolfbeis, An Overview of Nanoparticles Commonly Used in Fluorescent Bioimaging, *Chem. Soc. Rev.*, 2015, **44**(14), 4743–4768.
- 294 R. Hao, S. Luo, F. Wang, X. Pan, J. Yao, J. Wu, H. Fang and W. Li, Enhancement of Fluorescence and Anti-Tumor Effect of ZnO QDs by La Doping, *Front. Chem.*, 2022, **10**, 1042038.
- 295 F. D. Duman, Y. Akkoc, G. Demirci, N. Bavili, A. Kiraz, D. Gozuacik and H. Y. Acar, Bypassing Pro-Survival and Resistance Mechanisms of Autophagy in EGFR-Positive Lung Cancer Cells by Targeted Delivery of 5FU Using Theranostic Ag₂S Quantum Dots, *J. Mater. Chem. B Mater. Biol. Med.*, 2019, **7**(46), 7363–7376.
- 296 F. D. Duman, M. Erkisa, R. Khodadust, F. Ari, E. Ulukaya and H. Y. Acar, Folic Acid-Conjugated Cationic Ag₂S Quantum Dots for Optical Imaging and Selective Doxorubicin Delivery to HeLa Cells, *Nanomedicine*, 2017, **12**(19), 2319–2333.
- 297 J. V. Rajendran, S. Parani, V. P. R. Remya, T. C. Lebepe, R. Maluleke, O. A. Aladesuyi, S. Thomas and O. S. Oluwafemi, Preparation of β-Cyclodextrin Conjugated, Gelatin Stabilized SBA 15-CuInS₂/ZnS Quantum Dot Nanocomposites for Camptothecin Release, *J. Inorg. Organomet. Polym. Mater.*, 2023, **34**(1), 93–99.
- 298 M. Ruzycka-Ayoush, P. Kowalik, A. Kowalczyk, P. Bujak, A. M. Nowicka, M. Wojewodzka, M. Kruszewski and I. P. Grudzinski, Quantum Dots as Targeted Doxorubicin Drug Delivery Nanosystems in Human Lung Cancer Cells, *Cancer Nanotech.*, 2021, **12**(1), 1–27.
- 299 C. Huang, X.-B. Li, C.-H. Tung and L.-Z. Wu, Photocatalysis with Quantum Dots and Visible Light for Effective Organic Synthesis, *Chem. – Eur. J.*, 2018, **24**(45), 11530–11534.
- 300 X.-B. Li, C.-H. Tung and L.-Z. Wu, Semiconducting Quantum Dots for Artificial Photosynthesis, *Nat. Rev. Chem.*, 2018, **2**(8), 160–173.
- 301 C.-F. Fu, X. Wu and J. Yang, Material Design for Photocatalytic Water Splitting from a Theoretical Perspective, *Adv. Mater.*, 2018, **30**(48), 1802106.
- 302 H.-L. Wu, M.-Y. Qi, Z.-R. Tang and Y.-J. Xu, Semiconductor Quantum Dots: A Versatile Platform for Photoredox Organic Transformation, *J. Mater. Chem. A*, 2023, **11**(7), 3262–3280.
- 303 I. N. Chakraborty, P. Roy and P. P. Pillai, Visible Light-Mediated Quantum Dot Photocatalysis Enables Olefination Reactions at Room Temperature, *ACS Catal.*, 2023, **13**(11), 7331–7338.
- 304 Y.-Y. Yin, X.-R. Liu, J.-H. Jin, Z.-M. Li, Y.-M. Shen, J. Zhou and X. Peng, Visible-Light Induced Three-Component Reaction for α-Aminobutyronitrile Synthesis by C–C Bond Formation Using Quantum Dots as Photocatalysts, *Org. Biomol. Chem.*, 2023, **21**(2), 359–364.
- 305 B. Malile, R. Sodhi and J. I. L. Chen, Mn(II)-Doped CdS/ZnS Core/Shell Quantum Dot Films Photocatalyze Reductive Organic Transformations with a Boost in Efficiency from Enhanced Auger Processes, *J. Mater. Chem. A*, 2022, **10**(47), 25319–25328.
- 306 S. Hooe, J. Breger, S. Dean, K. Susumu, E. Oh, S. Walper, G. A. Ellis and I. L. Medintz, Benzaldehyde Lyase Kinetic Improvements, Potential Channeling to Alcohol Dehydrogenase, and Substrate Scope When Immobilized on Semiconductor Quantum Dots, *ACS Appl. Nano Mater.*, 2022, **5**(8), 10900–10911.
- 307 Y. Jiang, R. López-Arteaga and E. A. Weiss, Quantum Dots Photocatalyze Intermolecular [2+2] Cycloadditions of Aromatic Alkenes Adsorbed to Their Surfaces via van der Waals Interactions, *J. Am. Chem. Soc.*, 2022, **144**(9), 3782–3786.
- 308 Y. Liu, Y. Guo, B. Lin, Z. Chen, X. Ying, M. Zhang, C. Wang, G. Zhang, H. Gu, D. Luo and X. Liu, Gradient Alloyed Quantum Dots for Photocatalytic Lignin Valorization via Proton Coupled Electron Transfer, *ACS Appl. Nano Mater.*, 2023, **6**(8), 6614–6626.
- 309 J. M. Mouat, J. K. Widness, D. G. Enny, M. T. Meidenbauer, F. Awan, T. D. Krauss and D. J. Weix, CdS Quantum Dots for Metallaphotoredox-Enabled Cross-Electrophile Coupling of Aryl Halides with Alkyl Halides, *ACS Catal.*, 2023, **13**(13), 9018–9024.
- 310 J. K. Widness, D. G. Enny, K. S. McFarlane-Connelly, M. T. Miedenbauer, T. D. Krauss and D. J. Weix, CdS Quantum Dots as Potent Photoreductants for Organic Chemistry Enabled by Auger Processes, *J. Am. Chem. Soc.*, 2022, **144**(27), 12229–12246.
- 311 T.-T. Zhao, Y.-Y. Zhang, L.-Q. Wang, Y.-M. Shen and H. Qi, Visible-Light-Mediated Cyclization of Arylamines with Aldehydes Using CdSe/CdS Quantum Dots and Titanium Dioxide Nanotube Composite, *Catal. Lett.*, 2023, **154**(4), 1855–1864.
- 312 C. Nie, X. Lin, G. Zhao and K. Wu, Low-toxicity ZnSe/ZnS Quantum Dots as Potent Photoreductants and Triplet Sensitizers for Organic Transformations, *Angew. Chem., Int. Ed.*, 2022, **134**(49), e202213065.
- 313 S. Benndorf, A. Schleusener, R. Müller, M. Micheel, R. Baruah, J. Dellith, A. Undisz, C. Neumann, A. Turchanin, K. Leopold, W. Weigand and M. Wächtler, Covalent Functionalization of CdSe Quantum Dot Films with Molecular [FeFe] Hydrogenase Mimics for Light-Driven Hydrogen Evolution, *ACS Appl. Mater. Interfaces*, 2023, **15**(15), 18889–18897.
- 314 H. Yu, M. Dou, S. Wang, Y. Cheng, Z. Li, H. Shao, M. Yao, X. Wang, Y. Chen and S. Li, ZIF-8-Supported AgInS₂ Quantum Dots for Photocatalytic H₂ Production by Precise Location Sulfurization, *ACS Appl. Nano Mater.*, 2023, **6**(1), 228–237.
- 315 M. Chen, H. Fang, C. Wang, J. Xu and L. Wang, Enhanced Photocatalytic Cr(vi) Reduction and H₂ Production of CdSe Quantum Dots Supported on Co-Encapsulated N-Doped Carbon, *J. Taiwan Inst. Chem. Eng.*, 2023, **146**, 104798.
- 316 P. Wang, W. Shi, N. Jin, Z. Liu, Y. Wang, T. Cai, K. Hills-Kimball, H. Yang, X. Yang, Y. Jin, X. Wang, J. Zhao and O. Chen, Counterbalancing of Electron and Hole Transfer in Quantum Dots for Enhanced Photocatalytic H₂ Evolution, *Nano Res.*, 2023, **16**(2), 2271–2277.

- 317 A. Jiang, H. Guo, S. Yu, F. Zhang, T. Shuai, Y. Ke, P. Yang and Y. Zhou, Dual Charge-Accepting Engineering Modified AgIn₅S₈/CdS Quantum Dots for Efficient Photocatalytic Hydrogen Evolution Overall H₂S Splitting, *Appl. Catal., B*, 2023, **332**, 122747.
- 318 J. Song, J. Zhang, K. Qi, C. Imparato and S.-Y. Liu, Exploration of the G-C₃N₄ Heterostructure with Ag-in Sulfide Quantum Dots for Enhanced Photocatalytic Activity, *ACS Appl. Electron. Mater.*, 2023, **5**(8), 4134–4144.
- 319 N. Jin, Y. Sun, W. Shi, P. Wang, Y. Nagaoka, T. Cai, R. Wu, L. Dube, H. N. Nyiera, Y. Liu, T. Mani, X. Wang, J. Zhao and O. Chen, Type-I CdS/ZnS Core/Shell Quantum Dot-Gold Heterostructural Nanocrystals for Enhanced Photocatalytic Hydrogen Generation, *J. Am. Chem. Soc.*, 2023, **145**(40), 21886–21896.
- 320 R.-J. Huang, Z.-K. Qin, L.-L. Shen, G. Lv, F. Tao, J. Wang and Y.-J. Gao, Interface Engineering of InP/ZnS Core/Shell Quantum Dots by the Buffer Monolayer for Exceptional Photocatalytic H₂ Evolution, *J. Mater. Chem. A*, 2023, **11**(12), 6217–6225.
- 321 S. Mao, J.-W. Shi, G. Sun, Y. Zhang, D. Ma, K. Song, Y. Lv, J. Zhou, H. Wang and Y. Cheng, PdS Quantum Dots as a Hole Attractor Encapsulated into the MOF@Cd_{0.5}Zn_{0.5}S Heterostructure for Boosting Photocatalytic Hydrogen Evolution under Visible Light, *ACS Appl. Mater. Interfaces*, 2022, **14**(43), 48770–48779.
- 322 H. Guo, P. Yang, J. Hu, A. Jiang, H. Chen, X. Niu and Y. Zhou, Band Structure Engineering and Defect Passivation of Cu_xAg_{1-x}InS₂/ZnS Quantum Dots to Enhance Photoelectrochemical Hydrogen Evolution, *ACS Omega*, 2022, **7**(11), 9642–9651.
- 323 D. Borah, P. Saikia, P. Sarmah, D. Gogoi, A. Das, J. Rout, N. N. Ghosh, P. Pandey and C. R. Bhattacharjee, Photocatalytic and Antibacterial Activity of Fluorescent CdS Quantum Dots Synthesized Using Aqueous Extract of Cyanobacterium Nostoc Carneum, *BioNanoSci.*, 2023, **13**(2), 650–666.
- 324 T. Iqbal, M. Ashraf, S. Afsheen, A. Masood, M. T. Qureshi, S. T. Obediat, M. F. Hamed and M. S. Othman, Copper Sulfide (CuS) Doped with Carbon Quantum Dots (CQD) as an Efficient Photo Catalyst, *Opt. Mater.*, 2022, **125**, 112116.
- 325 M. Mrad, B. Chouchene, T. Ben Chaabane, T. Gries, G. Medjahdi, L. Balan and R. Schneider, Heterostructured Photocatalysts Associating ZnO Nanorods and Ag-in-Zn-S Quantum Dots for the Visible Light-Driven Photocatalytic Degradation of the Acid Orange 7 Dye, *Catalysts*, 2022, **12**(12), 1585.
- 326 Q. Liu, Z. Fan, X. Yi, S. Chen, B. Li and W. Luo, Porous Polyimide/Carbon Quantum Dots/ZnS Quantum Dots Material Aerogel for Efficient Visible-Light Photocatalytic Degradation over Oxytetracycline, *React. Funct. Polym.*, 2022, **178**, 105330.
- 327 Y. Gu, T. Gao, F. Zhang, C. Lu, W. Cao, Z. Fu, C. Hu and L. Lyu, Surface Sulfur Vacancies Enhanced Electron Transfer over Co-ZnS Quantum Dots for Efficient Degradation of Plasticizer Micropollutants by Peroxymonosulfate Activation, *Chin. Chem. Lett.*, 2022, **33**(8), 3829–3834.
- 328 P. Sun, K. Li, K. Lin, W. Wei and J. Zhao, Ag₂S Quantum Dots for Use in Whole-Cell Biohybrid Catalyst for Visible-Light-Driven Photocatalytic Organic Pollutant Degradation, *ACS Appl. Nano Mater.*, 2022, **5**(7), 9754–9760.
- 329 F. Farahmandzadeh, S. Salehi, M. Molaei, H. Fallah and V. Nejadshafiee, CdS Semiconductor Quantum Dots; Facile Synthesis, Application as off Fluorescent Sensor for Detection of Lead (Pb²⁺) Ions and Catalyst for Degradation of Dyes from Water, *J. Fluoresc.*, 2023, **33**(4), 1515–1524.
- 330 Y. Chen, D. Luo, Y. Wei, H. Liu, Y. Huang, L. Fan and J. Wu, Synthesis of 0D/2D CdSe/H₂Nb₃O₁₀ n-n Heterojunction with Excellent Visible-Light-Driven Photocatalytic Performance, *Mater. Sci. Eng., B*, 2023, **290**, 116304.
- 331 Z. Huang, J. T. Koubek, A. Sellinger and M. C. Beard, Pickering Emulsions of Self-Assembled Lead Sulfide Quantum Dots with Janus-Ligand Shells as Nanoreactors for Photocatalytic Reactions, *ACS Appl. Nano Mater.*, 2022, **5**(3), 3183–3187.
- 332 S. Li, X. Gong, Z. Li, M. Yu, Y. Chen, H. Yu, S. Wang, H. Shao, M. Dou and Y. Cheng, Interfacial Nucleation Mechanism of Water-Soluble Ag-in-S Quantum Dots at Room Temperature and Their Visible Light Catalytic Performance, *Langmuir*, 2022, **38**(15), 4692–4701.
- 333 S. Singh, C. Rao, C. K. Nandi and T. K. Mukherjee, Quantum Dot-Embedded Hybrid Photocatalytic Nanoreactors for Visible Light Photocatalysis and Dye Degradation, *ACS Appl. Nano Mater.*, 2022, **5**(5), 7427–7439.
- 334 A. Ur Rehman, M. Ikram, A. Haider, M. A. Raza, T. Shujah, M. Naz, A. Ul-Hamid, I. Shahzadi, S. Goumri-Said, M. B. Kanoun and W. Nabgan, Facile Synthesis of Barium-Doped Cadmium Sulfide Quantum Dots for the Treatment of Polluted Water: Experimental and Computational Investigations, *ACS Omega*, 2022, **7**(50), 46325–46336.
- 335 S. N. Pourtakallo, M. Molaei and M. Khanzadeh, CdTe/CdS Core-Shell Quantum Dots: Synthesis and Applications as a Heavy Metal Ion's Fluorescence Sensor and Photocatalyst for Photodegradation of Organic Dyes, *Phys. Status Solidi A*, 2023, **220**(7), 2200858.
- 336 B. Chon, S. Choi, Y. Seo, H. S. Lee, C. H. Kim, H.-J. Son and S. O. Kang, InP-Quantum Dot Surface-Modified TiO₂ Catalysts for Sustainable Photochemical Carbon Dioxide Reduction, *ACS Sustainable Chem. Eng.*, 2022, **10**(18), 6033–6044.
- 337 W. Boonta, W. Sangkhun, C. Suppaso, N. Chantanop, W. Panchan, K. Chainok, P. Thamyongkit, T. Sudyoedsuk, K. Maeda, T. Butburee and J. Unruangsri, Rhodium(I) Complex-Containing Amphiphilic Metallocopolymer Stabilizing CdS Quantum Dots for Synergistically Boosting Photoreduction of CO₂, *ACS Catal.*, 2023, **13**(18), 12391–12402.
- 338 H. Jiang, Z. Hu, Q. Zhou, Y. Li, C. Gan, M. Sheng, X. Gao and B. Sun, Photocatalytic Lignin Oils and CO₂ Upgradation to Diesel Precursors and Syngas over Engineered CdSe Quantum Dots, *Chem. Eng. J.*, 2023, **471**, 144452.
- 339 C. D. Sahm, A. Ciotti, E. Mates-Torres, V. Badiani, K. Sokołowski, G. Neri, A. J. Cowan, M. García-Melchor

- and E. Reisner, Tuning the Local Chemical Environment of ZnSe Quantum Dots with Dithiols towards Photocatalytic CO₂ Reduction, *Chem. Sci.*, 2022, **13**(20), 5988–5998.
- 340 G. Jiang, J. Wang, N. Li, R. Hübner, M. Georgi, B. Cai, Z. Li, V. Lesnyak, N. Gaponik and A. Eychmüller, Self-Supported Three-Dimensional Quantum Dot Aerogels as a Promising Photocatalyst for CO₂ Reduction, *Chem. Mater.*, 2022, **34**(6), 2687–2695.
- 341 H.-Y. Wang, W.-H. Xie, D.-D. Wei, R. Hu, N. Wang, K. Chang, S.-L. Lei, B. Wang and R. Cao, A Hybrid Assembly with Nickel Poly-pyridine Polymer on CdS Quantum Dots for Photo-reducing CO₂ into Syngas with Controlled H₂/CO Ratios, *ChemSusChem*, 2022, **15**(8), e202200200.
- 342 Q. Wang, X. Ren, R. Chen, L. Jia, C. He, D. Philo, S. Li, L. Shi, S. Luo and J. Ye, Selective Conversion of CO₂ to CO under Visible Light by Modulating Cd to In Ratio: A Case Study of Cd-In-S Colloidal Catalysts, *Appl. Surf. Sci.*, 2023, **610**, 155546.
- 343 N. Wen, Q. Jiang, J. Cui, H. Zhu, B. Ji and D. Liu, Intracellular InP Quantum Dots Facilitate the Conversion of Carbon Dioxide to Value-Added Chemicals in Non-Photosynthetic Bacteria, *Nano Today*, 2022, **47**, 101681.
- 344 Y.-Y. Ren, W. Xia, B.-Y. Deng, J. Liu and F. Wang, Host-Guest Assemblies of Anchoring Molecular Catalysts of CO₂ Reduction onto CuInS₂/ZnS Quantum Dots for Robust Photocatalytic Syngas Production in Water, *Mol. Catal.*, 2022, **520**, 112168.
- 345 D. Prusty, S. Mansingh, N. Priyadarshini and K. M. Parida, Unraveling the Photocatalytic Efficiency of Quinary Alloyed QDs for H₂O₂ Production and Antibiotic Degradation with Detail Kinetic and Influencing Factor Study, *Surf. Interfaces*, 2023, **39**, 102999.
- 346 J. Sahu, S. Mansingh, B. P. Mishra, D. Prusty and K. Parida, Compositionally Engineered Cd-Mo-Se Alloyed QDs toward Photocatalytic H₂O₂ Production and Cr(vi) Reduction with a Detailed Mechanism and Influencing Parameters, *Dalton Trans.*, 2023, **52**(44), 16525–16537.
- 347 D. Prusty, S. Mansingh, N. Priyadarshini and K. M. Parida, Defect Control via Compositional Engineering of Zn-Cu-in-S Alloyed QDs for Photocatalytic H₂O₂ Generation and Micropollutant Degradation: Affecting Parameters, Kinetics, and Insightful Mechanism, *Inorg. Chem.*, 2022, **61**(47), 18934–18949.